The Transport Properties of High-Temperature Superconductor/Graphene Junctions

Sharadh Jois

In partial fulfillment of the Doctor of Philosophy in

Nanoscale Engineering

The College of Nanoscale Science and Engineering
SUNY Polytechnic Institute, Albany, NY

SUNY POLYTECHNIC INSTITUTE

SUNY Polytechnic Institute
College of Nanoscale Science and Engineering

The **dissertation** submitted by Sharadh Jois, under the title,
"The Transport Properties of High-Temperature Superconductor/Graphene Junctions"
has been read by the undersigned. It is hereby recommended for acceptance to the Faculty of the University in partial fulfillment of the requirements for the degree of Doctor of Philosophy.

Dissertation Committee Members

Printed Name	Signature	Date Approved
Prof. Yongqiang Xue	(SUNY Poly Committee Member)	04/19/2023
Prof. Carl Ventrice	(SUNY Poly Committee Member)	4/19/2023
Prof. Vince LaBella	(SUNY Poly Committee Member)	4/19/2023
Prof. Kenneth Burch	(External Committee Member)	April 20 , 2023

As chair of the student's dissertation committee, I confirm that all required edits have been made and the thesis document is accepted in final, approved condition.

Prof. Ji Ung Lee — 4/19/2023
(Dissertation Committee Chair) — Date

Recommendation submitted on behalf of SUNY Polytechnic Institute College of Nanoscale Science and Engineering by:

04/20/2023
Dean of College,
SUNY Polytechnic Institute
Date

Krista Thompson — 4/20/2023
Assistant Dean of Graduate Studies
SUNY Polytechnic Institute
Date

NanoFab East
257 Fuller Road, Albany, NY 12203
PH: 518-437-8686 FX: 518-437-8687
https://sunypoly.edu

Acknowledgments

I found out about CNSE while searching for my B.S. education in nanotechnology. I was drawn to the opportunity at CNSE because of the experience I would gain in nanotechnologies. During my B.S. in Nanoscale Engineering, my curiosity about device physics grew to the extent that pursuing a Ph.D. was the obvious next step. The faculty, staff, and cleanroom facilities at CNSE gave me confidence that my graduate career here can be productive and impactful. I thank CNSE for providing the resources necessary to complete my graduate education.

The work discussed here was possible because of the support and encouragement from many people. I have become a better person and researcher because of them. Words cannot truly capture my gratitude.

The mentorship and support I received from my adviser, Prof. Ji Ung Lee, have been vital to my success. Dr. Lee set high expectations but remained patient and kind as we set out to make and understand the physics of our devices. I will cherish our conversations on Fridays, during the late afternoon, when he would share his passion for quantum mechanics and physics. Some of these conversations then led to new ideas for experiments and projects. I thank him for supporting me through several stages of this thesis project. His lab has been well-equipped to support this work. I thank him for funding the supply of liquid cryogens needed for the experiments. I also appreciate the opportunity to contribute to projects on carbon nanotube devices which exposed me to novel semiconductor physics.

I thank the thesis committee for vetting my work and providing helpful feedback on my results. Prof. Carl Ventrice is one of the kindest people I know. He encouraged me to have a basic understanding of materials and physics. He has been supportive of my academic progress and been available to discuss my career prospects. I thank Prof. Vincent LaBella for asking the high-level questions that have expanded my view of approaching problems and lending us his instruments. Prof. Kenneth Burch from Boston College has brought his expertise on the material properties and junctions made of high-temperature superconductors, specifically BSCCO, to provide useful feedback that has helped improve the quality of this work. I took graduate courses on principles in quantum mechanics with Prof. Alex Xue, which gave me a foundation to begin learning superconductivity and quantum transport. I am appreciative of Prof. Xue's input on my thesis work. Overall, I am very thankful to all my committee members, including Dr. Lee, for guidance, reviewing my results, and helping me become a better researcher.

Our understanding of the experimental results we observed in BSCCO/Gr junctions was greatly enhanced by the contributions of our collaborator, Prof. Jose Lado from Aalto University, Finland. I appreciate his openness to collaborate since the first time I reached out to him. He found time in his busy schedule to run computations, attend our meetings, and review the papers. I thank Dr. Qiang Li and Dr. Genda Gu at Brookhaven National Lab for providing their high-quality BSCCO crystals that were essential to this work.

I am grateful to the members of Dr. Lee's group with whom I had the pleasure of working on experiments and getting our hands dirty to fix tools. I thank Dr. Prathamesh Dhakras and Dr. Sam LaGasse for my initial training in fabrication and measurement. By watching the progression of their work, I understood that conducting graduate research depends on perseverance. Discussions with them helped in solidifying concepts on quantum transport, graphene, and carbon nanotubes. Sam was the one to introduce and champion pick-and-place in the lab. I thank him for sharing his methods with us, which I adopted and developed further for my work. Gideon Oyibo has been a good friend and lab mate. While I did liquid helium measurements, which often meant working for two days non-stop, Gideon would stay up in the lab with me through the night and work on his experiments. We would share jokes and celebrate new results. This helped me forget the arduous nights and put one foot in front of the other, especially when things did not work out. I had the chance to train and mentor an undergraduate student, Thomas Barret. He is a great student and a hard worker. He has helped me on several occasions. He was ready to take on the challenge to flip graphene/h-BN heterostructures to expose pristine graphene on h-BN. Once developed, this could help in the fabrication of BSCCO/Gr devices on h-BN. Finally, I thank the postdocs in Dr. Lee's group. Nargess Arabchigavkani helped us get started with AC+DC measurements. Dr. Sanjib Banik and Dr. Mohammad Javadi helped me during liquid helium measurements.

The Academic Engineering Support Group at CNSE is the spine for the upkeep of labs that students rely on for their research. My work has been possible because of their assistance and oversight in numerous ways. Brian Taylor implemented my design for the motorized pick-and-place for the glovebox. I jokingly say – “Brian can machine parts quicker than a pizza delivery". He and Brian Guynup managed the cryogen orders and delivery schedules. Stephen Stewart has been my first point of contact anytime I have had issues with pumps and vacuum and helped make the glovebox operational. I owe everything I know about operating and maintaining electron microscopes to Miguel Rodriguez from the metrology department. Miguel has been integral in the upkeep of electron microscopes and lithography systems that I have relied on.

My life during grad school has had its fair share of ups and downs, but some people have made it easier by not letting me lose sight of the simple things. I am very grateful for my partner, Emma, who has been extremely supportive of me every single day. We shared our household responsibilities and knew when to take a break. It is common for us to casually engage in long conversations about science, philosophy, and equality over dinner or a walk. She has brought food and coffee for me almost every time I was tied to liquid helium experiments. I cannot imagine living through the COVID-19 era without her. Emma’s diligence, selflessness, and grit have been a continuous source of inspiration for me through the years. I am thankful for my parents supporting me throughout my life and education. Without their support, I would not have had the privilege of pursuing my interests in science. My traits are a combination of my father’s undying passion for innovation and my mother’s project management skills. I thank my sister for always being there to lighten the mood with jokes and for sharing her artwork. I also thank my friends in Albany who are as good as kin – Val and the Stebbins family, Mark & Ana, Emma’s parents, Shashank, and Minhaz; for the dinners and holidays that brought a sense of normalcy to my graduate life.

Abstract

Charge transport in graphene (Gr) has been studied using conventional superconductors (SCs) in different types of devices. Graphene Josephson junctions (Gr-JJ), using *s*-wave superconductors, have shown supercurrents that are gate tunable. Andreev reflection (AR), which occurs at both Gr-SC interfaces in a Gr-JJ is responsible for the supercurrent. A prelude to realizing Gr-JJ using unconventional SCs, such as $Bi_2Sr_2CaCu_2O_{8+x}$ (BSCCO), is to understand transport in a single BSCCO/Gr junction which can reveal unique aspects of AR. We have found that charge transfer from BSCCO into graphene creates a hole-doped region at the boundary of the BSCCO/Gr junction. This doped region renders two different interfaces, one with a superconducting graphene region and the other with a bare graphene region. Together they contribute to two scattering mechanisms – AR and Klein tunneling (KT), respectively, that create resonance states. We use a global gate to simultaneously gate the doped and bare graphene regions and observe an asymmetry in conductance as doping configuration changes from p^+-p to p-n, a hallmark of KT. A resonant interference condition occurs for every two round trips of carriers within the doped region, which produces oscillations in conductance while sweeping the gate voltage. We observe the suppression of the oscillation amplitude above a junction bias ranging between 10 to 15 mV in over half-a-dozen BSCCO/Gr devices. This energy is consistent with the expected size of the induced gap of Δ_i ~15 meV measured by others. Furthermore, we have studied the transport properties in BSCCO-Gr-BSCCO junctions that were fabricated by mechanically cracking a single BSCCO flake, to control the separation length from 20 nm to 3 μm between the SCs, while setting it on graphene. We observe that the oscillation period increases as junction length decreases. In long junctions, the period tends to that of the single

junction. The oscillations suppress for bias between 20 to 30 meV in the BSCCO-Gr-BSCCO junction which corresponds to $2\Delta_i$, as expected for transport between two SCs. These results show the rich transport phenomena in junctions of BSCCO and graphene that may lead to the realization of gate-tunable high-temperature graphene Josephson junctions for quantum computing applications. Superconducting *d*-wave proximity in graphene could create an effective *p*-wave pairing, which is one of the ingredients to create Majorana excitations.

Contents

List of Figures

1. Introduction

Quantum computers break the limitations of classical binary state computing by utilizing superposition and entanglement and rely on the inherent parallelism to exponentially speed up specific calculations. Recent advances in superconducting qubit technology[1,2] have achieved quantum supremacy, i.e., demonstrated their programmable quantum computers can solve a problem that is impossible for a classical computer to solve within a reasonable amount of time. Superconducting transmon qubits are appealing because of their manufacturing scalability using existing semiconductor fabrication facilities. These devices are comprised of Josephson junctions (JJs) made of conventional low-temperature superconductors, such as Al or Nb, that need to operate at millikelvin temperatures and thus require dilution refrigerators. These Josephson junctions have an insulating barrier (oxide or nitride) sandwiched between two superconducting electrodes. Improving the qubit relaxation and coherence times requires greater control over surfaces, interfaces, and contaminants[3]. Van der Waals heterostructures using two-dimensional (2D) materials have shown that atomically pristine surfaces can surprisingly be easily achieved and thus reveal new physics. The variety of 2D (or layered) materials has grown incredibly since the discovery of graphene, a semi-metal, to now include insulators, semiconductors, superconductors, topological insulators, and even topological superconductors[4]. Therefore, we are presented with the opportunity to explore Van der Waals heterostructures with clean interfaces to create JJs that operate at high temperatures.

Graphene nanoelectronics have greatly evolved since the discovery in 2004[5] which showed that pristine monolayers can be mechanically exfoliated. Its electronic properties, governed by the Dirac equation, lead to novel physics such as half-integer quantum Hall effect[6,7], Klein tunneling[8–10], and Veselago lensing[11,12]. Experimental studies of proximity-induced superconductivity in graphene have demonstrated Josephson junctions[13–15], Andreev bound states[16,17] and supercurrents in the quantum Hall states [18]. A special case of inter-band Andreev reflection, also known as specular Andreev reflection[19], was found in superconductor/bilayer graphene junctions[20]. The helical nature[*] of carriers in graphene is at the core of its exotic properties.

Heterojunctions of superconductors with insulators and metals have led to profound discoveries such as the Josephson effect[21,22], new scattering mechanisms (Andreev Reflection, McMillan-Rowell resonances [23,24], Tomasch resonances[25]), and emergent bound states (Andreev bound states[26–28], Yu-Shiba-Rusinov states[29–32]). Similarly, heterojunctions with high-temperature nodal (*d*-wave) superconductors have special scattering mechanisms due to the anisotropic order parameter [33,34].

Supercurrents have been observed in graphene Josephson junctions (GJJ) using a variety of conventional s-wave superconductors[13]. Owing to the nature of s-wave superconductors, these GJJs operate at liquid helium temperatures, and the supercurrent vanishes in a small magnetic field[35]. The supercurrent in the GJJ is gate tunable, exhibits the Fraunhofer pattern, and was found in the quantum Hall regime[36]. Until recently, little was reported about proximity-induced effects in graphene with high-temperature superconductors[37–40], partly due to fabrication challenges[41,42]. However, several theoretical predictions of novel transport phenomena in *d*-wave/graphene junctions[43–46] and of the nature of the induced pseudo-gap[47–49] have urged

[*] projection of pseudo-spin on the direction of motion

experimentalists of the need to find clever solutions to overcome fabrication challenges and investigate these possibilities.

The junctions made of $Bi_2Sr_2CaCu_2O_{8+x}$ (BSCCO) and graphene (Gr) discussed in this work inform the scope of realizing high-temperature GJJs. They shed light on the proximity effects in graphene due to *d*-wave superconductivity and charge transfer from BSCCO. Two scattering mechanisms, Andreev reflection and Klein tunneling, occur together and contribute to the resonance in the single BSCCO/Gr devices. We also bring the superconducting contacts close together to make BSCCO-Gr-BSCCO junctions of different lengths and observe an inverse scaling of resonance period with junction length. This is attributed to losing the interface for Klein tunneling and only having resonances from Andreev reflections. Nodal superconductivity in graphene, like the pseudo-gap induced from a *d*-wave superconductor, is of interest for the discovery of Majorana fermions which are relevant for quantum computing[45,48].

Chapter-2 delves into the background on the electronic properties of graphene. Details on the mechanism of Klein tunneling in graphene are given in section 2.3. We conclude the chapter with a summary of seminal results in graphene transport that arise from Klein tunneling – specifically the conductance asymmetry and Fabry-Perot resonances.

An introduction to the basic properties of superconductors is given in **Chapter-3** to understand the properties of BSCCO.

Chapter-4 covers the properties of cuprate superconductors, with a specific emphasis on BSCCO. We show what makes BSCCO a layered material that we can exfoliate with similar methods used for graphene. A brief literature review is given to substantiate *d*-wave pairing in

BSCCO. The doping-dependent electronic properties are discussed as context for our fabrication strategies and the properties of BSCCO measured in our devices.

Chapter-5 begins with the description of Andreev reflection in superconductor-metal junctions based on the Blonder-Tinkham-Klapwijk formalism. Then we describe the formation of a zero-bias peak in *d*-wave superconductor-metal junctions observed in Andreev reflection, due to nodal fermions in the order parameter, which has been observed experimentally. It also supports the presence of a zero-bias mode in the computed spectral functions shown in Chapter-7. Then we discuss analytical models on gating barriers

Chapter-6 begins with an introduction to the sample fabrication methods – pick-and-place, and exfoliation techniques (see 6.1 to 6.3). The design and operation of the homebuilt glovebox pick-and-place system are presented in section 6.4. The design of the system is ergonomic and improves repeatability and reliability of the process. Sections 6.5 and 6.6 provide details on the pick-and-place and lithography techniques used in making the BSCCO/Gr and BSCCO-Gr-BSCCO heterostructures discussed here. Basic electrical characterization methods can be found in the Appendix.

Typically, resonances occur from a single scattering mechanism, for example in Andreev bound states and Yu-Shiba-Rusinov states. Our results on BSCCO/graphene junctions, discussed in **Chapter-7**, showcase resonances arising from two different scattering mechanisms – Klein tunneling and Andreev reflection, due to two naturally occurring interfaces. The device schematic details are given in 7.1. The transport data showing conductance resonances with gating and the discussion on their origin are provided in 7.2. We also provide calculations of the spectral functions and junction conductance, generated by our collaborator, which enhance the understanding of the effect of superconducting *d*-wave proximity in graphene. Additionally, the dependence of resonances on magnetic field are discussed in sections 7.3 that provide a starting point for further investigation.

Chapter-8 of the thesis extends the characterization of the resonant mechanism to BSCCO-Gr-BSCCO lateral junctions. The spacing between the BSCCO flakes that exposes graphene was made possible by a pick-and-place technique that incorporates cracking a single BSCCO, as discussed in section 6.5. We observe the period of the resonance scales inversely with the junction length ranging from 20 nm to 3 μm. Additional data on the effect of varying magnetic field on devices of different lengths is provided. This supports the reappearance of the single BSCCO-Gr junction behavior in the long BSCCO-Gr-BSCCO junctions and the robustness of resonances in the short junction junctions <1 μm.

Finally, the conclusions and outlook for this work are given in **Chapter-9**. Here we elaborate on how our results can guide new experiments to realize high-temperature GJJ and help the search for more exotic low-energy bound states, using copper oxide superconductors such as BSCCO.

1.1 References

1. Arute, F. *et al.* Quantum supremacy using a programmable superconducting processor. *Nature* **574**, 505–510 (2019).
2. Wu, Y. *et al.* Strong Quantum Computational Advantage Using a Superconducting Quantum Processor. *Phys Rev Lett* **127**, 180501 (2021).
3. Place, A. P. M. *et al.* New material platform for superconducting transmon qubits with coherence times exceeding 0.3 milliseconds. *Nat Commun* **12**, (2021).
4. Geim, A. K. & Grigorieva, I. v. Van der Waals heterostructures. *Nature* **499**, 419–425 (2013).
5. Novoselov, K. S. *et al.* Electric field in atomically thin carbon films. *Science (1979)* **306**, 666–669 (2004).
6. Jiang, Z., Zhang, Y., Tan, Y., Stormer, H. L. & Kim, P. Quantum Hall effect in graphene. **143**, 14–19 (2007).

7. Novoselov, K. S. *et al.* Two-dimensional gas of massless Dirac fermions in graphene. *Nature* **438**, 197–200 (2005).

8. Katsnelson, M. I., Novoselov, K. S. & Geim, A. K. Chiral tunnelling and the Klein paradox in graphene. *Nat Phys* **2**, 620–625 (2006).

9. Cheianov, V. v. & Fal'ko, V. I. Selective transmission of Dirac electrons and ballistic magnetoresistance of n-p junctions in graphene. *Phys Rev B* **74**, 041403 (2006).

10. Stander, N., Huard, B. & Goldhaber-Gordon, D. Evidence for Klein tunneling in graphene p-n junctions. *Phys Rev Lett* **102**, 1–4 (2009).

11. Cheianov, V. v, Fal'ko, V. & Altshuler, B. L. The focusing of electron flow and a Veselago lens in graphene p-n junctions. *Science* **315**, 1252–1255 (2007).

12. Lee, G. H., Park, G. H. & Lee, H. J. Observation of negative refraction of Dirac fermions in graphene. *Nat Phys* **11**, 925–929 (2015).

13. Heersche, H. B., Jarillo-Herrero, P., Oostinga, J. B., Vandersypen, L. M. K. & Morpurgo, A. F. Bipolar supercurrent in graphene. *Nature* **446**, 56–59 (2007).

14. ben Shalom, M. *et al.* Quantum oscillations of the critical current and high-field superconducting proximity in ballistic graphene. *Nat Phys* **12**, 318–322 (2016).

15. Borzenets, I. v. *et al.* Ballistic Graphene Josephson Junctions from the Short to the Long Junction Regimes. *Phys Rev Lett* **117**, 1–5 (2016).

16. Dirks, T. *et al.* Transport through Andreev bound states in a graphene quantum dot. *Nat Phys* **7**, 386–390 (2011).

17. Banszerus, L. *et al.* Minigap and Andreev bound states in ballistic graphene. (2020).

18. Amet, F. *et al.* Supercurrent in the quantum Hall regime. *Science (1979)* **352**, 966–969 (2016).

19. Beenakker, C. W. J. Specular andreev reflection in graphene. *Phys Rev Lett* **97**, 1–4 (2006).

20. Efetov, D. K. *et al.* Specular interband Andreev reflections at van der Waals interfaces between graphene and NbSe 2. *Nat Phys* **12**, 328–332 (2016).

21. Josephson, B. D. Possible new effects in superconductive tunnelling. *Physics Letters* **1**, 251–253 (1962).

22. Anderson, P. W. & Rowell, J. M. Probable observation of the Josephson superconducting tunneling effect. *Phys Rev Lett* **10**, 230–232 (1963).

23. Rowell, J. M. & McMillan, W. L. Electron interference in a normal metal induced by superconducting contacts. *Phys Rev Lett* **16**, 453–456 (1966).

24. Chang, H. S., Bae, M. H. & Lee, H. J. McMillan-Rowell oscillations observed in c-axis Au/Bi2Sr 2CaCu2O 8+δ junctions. *Physica C: Superconductivity and its Applications* **408–410**, 618–619 (2004).

25. Tomasch, W. J. Geometrical Resonance in the Tunneling Characteristics of Superconducting Pb. *Phys Rev Lett* **15**, 672–675 (1965).

26. Sauls, J. A. Andreev bound states and their signatures. *Philosophical Transactions of the Royal Society A: Mathematical, Physical and Engineering Sciences* **376**, 20180140 (2018).

27. Millo, O. & Koren, G. What can Andreev bound states tell us about superconductors? *Philosophical Transactions of the Royal Society A: Mathematical, Physical and Engineering Sciences* vol. 376 Preprint at https://doi.org/10.1098/rsta.2014.0143 (2018).

28. Löfwander, T., Shumeiko, V. S. & Wendin, G. Andreev bound states in high- T c superconducting junctions. *Supercond Sci Technol* **14**, R53–R77 (2001).

29. Yu, L. Bound state in superconductors with paramagnetic impurities. *Acta Physica Sinica* **21**, 75 (1965).

30. Shiba, H. Classical Spins in Superconductors. *Progress of Theoretical Physics* **40**, 435–451 (1968).

31. Rusinov, A. On the Theory of Gapless Superconductivity in Alloys Containing Paramagnetic Impurities. *Soviet Journal of Experimental and Theoretical Physics* **29**, 1101 (1969).

32. Yazdani, A., Jones, B. A., Lutz, C. P., Crommie, M. F. & Eigler, D. M. Probing the Local Effects of Magnetic Impurities on Superconductivity. *Science (1979)* **275**, 1767–1770 (1997).

33. Hu, C. R. Origin of the zero-bias conductance peaks observed ubiquitously in high superconductors. *Phys Rev B Condens Matter Mater Phys* **57**, 1266–1276 (1998).

34. Hu, C.-R. Midgap surface states as a novel signature for Midgap surface states as a novel signature for dx2-y2-wave superconductivity. *Phys Rev Lett* **72**, 1526–1529 (1994).

35. ben Shalom, M. *et al.* Quantum oscillations of the critical current and high-field superconducting proximity in ballistic graphene. *Nat Phys* **12**, 318–322 (2016).

36. Amet, F. *et al.* Supercurrent in the quantum Hall regime. *Science (1979)* **352**, 966–969 (2016).

37. di Bernardo, A. *et al.* P-wave triggered superconductivity in single-layer graphene on an electron-doped oxide superconductor. *Nat Commun* **8**, (2017).

38. Perconte, D. *et al.* Tunable Klein-like tunnelling of high-temperature superconducting pairs into graphene. *Nat Phys* **14**, 25–29 (2018).

39. Perconte, D. *et al.* Long-Range Propagation and Interference of d -Wave Superconducting Pairs in Graphene. *Phys Rev Lett* **125**, 87002 (2020).

40. Wu, Y. *et al.* The transport properties in graphene/single-unit-cell cuprates van der Waals heterostructure. *Supercond Sci Technol* **32**, (2019).

41. Sandilands, L. J. *et al.* Origin of the insulating state in exfoliated high-Tc two-dimensional atomic crystals. *Phys Rev B Condens Matter Mater Phys* **90**, 1–5 (2014).

42. Lupascu, A. *et al.* Structural study of Bi2 Sr2 CaCu2 O 8+ δ exfoliated nanocrystals. *Appl Phys Lett* **101**, 1–5 (2012).

43. Linder, J. & Sudbø, A. Tunneling conductance in s- and d-wave superconductor-graphene junctions: Extended Blonder-Tinkham-Klapwijk formalism. *Phys Rev B Condens Matter Mater Phys* **77**, 1–14 (2008).

44. Linder, J. & Sudbø, A. Dirac fermions and conductance oscillations in s- and d-wave superconductor-graphene junctions. *Phys Rev Lett* **99**, 1–4 (2007).

45. Black-Schaffer, A. M. & Doniach, S. Possibility of measuring intrinsic electronic correlations in graphene using a d -wave contact Josephson junction. *Phys Rev B Condens Matter Mater Phys* **81**, 1–5 (2010).

46. Linder, J., Black-Schaffer, A. M., Yokoyama, T., Doniach, S. & Sudbø, A. Josephson current in graphene: Role of unconventional pairing symmetries. *Phys Rev B Condens Matter Mater Phys* **80**, 1–15 (2009).

47. Black-Schaffer, A. M. Edge properties and majorana fermions in the proposed chiral d-wave superconducting state of doped graphene. *Phys Rev Lett* **109**, 1–5 (2012).

48. Black-Schaffer, A. M. & Honerkamp, C. Chiral d -wave superconductivity in doped graphene. *Journal of Physics: Condensed Matter* **26**, 423201 (2014).

49. Awoga, O. A. & Black-Schaffer, A. M. Probing unconventional superconductivity in proximitized graphene by impurity scattering. *Phys Rev B* **97**, 1–6 (2018).

2. Graphene

2.1 Introduction

The layered nature of graphite led to the invention of the pencil – a household writing instrument that has been around for centuries. Theory by P. M. Wallace[1] in 1947 predicted the unusual properties of a single atomic layer of graphite that later earned the name ‘graphene’. The isolation and characterization of graphene[2–4] by K. Novoselov & A. Geim et. al confirmed its exotic electronic properties described by the Dirac equation and was the first evidence for the existence of 2D materials. They were awarded the 2010 Nobel Prize in Physics for their out-of-the-box approach to obtaining monolayer graphene and rigorous transport studies. Since then, numerous 2D materials of different types including semiconductors, insulators, ferromagnets, superconductors, and topological insulators, etc., have been synthesized and combined in Van der Waals heterostructures[5]. Graphene continues to be ubiquitous in the research on 2D materials, just as the pencil has been essential to scribing.

“Astonishingly, graphene reincarnates itself every few years” - *Andre Geim, 2020*

Monolayer graphene was isolated from bulk graphite on SiO_2/Si wafers using 3M Scotch Tape® by K. Novoselov at the University of Manchester during a “Friday night experiment”. These experiments were meant to quickly test ideas without consuming too much time and effort. The story goes - while he was wondering how one could isolate a single atomic layer of carbon, he had seen his colleagues discard pieces of Scotch tape after exposing a fresh surface of graphite for their regular electron microscopy samples. He picked up a few of those pieces of tape and pasted them onto SiO_2 wafers in the lab. Upon peeling the tape and looking under a microscope, he discovered strips of thin layers of graphite that were translucent in appearance.

This was the beginning of many experiments to isolate monolayer graphene and study its novel electrical properties through gating and Hall transport. Research in 2D materials has retained the flavor of “Friday night” experimentation - where a naïve question and quick experiment have led to major advances and discoveries.

Section 2 introduces the atomic and electronic structure of graphene, which are needed to understand its basic transport properties in sections 3 and 4 that are relevant to our work.

2.2 Electronic Structure

Graphene is a monolayer of carbon atoms covalently bonded in a honeycomb structure. The two carbon atoms A and B in Figure 1(a) form a basis for the hexagonal lattice with vectors $\overrightarrow{a_1}$ and $\overrightarrow{a_2}$, with carbon-carbon nearest neighbor distance $a_0 = 1.42$ Å. The reciprocal lattice vectors of the Brillouin zone in Figure 1(b) are given by $\overrightarrow{b_1}$ and $\overrightarrow{b_2}$. At the corners of the Brillouin zone are the K and K’ points where the conduction and valence bands of the Dirac cone meet, commonly called the Dirac points[6].

Figure 1 (c) shows the electronic band structure and the conical dispersion at the Dirac points along the two-dimensional wave vector $\boldsymbol{k} = (k_x, k_y)$. The charge carriers in graphene are described by the massless Dirac Hamiltonian,

$$H_{K\,(or\,K')} = \hbar v_f \boldsymbol{\sigma}\ (or\ \boldsymbol{\sigma}^*) \cdot \boldsymbol{k}$$

for the K (or K’) point. Here the Fermi velocity, $v_f \approx 1 \times 10^6$ m/s and $\boldsymbol{\sigma} = (\sigma_x, \sigma_y)$ is a set of the 2×2 Pauli spin matrices. The linear dispersion relations implies that the group velocity for carriers at low energy is constant. The linear energy-momentum relationship is given by $E =$

$\pm\hbar v_f k$, unlike the parabolic relationship in semiconductors where carriers have an effective mass. Many unusual properties of quantum electrodynamics (QED) have been found in graphene owing to the relativistic nature of its carriers. Graphene is considered as a semi-metal due to its unique band structure and low carrier density of the order $n\sim10^{12}$ cm^{-2}.

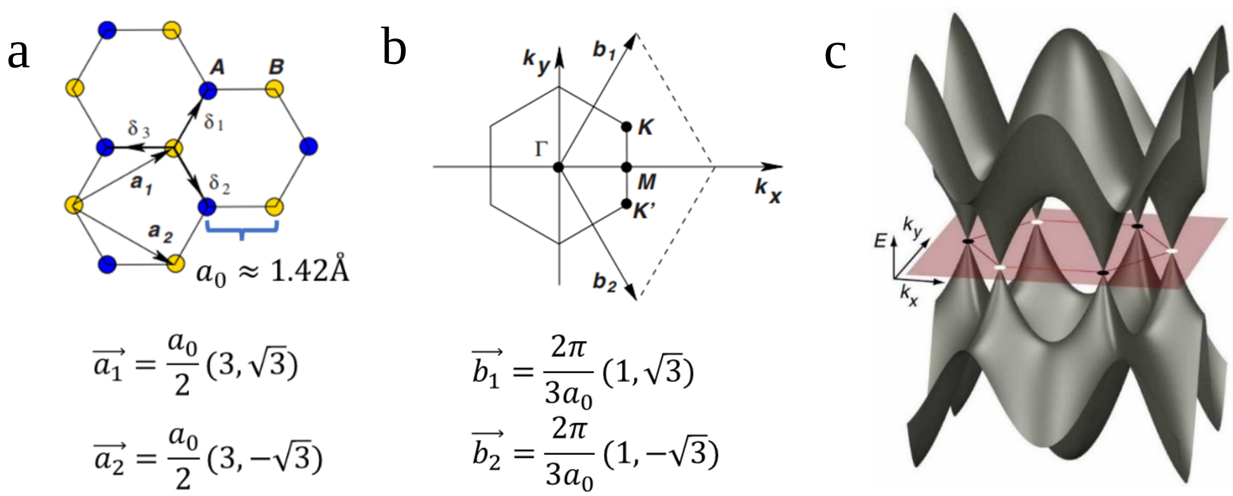

Figure 1. (a) Atomic lattice and (b) reciprocal lattice of graphene. $\delta_i, i = 1,2,3$ are the nearest-neighbor vectors. The K and K' points in the Brillouin Zone have three-fold symmetry and are the location of the Dirac cones, reproduced from [6] with permissions. (c) Electronic band structure of graphene in k_x, k_y. The Dirac cones are visible at the corners of the Brillouin zone reproduced from [26] with permissions.

We describe the tight-binding Hamiltonian using the nearest-neighbor coupling the nearest-neighbor hopping energy is $t \approx 2.7$ eV and vectors are:

$$\delta_1 = \tfrac{a_0}{2}(1, \sqrt{3}) \quad , \quad \delta_2 = \tfrac{a_0}{2}(1, -\sqrt{3}), \quad \text{and} \quad \delta_3 = a_0(-1,0).$$

The tight-binding Hamiltonian takes on the form:

$$H = -t \sum_{\langle i,j\rangle,\sigma} (c_{\sigma,i}^{\dagger}\, c_{\sigma,j} + h.c.)$$

The creation $c^\dagger$ and annihilation c operators act on the lattice sites i, j. We use this form of the tight binding Hamiltonian for single particles in the calculations of spectral functions and transport for non-superconducting graphene shown in Chapter-7.

The spin index (σ) in graphene is associated with the two sub-lattice degrees of freedom, referred to as a pseudo-spin. Spin-orbit coupling in graphene is negligible due to the small atomic number of carbon atoms. The helical nature of carriers in graphene is due to coupling between the momentum and the pseudo-spin.

2.3 Transport in Graphene

The electrical transport properties of graphene are unique due to the Dirac dispersion relation at low energy (<1 eV). It behaves like a gapless semiconductor or semi-metal which has a small carrier density that is also tunable through electrostatic gating, similar to MOSFET devices. Figure 2 shows the resistance for a monolayer graphene flake as function of gating at different temperatures. This is commonly called a "transfer curve". The peak of the resistance indicates the position of the Dirac point in gate voltage. We can estimate several other basic transport parameters such as mean free path, mobility, and carrier concentration from this measurement.

The mobility for graphene devices can be estimated using the Drude model, $\mu = \frac{v_{drift}}{E} = \frac{\sigma}{en}$, where σ is the conductivity, e is the charge constant and n is the carrier density. Graphene devices[2,7] on SiO_2 have poor mobility, when compared to suspended or encapsulated graphene, ranging from 1,300 – 15,000 $cm^2\ V^{-1}\ s^{-1}$ due to charge puddles and surface roughness[8]. Dean et al at Columbia University[9] introduced hexagonal boron nitride (h-BN) substrates for graphene, which have dramatically improved the field-effect mobility to >100,000 cm^2 V^{-1} s^{-1}. The mean free path can be estimated using the relationship $\lambda_{mfp} = \frac{h}{e^2}\frac{\sigma}{2k_f}$. Comparing λ_{mfp} with the length of the channel (L) can help us determine whether ballistic and coherent transport (if $\lambda_{mfp} > L$) of carriers are responsible for observed effects [10]. Coherent transport is expected when the dephasing length $L_\phi = \sqrt{D \times t_\phi} = \sqrt{\left(v_f \times \frac{\lambda_{MFP}}{2}\right) \times t_\phi}$ is comparable to λ_{MFP}. t_ϕ is the dephasing time for carriers in graphene, which is between 22-80 fs. We also utilize the electrostatic gating technique to characterize the BSCCO/Gr and BSCCO-Gr-BSCCO junctions. See Figure 28 (a) from Chapter-7 where we show a typical transfer curve of graphene in our devices and utilize the equation for λ_{mfp} and find it to be larger than the length of the hybrid scattering region.

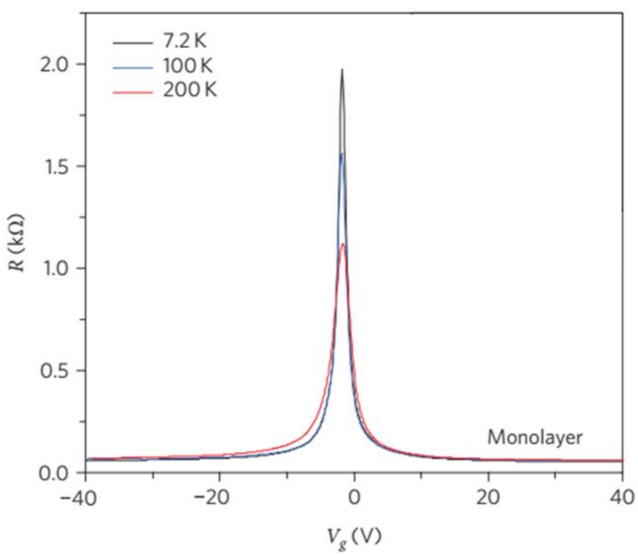

Figure 2. Longitudinal resistance of graphene on h-BN at different temperatures. Reproduced with permissions from [9].

2.4 Klein Tunneling

The Klein paradox (1929)[17] presented a surprising consequence of quantum electrodynamics - the probability for relativistic electrons to tunnel across a potential barrier is unity[18]. The massless Dirac fermions in graphene, which are responsible for charge transport and the ability to set the chemical potential (Fermi level) by electrostatic gating, posed an unprecedented opportunity to find experimental evidence for the Klein paradox[19].

A simple way to create a potential wall in graphene is to make a *p*-*n* junction using electrostatic gates, such that a positive gate voltage will induce electron (*n*) doping and a negative gate voltage will induce hole (*p*) doping. An electron above the Fermi-level in the conduction band of the *n*-side which is incident on the potential wall tunnels into the valence band of the *p*-side as a hole, see Figure 3 (a). The inter-band tunneling of Dirac fermions in graphene *p*-*n* junctions is a manifestation of Klein tunneling in a condensed matter system. Electrons and holes have longitudinal momenta ($k_e = -k_h$) that are anti-parallel with respect to the pseudo-spin σ, owing to their chiral nature[19]. Figure 3 (b) shows the trajectories for an electron incident at an oblique angle involved in Klein tunneling in graphene *n*-*p* junction, where the potential changes over a length d. Here too, we see that the longitudinal momentum of the transmitted carriers is flipped. The inversion of longitudinal momentum of transmitted carriers in a graphene *p*-*n* junction leads to another exotic effect called Veselago lensing[20].

The next parts discuss the evidence of Klein tunneling, dependence of carrier transmission on orientation angle (θ_i) and d, and the occurrence of Fabry-Pérot resonances.

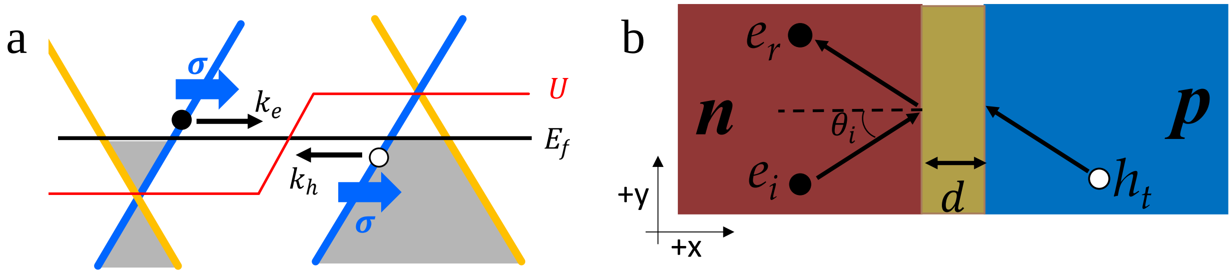

Figure 3. (a) The Dirac cones with respect to the fermi level (E_f) in a graphene *p*-*n* junction created by an extrinsic electrostatic potential (U). The blue and yellow lines highlight the linear spectrum. Electron (filled, black) states in the *n*-side tunnel through the potential step and becomes a hole (unfilled, white) in the *p*-side. (b) Schematic of the trajectories of an incident electron (e_i), the partially transmitted hole (h_t), and reflected electron (e_r) components in a graded graphene *p*-*n* junction.

Evidence for Klein Tunneling was found in transport measurements across a tunable potential barrier in graphene[7,21] created using a top gate. The four-terminal resistance was measured as device was tuned from unipolar (*p*-*p*-*p* or *n*-*n*-*n*) to bipolar (*p*-*n*-*p* or *n*-*p*-*n*) using both top and bottom gates. The resistance of the bipolar junction was found to be higher than the unipolar junction in various devices. The total resistance in the bipolar regime (200 to 600 Ω) is the sum of the resistance for two *p*-*n* junctions in series. In addition, they showed that increasing the length of the barrier beyond the l_{mfp} resulted in a deviation from theoretical predictions due to increase in diffusive transport. The main result from these studies is the increase (decrease) in resistance (conductance) going from *p*-*p* to *p*-*n*, which we refer to as the "conductance asymmetry", a recognizable feature of Klein tunneling in graphene devices. This asymmetry was calculated to be 2/3 in abrupt *p*-*n* junctions by Low, T. et al *IEEE Trans. Electron Devices* (2009). The conductance asymmetry is also seen in our single BSCCO/Gr junctions discussed in Chapter-7.

The transmission of carriers through a *p*-*n* junction in graphene also depends on the angle of incidence[22]. Carriers are 100% transmitted at normal incidence ($\theta_i = 90°$) to the *p*-*n* interface. This case of perfect tunneling is possible because the carriers conserve their pseudo-spin. In Figure 3 (b), an electron is incident on a region of graded p-n junction of length *d* with momentum vectors (k_x, k_y). An electron that is incident at an oblique angle from the *n*-side partially transmits as a hole $(-k_x, k_y)$ into the *p*-side by Klein tunneling and the remaining component reflects as an electron $(-k_x, k_y)$. In this process, the longitudinal momentum of the transmitted hole is reversed, but the transverse momentum is conserved. The transmission probability decays as $T \propto e^{-(\sin\theta_i)^2}$, meaning more carriers are reflected as the angle of incidence becomes more oblique. Furthermore, abrupt *p*-*n* junctions are not always easy to realize in devices due to fabrication challenges and fringe-field effects. The change in potential across the graded *p*-*n* junction, further decreases the transmission probability according to the relation $T(\theta_i) = e^{-\pi d k_F \sin{\theta_i}^2}$. The increase in resistance for sub-micron wide graphene p-n junctions oriented at 45° to split-gates[23] provided evidence for the angle dependent transport, see Figure 4. The junction resistance was extracted by removing the channel resistances. The buried poly-silicon gates were independently controlled to go from unipolar (*p*-*p* or *n*-*n*) to ambipolar (*p*-*n* or *n*-*p*) regimes. The junction resistance is higher for narrower width channels because fewer modes are available for transport.

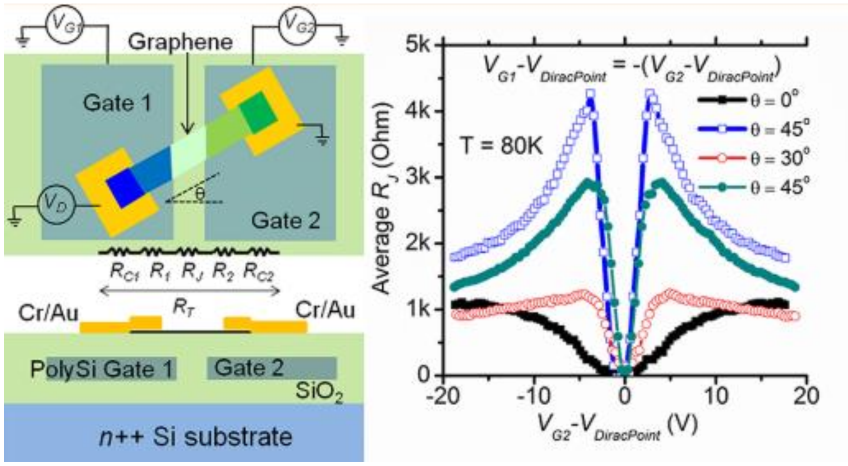

Figure 4. In the left panel is the schematic of the device. Graphene of finite width (≤1 μm) is on a dielectric with two buried split gates which can independently tune the carrier concentration to create a *p-n* junction. In the right panel is the resistance of the *p-n* junction, after removing other series resistances. Perfect transmission (lowest resistance) was observed at normal incidence ($\theta = 0°$). The resistance increased to maximum as the orientation of the graphene channel was increased to $\theta = 45°$, due to reduced transmission. Reprinted (adapted) with permission from [23] Copyright 2012 American Chemical Society.

Furthermore, abrupt *p-n* junctions are not always easy to realize in devices due to fabrication challenges and fringe-field effects. The change in potential across a graded *p-n* junction, further decreases the transmission probability according to the relation $T(\theta_i) = e^{-\pi d k_F \sin\theta_i{}^2}$. The increase in resistance for sub-micron wide graphene *p-n* junctions oriented at 45° to split-gates[23] provided evidence for the angle dependent transport, see Figure 4. The buried poly-silicon gates were independently controlled to go from unipolar (*p-p* or *n-n*) to ambipolar (*p-n* or *n-p*) regimes.

In another study, two parallel *p-n* interfaces of bipolar graphene (*p-n-p* or *n-p-n*) junctions act as partially reflecting mirrors and create Fabry-Pérot resonances[24], which are traditionally associated with interference in optical cavities. The trajectories of carriers scattering between the two *p-n* interfaces at zero and non-zero magnetic fields are shown in Figure 5 (a) and (b), respectively. At zero field, the change in incidence angle α from positive to negative cancels any contribution to the phase gained by carriers between reflections. However, the curved carrier trajectories due to a magnetic field, shown in Figure 5 (b), can result in the same sign for incidence angles and carrier gain additional phase at every reflection. Young et al fabricated *p-n-p* junctions with a small barrier region $L \sim 20$ nm and large mean free path $l_{mfp} \geq 100$ nm[25] and examined conductance oscillations from the Fabry-Perot process and showed their sensitivity to magnetic field, depicted in Figure 5 (b). In S-Gr-S junctions presented in Chapter-8, we observe shift in oscillations with gating, which can be due to a similar mechanism discussed here.

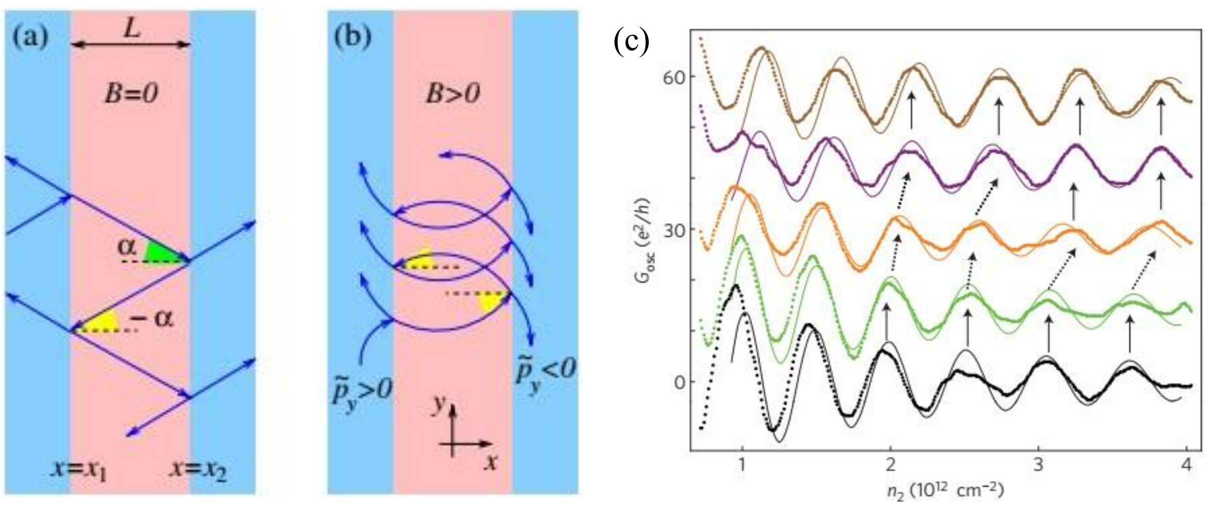

Figure 5. Trajectories of carriers undergoing back-reflection and resulting in a Fabry-Perot interference without (a) and with (b) magnetic field. These are reproduced with permission from[24]. (c) Conductance oscillations, reproduced with permissions from[25], as a function of carrier density (n_2) in the potential barrier of a bipolar graphene junction from 0 (black), 200, 400, 600, and 800 (brown) mT.

The basic electronic properties and results from transport studies of graphene covered in this chapter have been essential for analyzing our results.

References

1. Wallace, P. R. The Band Theory of Graphite. Physical Review 71, 622–634 (1947).
2. Novoselov, K. S. et al. Two-dimensional gas of massless Dirac fermions in graphene. Nature 438, 197–200 (2005).
3. Geim, A. K. & Novoselov, K. S. The rise of graphene. Nat Mater (2007) doi:10.1038/nmat1849.
4. Novoselov, K. S. et al. Electric field in atomically thin carbon films. Science (1979) 306, 666–669 (2004).
5. Geim, A. K. & Grigorieva, I. v. Van der Waals heterostructures. Nature 499, 419–425 (2013).
6. Castro Neto, A. H., Guinea, F., Peres, N. M. R., Novoselov, K. S. & Geim, A. K. The electronic properties of graphene. Rev Mod Phys 81, 109–162 (2009).
7. Stander, N., Huard, B. & Goldhaber-Gordon, D. Evidence for Klein tunneling in graphene p-n junctions. Phys Rev Lett 102, 1–4 (2009).
8. Martin, J. et al. Observation of electron–hole puddles in graphene using a scanning single-electron transistor. Nat Phys 4, 144–148 (2008).
9. Dean, C. R. et al. Boron nitride substrates for high-quality graphene electronics. Nat Nanotechnol 5, 722–726 (2010).
10. Datta, S. Electronic Transport in Mesoscopic Systems. (Cambridge University Press, 1995). doi:10.1017/CBO9780511805776.
11. Klitzing, K. v., Dorda, G. & Pepper, M. New method for high-accuracy determination of the fine-structure constant based on quantized hall resistance. Phys Rev Lett 45, 494–497 (1980).
12. von Klitzing, K. et al. 40 years of the quantum Hall effect. Nature Reviews Physics 2, 397–401 (2020).
13. Finkelstein, G. & Amet, F. When Andreev meets Hall. Nat Phys 13, 625–626 (2017).
14. San-Jose, P., Lado, J. L., Aguado, R., Guinea, F. & Fernández-Rossier, J. Majorana zero modes in graphene. Phys Rev X 5, 1–15 (2015).
15. Lee, G. H. et al. Inducing superconducting correlation in quantum Hall edge states. Nat Phys 13, 693–698 (2017).
16. Amet, F. et al. Supercurrent in the quantum Hall regime. Science (1979) 352, 966–969 (2016).
17. Klein, O. Die Reflexion von Elektronen an einem Potentialsprung nach der relativistischen Dynamik von Dirac. Zeitschrift für Physik 53, 157–165 (1929).
18. Greiner, W., Müller, B. & Rafelski, J. The Klein Paradox. in Quantum Electrodynamics of Strong Fields 112–121 (Springer Berlin Heidelberg, 1985). doi:10.1007/978-3-642-82272-8_5.
19. Katsnelson, M. I., Novoselov, K. S. & Geim, A. K. Chiral tunnelling and the Klein paradox in graphene. Nat Phys 2, 620–625 (2006).
20. Cheianov, V. v, Fal'ko, V. & Altshuler, B. L. The focusing of electron flow and a Veselago lens in graphene p-n junctions. Science 315, 1252–1255 (2007).
21. Huard, B. et al. Transport measurements across a tunable potential barrier in graphene. Phys Rev Lett 98, 8–11 (2007).

22. Cheianov, V. V. & Fal'ko, V. I. Selective transmission of Dirac electrons and ballistic magnetoresistance of n-p junctions in graphene. Phys Rev B 74, 041403 (2006).

23. Sutar, S. et al. Angle-dependent carrier transmission in graphene p-n junctions. Nano Lett 12, 4460–4464 (2012).

24. Shytov, A. V., Rudner, M. S. & Levitov, L. S. Klein Backscattering and Fabry-Pérot Interference in Graphene Heterojunctions. Phys Rev Lett 101, 156804 (2008).

25. Young, A. F. & Kim, P. Quantum interference and Klein tunnelling in graphene heterojunctions. Nat Phys 5, 222–226 (2009).

26. Beenakker, C. W. J. Colloquium: Andreev reflection and Klein tunneling in graphene. Rev Mod Phys 80, 1337–1354 (2008).

3. Superconductivity

This chapter introduces the basic properties and classifications of superconductors that are required to describe the experimental work discussed later on.

3.1 Introduction

The four-terminal resistance measurement of a conductor is the voltage dropped along a length of the conductor divided by the current flowing through it. The schematics in Figure 6 (a) and (b) show the circuit used to measure the resistance of a normal metal (R_N) and a superconductor (R_S). Figure 6 (c) shows a representative plot of R_N (gray), which shows a decrease in resistance with reduced temperature due to the reduction in thermal scattering from lattice vibrations. $R_N > 0\ \Omega$ even close to zero temperature due to imperfections and impurities. Interestingly, when a superconductor (green) is below the critical temperature (T_C), it undergoes a macroscopic phase transition from a state with finite resistance to a state of zero resistance, $R_S = 0\ \Omega$, first discovered by H. K. Onnes in 1911.

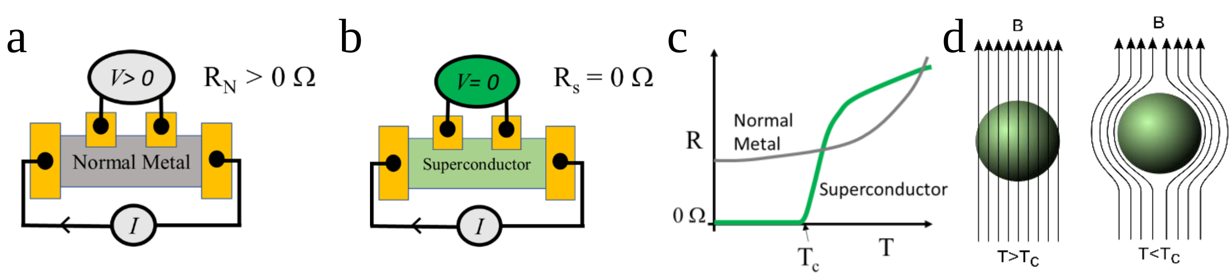

Figure 6. (a) A normal metal has a finite resistance. (b) Whereas, a SC has no resistance below critical temperature, current and magnetic field. (c) Schematic of the resistance of a superconductor (green) and a normal metal (gray). (d) Magnetic field (left) permitted and (right) expelled by a superconductor exhibiting the Meissner effect.

The current flowing through the superconductor is commonly called a “supercurrent” and is carried by Cooper pairs[1] – which are paired electrons (or holes) of opposite spin and momenta. The transport of Cooper pairs is without dissipation up to a critical limit I_C, beyond which Cooper pairs are broken. Another distinguishing feature of a superconductor is that it is a perfect diamagnetic, up to a critical field (H_C), i.e., it expels the magnetic field[2]. This is called the Meissner effect and is shown in Figure 6(d).

3.2 Classification for Superconductors

Superconductors can be classified based on their transition temperature, properties under an external magnetic field, and the symmetry of the superconducting order parameter. These classifications are discussed below and help us understand the properties of BSCCO.

3.2.1 Transition Temperature

The cryogens required to reach critical temperatures are a basis for generally categorizing superconductors. Low-temperature superconductors have T_C accessible with liquid helium which has a boiling point of 4.2 K at atmospheric pressure. Elemental superconductors like Al, Hg, Pb and Nb were some of the earliest materials identified with superconducting properties. Some alloyed superconductors like MoRe, NbN, and layered $NbSe_2$ ($T_C > 4.2$ K) are also low-temperature superconductors. A material is regarded as high-temperature superconductor when its T_C is above the boiling point of nitrogen (77.2 K), for example - cuprate superconductors. Furthermore, materials are being explored for superconductivity at room-temperature without the need for special conditions like applying a high pressure. T_C can be easily determined electrically by measuring the resistance of the material as a function of temperature. Measuring the magnetic susceptibility is another way, where a negative value arises at the onset of superconductivity due to diamagnetism. In tunneling studies, a superconducting gap begins to form below T_C. We rely on the resistance measurement to find the T_c of BSCCO in our devices and have used tunnel contacts to measure its superconducting gap.

3.2.2 Magnetic Field

The properties of superconductors in an external magnetic field can be explained by the Ginzburg-Landau theory [2,3]. The main achievement of this theory was explaining the coexistence of superconducting and normal domains in near the critical fields. The two quantities that determine the Ginzburg-Landau parameter $\kappa = \frac{\lambda_L}{\xi_s}$ are: λ_L is the London penetration depth of an external magnetic and $\xi_s \approx \frac{\hbar v_f}{\Delta_0}$ is the superconducting coherence length.

- The type-I superconductor preserves its superconductivity up to a single critical field, H_C, exhibiting the Meissner effect. Superconductivity is suddenly broken at fields above H_C – dashed line in Figure 7 (a). Hg, Al, and Pb (typically films of a single element) are examples of type-I superconductors. Due to their long coherence length, $\kappa < \frac{1}{\sqrt{2}}$.
- The type-II SC also exhibits the Meissner effect up to a critical field H_{C1}. Above H_{C1}, magnetic field penetrates the superconductor in the form of Abrikosov vortices, up to a large second critical field H_{C2} without completely breaking superconductivity, see Figure 7 (a). In this intermediate state, superconducting domains coexist with the normal vortices. One Abrikosov vortex permits a single quantum of magnetic flux $\Phi_0 = \frac{h}{2e} \approx 2 \times 10^{-15}$ T m^{-2}, see Figure 7 (b). The center of the vortex is normal, and a supercurrent circulates at the boundary. Abrikosov vortices can arrange themselves in a closed packed lattice and bind to

defects. Above H_{C2}, the entire material becomes normal. Alloys such as NbN, MoRe, YBCO, and BSCCO are examples of type-II superconductors with $\kappa > \frac{1}{\sqrt{2}}$.

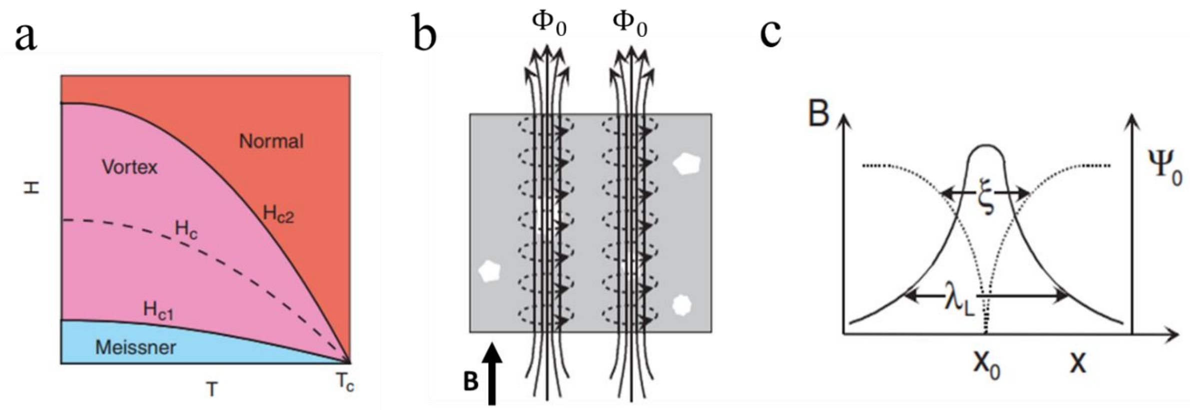

Figure 7. (a) Schematic phase diagram for superconductors with respect to magnetic field and temperature. Reproduced from Kopnin, Nikolai B. "Introduction to The Theory of Superconductivity Cryocourse" 2009 Helsinki, Finland. (b) Cross section schematic of Abrikosov vortices permitting a flux quantum through the superconductor and the circulating super current in dashed lines. (c) The London penetration length (solid) vs. B and coherence length (dashed) vs. the superconducting wave function from the center of the vortex. (b) and (c) adapted from Kleiner, R. and Koelle, D. (2004).

3.2.3 Symmetry of Order Parameter

Another classification is on the spatial symmetry of the order parameter. Its symmetry has interesting consequence to the mesoscopic tunneling mechanisms in S-N junctions, which is discussed later in Chapter-5.

The *s*-wave order parameter is isotropic and has a finite superconducting gap energy (Δ), seen in most type-I superconductors, which are considered conventional superconductors according to the BCS theory. Left panel in Figure 8 shows the uniform *s*-wave order parameter (top) and the corresponding single particle density of states (bottom).

The d-wave order parameter is anisotropic, i.e., the gap energy is direction-dependent. The superconducting gap vanishes along the nodes and reaches maximum along the lobes; it is therefore called a pseudo-gap, see right panel of Figure 8. The phase of the pair potential oscillates between positive and negative phases in the dumbbell shaped lobes of the order parameter[4]. Two variations for the d-wave order parameters are - $d_{x^2-y^2}$ and d_{xy}. The latter is oriented at 45° with respect to axes, whereas the formed is oriented along the. The lobes are oriented along the [100] and [010] directions in the case of $d_{x^2-y^2}$. Cuprates are examples of d-wave superconductors.

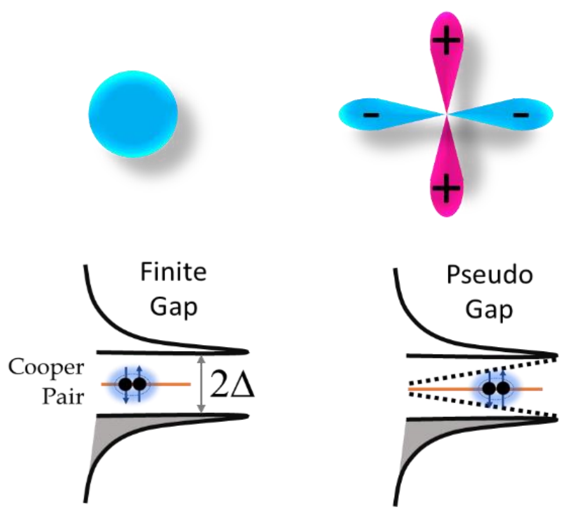

Figure 8. (Top) Representation of an s-wave and d-wave order parameter. The phase of the d-wave lobes alternates from positive (pink) to negative (blue). (Bottom) Density of states of the superconducting gap for s-wave has a fixed gap (left). Single particle states are absent within the superconducting gap. The d-wave gap is maximum along the lobes and zero in the nodes, referred to as a pseudogap (right). Cooper pairs exist at the Fermi level in orange, but single particles are present away from zero energy.

References

1. Bardeen, J., Cooper, L. N. & Schrieffer, J. R. Theory of Superconductivity. *Physical Review* **108**, 1175–1204 (1957).

2. Tinkham, M. *Introduction to Superconductivity: Second Edition*. (Dover Publications, 2004).

3. De Gennes, P. G. *Superconductivity of Metals and Alloys*. *Superconductivity of Metals and Alloys* (CRC Press, 2018). doi:10.1201/9780429497032.

4. Hu, C.-R. Midgap surface states as a novel signature for Midgap surface states as a novel signature for $d_{x^2-y^2}$-wave superconductivity. *Phys Rev Lett* **72**, 1526–1529 (1994).

4. $Bi_2Sr_2CaCu_2O_{8+x}$

4.1 Introduction

The discovery of high-temperature cuprate superconductors (HTCS) in 1986 [1] opened doors for the exploration of superconducting effects beyond what was known in s-wave superconductors. In the decade following the discovery, many studies on the pairing symmetry established several cuprate superconductors to be singlet *d*-wave[2] through experiments on SQUID microscopy[3,4], Josephson junctions[5] and Andreev reflection[6]. Although superconductivity was identified to exist in the Cu-O planes of HTCS, the exact reasons for its occurrence are yet to be explained[7]. The Cu-O planes are doped by the surrounding layers, which function as charge reservoirs to contribute (electron-doped) or extract (hole-doped) electrons[8,] which participate in the phase transition to superconductivity. $YBa_2Cu_3O_{7-x}$ (YBCO) and $Bi_2Sr_2CaCu_2O_{8+x}$ (BSCCO) are hole-doped superconductors whose T_c can be four times higher than that of electron-doped cuprate superconductor such as $Pr_{1.85}Ce_{0.15}CuO_{4-x}$ (PCCO, T_c ~ 22 K)[7]. For transport studies, making clean ohmic contact to these materials is difficult because their exposed surfaces can quickly become insulating. Since BSCCO is a layered material and large-area crystals can be exfoliated using the scotch-tape method, it is an optimal candidate for us to combine with graphene using dry stamping techniques.

In this section, we elucidate on the specific material and electronic properties of BSCCO. The key results which established *d*-wave superconductivity in BSCCO are discussed to support our treatment of *d*-wave superconducting proximity effects in BSCCO/graphene junctions. Then, the doping-dependent electronic phase diagram of BSCCO (1-2.5-unit cells) developed through ionic gating is discussed. This gives context to the degradation of its superconducting properties.

4.2 Properties

$Bi_2Sr_2CaCu_2O_{8+x}$, commonly called Bi-2212, is a quintenary alloy made of bismuth, strontium, calcium, copper, and oxygen. The orthorhombic single unit cell (c = 3.07 Å) of BSCCO is comprised of two monolayers that are separated by a Van der Waals (VdW) gap shown in Figure 9, which is not present in other HTCS. This layered nature allows us to mechanically exfoliate large-area crystals of BSCCO using the scotch-tape method, similar to graphene[9].

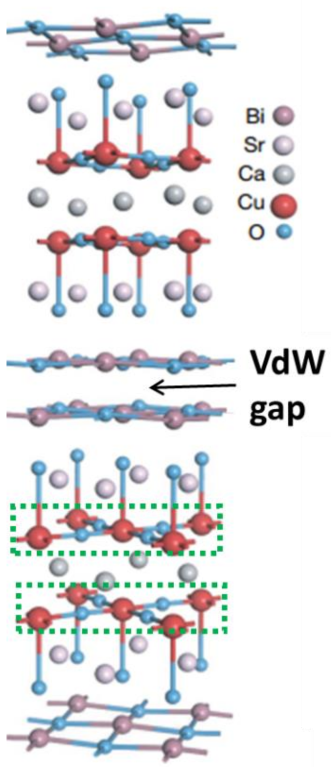

Figure 9. Crystal structure of BSCCO reproduced with permission from Yu et al.[10] (2019), showing a single unit cell comprised of two monolayers which are separated by a VdW gap. The dotted green boxes are added to highlight the Cu-O layers which are host to superconductivity. The surrounding layers aid the Cu-O layer by donating carriers.

As expected for an alloyed material, it is a type-II superconductor with a high T_c ~ 85 K and carrier concentration of the order $n{\sim}10^{15}$ cm^{-2}. Recently, T_c in a monolayer of BSCCO[10] was measured to be comparable to optimally doped bulk samples. The true two-dimensionality of superconductivity in BSCCO defies Hohenberg-Mermin-Wagner theorem[11,12], unlike the reduced T_c in monolayer $NbSe_2$[13]. The theorem suggested that long-range order, such as superconductivity and ferromagnetism, vanishes in one and two dimensions due to interactions from surrounding short-range disorder.

The size of the superconducting pseudo-gap is $40 < \Delta < 50$ meV in high-quality BSCCO[10,14,15]. The 2D superconductivity in BSCCO manifests a large difference in the coherence lengths in the a-b plane as compared to c-axis, i.e., $\xi_{ab} = 2\ nm > \xi_c = 0.1\ nm$. The short coherence lengths set limitations on the distance over which superconductivity can persist in materials in contact with BSCCO. Proximity-induced superconductivity from BSCCO has been possible in layered materials with low diffusion coefficients ($D = v_f \times \frac{\lambda_{mfp}}{2}$) and small carrier density[16], such as graphene and topological insulators. These observations from experiments on Andreev reflections are discussed in Chapter 5.

ARPES [17] and tunneling experiments[6] on cuprate superconductors were successful in finding the anisotropy and size of the order parameter. SQUID loops of YBCO-Au-Pb[18] demonstrated the π phase shift of the critical current due to the *d*-wave pairing in YBCO. The oscillating phase of the *d*-wave order parameter for cuprates was explored using scanning SQUID microscopy of superconducting rings (YBCO)[3] and Josephson weak-links[4] (BSCCO) where a spontaneous (without an external magnetic field) half-integer flux quantum was generated at tri-crystal junctions. This is due to the odd number of sign changes of the pairing current in the weak-link. In more recent experiments, *d*-wave Cooper wave density was spatially mapped in BSCCO using scanning Josephson tunneling microscopy[19]. Another unexpected result from Andreev reflection in BSCCO-metal junctions is the occurrence of a zero-bias peak [20] arising from single particles along the nodes[21,22]. Based on the cumulative evidence, it is believable that the superconducting pairing symmetry in BSCCO is *d*-wave.

Changes in carrier densities in BSCCO have been possible by ionic gating [14,23]. Since the carrier density in BSCCO is on the order of 10^{15} cm^{-2}, one would need special gating techniques to alter the BSCCO properties, such as the use of liquid or solid ionic gates which rely on ion (Li^{+}, Ca^{+}, Al^{+}) intercalation. Using a 90 nm SiO_2 layer, as in our study, we can induce carrier densities of order 10^{12} cm^{-2}, at least two orders of magnitude lower than that needed to affect BSCCO. The electronic phase diagram for thin layers of BSCCO as a function of temperature and hole doping is shown in Figure 10.

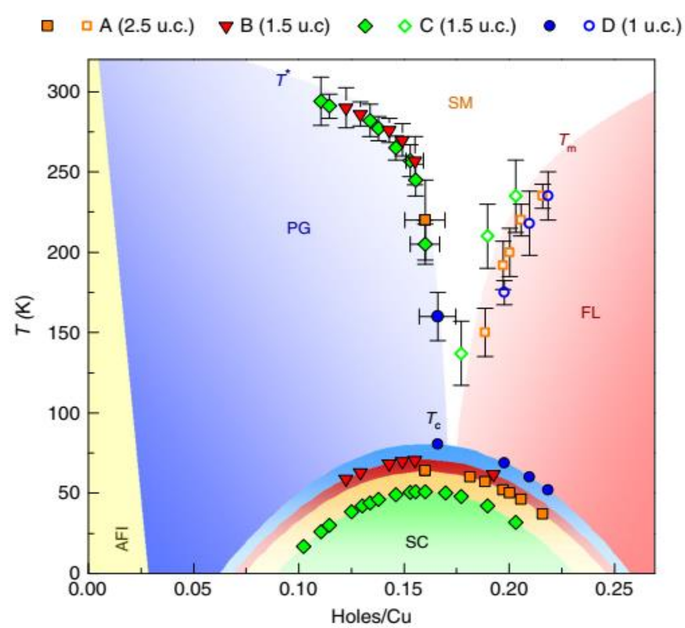

Figure 10. Phase diagram of BSCCO as a function of temperature and hole concentration adapted from [23] (open access). The resistance of BSCCO samples ranging in thickness from 1 unit-cell to 2.5 unit-cells were measured as a function of temperature at different doping controlled by solid ion gating method.

At low hole doping (<0.025), an anti-ferromagnetic insulator (AFI) state is known to exist in BSCCO[24]. The loss of oxygen from layers of BSCCO reduces the hole doping necessary for the superconducting (SC) phase to form at low temperature[25,26]. Without special steps to protect the surfaces of BSCCO, it is commonly found that a finite thickness (5-15 nm) film becomes insulating by loss of oxygen. Degradation is worse upon exposure to water vapor at room temperature[25,26]. The formation of an insulating layer on unprotected surfaces also makes it difficult to achieve ohmic contacts using conventional lithography techniques. Recent studies on

BSCCO have developed fabrication techniques in inert glovebox systems[27,28] at low temperature[29–31] and utilized maskless lithography methods[23,30,32] to create ohmic contacts. Based on recent progress, we were convinced to develop glovebox fabrication capabilities and lithography processes to achieve ohmic contacts to BSCCO.

The superconducting (SC) state is found between doping of 0.05 to 0.27, with T_C ranging from 30 K (low and high doped) to 85 K (optimal). Above T_c, in the underdoped regime (0.1-0.15), there is a pseudo-gap (PG) phase characterized by a non-linear change in resistivity with temperature. At optimal doping around 0.15, there is a phase termed as strange metal (SM), which has 100X resistivity of conventional metals and is a general property of HTCS behaving as strongly correlated electron systems[8]. Lastly, above Tc and in the over-doped regime (0.15-0.2) there is a power law dependence of resistivity with temperature as evidence for the metallic fermi-liquid (FL) state. The elaborate phase diagram for BSCCO, and cuprates in general[8], is an active area of research.

In this work, we are concerned with the superconducting properties of bulk BSCCO at low temperatures (4.2 - 77 K). The T_C of BSCCO in most of our devices (77-85 K) is comparable to optimal samples in the reports discussed above. Our tunneling experiment on BSCCO also found a comparable magnitude for the superconducting gap, $\Delta \sim 40$ meV, see Appendix A.2

Tunneling measurements of BSCCO

References

1. Bednorz, J. G. & Müller, K. A. Possible high-Tc superconductivity in the Ba-La-Cu-O system. *Zeitschrift für Physik B Condensed Matter* **64**, 189–193 (1986).
2. Tsuei, C. C. & Kirtley, J. R. Pairing symmetry in cuprate superconductors. *Physica C Supercond* **341–348**, 1625–1628 (2000).

3. Tsuei, C. C. *et al.* Pairing Symmetry and Flux Quantization in a Tricrystal Superconducting Ring of $YBa_2Cu_3O_{7-\delta}$. *Phys Rev Lett* **73**, 593–596 (1994).

4. Tsuei, C. C. *et al.* Half-integer flux quantum effect in tricrystal cuprate superconductors. *Physica C Supercond* **263**, 232–237 (1996).

5. Keene, M. N., Jackson, T. J. & Gough, C. E. Demonstration of the phase coherence of the superconducting wavefunctions between conventional and high-T_c superconductors. *Nature* **340**, 210–211 (1989).

6. Hoevers, H. F. C. *et al.* Determination of the energy gap in a thin $YBa_2Cu_3O_{7-x}$ film by Andreev reflection and by tunneling. *Physica C Supercond* **152**, 105–110 (1988).

7. Tsuei, C. C. & Kirtley, J. R. *d*-wave pairing symmetry in cuprate superconductors. *Physica C: Superconductivity and its Applications* **341–348**, 1625–1628 (2000).

8. Keimer, B., Kivelson, S. A., Norman, M. R., Uchida, S. & Zaanen, J. From quantum matter to high-temperature superconductivity in copper oxides. *Nature* vol. 518 179–186 Preprint at https://doi.org/10.1038/nature14165 (2015).

9. Novoselov, K. S. *et al.* Two-dimensional atomic crystals. *Proc Natl Acad Sci U S A* **102**, 10451–10453 (2005).

10. Yu, Y. *et al.* High-temperature superconductivity in monolayer $Bi_2Sr_2CaCu_2O_{8+\delta}$. *Nature* **575**, 156–163 (2019).

11. Mermin, N. D. & Wagner, H. Absence of Ferromagnetism or Antiferromagnetism in One- or Two-Dimensional Isotropic Heisenberg Models. *Phys Rev Lett* **17**, 1133–1136 (1966).

12. Hohenberg, P. C. Existence of long-range order in one and two dimensions. *Physical Review* **158**, 383–386 (1967).

13. Frindt, R. F. Superconductivity in Ultrathin $NbSe_2$ Layers. *Phys Rev Lett* **28**, 299–301 (1972).

14. Liao, M. *et al.* Superconductor-Insulator Transitions in Exfoliated $Bi_2Sr_2CaCu_2O_{8+\delta}$ Flakes. *Nano Lett* **18**, 5660–5665 (2018).

15. Hoogenboom, B. W., Kadowaki, K., Revaz, B. & Fischer. Homogeneous samples of $Bi_2Sr_2CaCu_2O_{8+\delta}$. *Physica C: Superconductivity and its Applications* **391**, 376–380 (2003).

16. Deutscher, G. & Simon, R. W. On the proximity effect between normal metals and cuprate superconductors. *J Appl Phys* **69**, 4137–4139 (1991).

17. Shen, Z.-X. *et al.* Anomalously large gap anisotropy in the a **-** b plane of $Bi_2Sr_2CaCu_2O_{8+\delta}$. *Phys Rev Lett* **70**, 1553–1556 (1993).

18. Wollman, D. A., Van Harlingen, D. J., Lee, W. C., Ginsberg, D. M. & Leggett, A. J. Experimental determination of the superconducting pairing state in YBCO from the phase coherence of YBCO-Pb dc SQUIDs. *Phys Rev Lett* **71**, 2134–2137 (1993).

19. Hamidian, M. H. *et al.* Detection of a Cooper-pair density wave in $Bi_2Sr_2CaCu_2O_{8+x}$. *Nature* **532**, 343–347 (2016).

20. Sinha, S. & Ng, K. W. Zero bias conductance peak enhancement in $Bi_2Sr_2CaCu_2O_{8+\delta}$/Pb tunneling junctions. *Phys Rev Lett* **80**, 1296–1299 (1998).

21. Hu, C.-R. Midgap surface states as a novel signature for Midgap surface states as a novel signature for dx2-y2-wave superconductivity. *Phys Rev Lett* **72**, 1526–1529 (1994).

22. Kashiwaya, S. & Tanaka, Y. Theory for tunneling spectroscopy of anisotropic superconductors. *Phys Rev B* **53**, 2667–2676 (1996).

23. Sterpetti, E., Biscaras, J., Erb, A. & Shukla, A. Comprehensive phase diagram of two-dimensional space charge doped $Bi_2Sr_2CaCu_2O_{8+x}$. *Nat Commun* **8**, 2060 (2017).

24. Moudden, A. H., Vasiliu-Doloc, L., Blanchard, N., Collin, G. & Hammann, J. Evidence of antiferromagnetic ordering of Cu2+ spins in non-superconducting Bi-2212. *Physica C: Superconductivity and its applications* **235–240**, 1621–1622 (1994).

25. Sandilands, L. J. *et al.* Stability of exfoliated $Bi_2Sr_2Dy_xCa_{1-x}Cu_2O_{8+\delta}$ studied by Raman microscopy. *Phys Rev B* **82**, 064503 (2010).

26. Sandilands, L. J. *et al.* Origin of the insulating state in exfoliated high-T_c two-dimensional atomic crystals. *Phys Rev B* **90**, 1–5 (2014).

27. Zareapour, P. *et al.* Proximity-induced high-temperature superconductivity in the topological insulators Bi_2Se_3 and Bi_2Te_3. *Nat Commun* **3**, (2012).

28. Zareapour, P. *et al.* Evidence for a new excitation at the interface between a high-T_c superconductor and a topological insulator. *Phys Rev B* **90**, (2014).

29. Koelle, D., Kleiner, R., Ludwig, F., Dantsker, E. & Clarke, J. High-transition-temperature superconducting quantum interference devices. *Rev Mod Phys* **71**, 631–686 (1999).

30. Zhao, S. Y. F. *et al.* Emergent Interfacial Superconductivity between Twisted Cuprate Superconductors. (2021).

31. Saito, S. *et al.* Comparison of $Bi_2Sr_2CaCu_2O_8$ surfaces cleaved at low temperature and at room temperature from secondary ion mass spectrometry and work function measurements. *Physica Status Solidi (A) Applications and Materials Science* **202**, 129–131 (2005).

32. Zhao, S. Y. F. *et al.* Sign-Reversing Hall Effect in Atomically Thin High-Temperature $Bi_{2.1}Sr_{1.9}CaCu_{2.0}O_{8+\delta}$ Superconductors. *Phys Rev Lett* **122**, 247001 (2019).

5. Superconductor-Graphene Heterojunctions

The confirmation of semi-metallic band structure in graphene (Gr) governed by the Dirac equation prompted the quest for new transport phenomena in superconductor-Gr junctions[1]. The goal of this chapter is to convey a basic theoretical and experimental background on the transport properties of SC-Gr junctions. The chapter begins with a brief discussion of Andreev reflection (AR) in conventional SC-NM junctions. Then, we will look at how AR in graphene changes with energy and review an experiment aimed at finding evidence for this. Finally, we will see how varying a gate-tunable barrier at the SC-Gr interface, both theoretically and experimentally, contributes to conductance oscillations.

5.1 Transport in Superconductor-Metal Junctions

Charge transport in SC-NM junctions can be described by a tunneling mechanism called Andreev reflection (AR). The trajectories of carriers involved in this process are shown in Figure 11 (a). An electron from a normal metal that enters a superconductor at energy $\varepsilon < \Delta$ combines with another electron to form a Cooper pair and reflects a hole into the metal. The NM-SC interface is not always ideal and will contain imperfections that become barriers to electron transport. These barriers impede the probability of AR across the NM-SC interface. The Blonder-Tinkham-Klapwijk (BTK)[2] formalism quantified the barrier using a dimensionless quantity Z. In an NM-SC junction, where the barrier is absent $(Z = 0)$, AR occurs with unit probability, and the conductance doubles for sub-gap excitation energies $\varepsilon \leq \Delta$. As the barrier height is increased $(0 < Z < 1)$, the conductance gradually reduces because AR decreases. For large barrier heights $(Z > 1)$, AR is almost null and leads to a dramatic drop in conductance for sub-gap energies and looks like the case for tunneling through an insulator (I) in NM-I-SC. See panels (b) and (c) of Figure 11 showing the Z dependence.

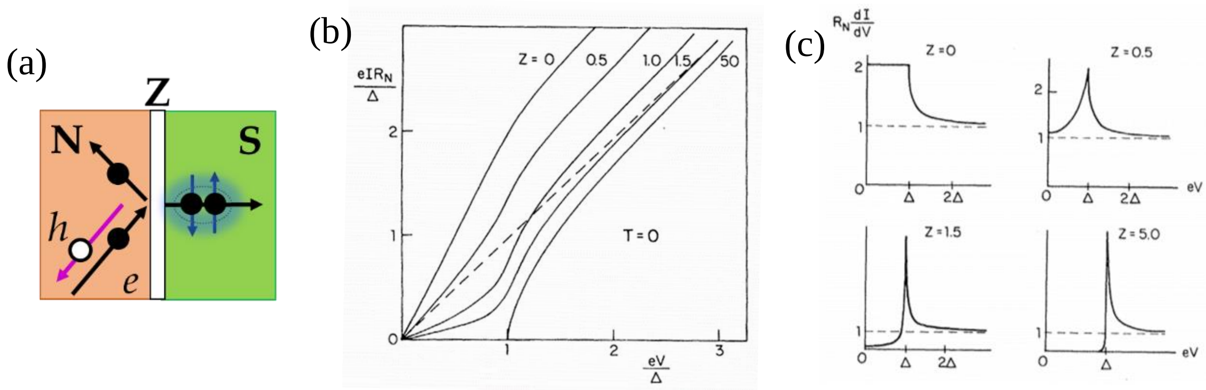

Figure 11. (a) NM-SC junction with an interfacial barrier (Z). The filled black circles are electron-like states and the white one is hole-like state. (b) The calculated normalized current in NM-SC junctions having different Z as a function of energy. (c) The corresponding differential conductance. R_N is the resistance of the junction above T_c. Reproduced with permissions from [2].

AR in a junction of a d-wave superconductor ($SC_{d\text{-wave}}$) with a metal is dependent on the orientation of the tunneling direction with crystalline axes, quantified by α in the left panel of Figure 12. The right panel of Figure 12 shows the tunneling spectra for different orientations and barrier heights (Z) are compared with the bulk density of states in normal state. Electrons and holes that tunnel into a $SC_{d\text{-wave}}$ are sensitive to the phase of the order parameter, i.e., they experience different pair potentials $\Delta(\theta_+)$ and $\Delta(\theta_-)$ respectively[3–5]. Where the angle of incidence is θ, and $\theta_+ = \theta$ $\theta_- = \pi - \theta$. The tunneling conductance in NM-I-$SC_{d\text{-wave}}$ (I – insulator) depends on both the amplitude and phase of the pair potentials. In addition, a zero-bias peak (ZBP) in conductance is expected when tunneling into to the nodes of the $SC_{d\text{-wave}}$ when a barrier is present. The nodal direction is along [110] for the $d_{x^2-y^2}$ order parameter, seen the Figure 12 (right - b, c) as α approaches $\frac{\pi}{4}$. The ZBP arises from constructive interference of the single-particle states in the nodes. Our calculated spectra functions (Figure 32) shows a mode at zero-bias, originating from the nodal fermions of the superconducting d-wave order parameter.

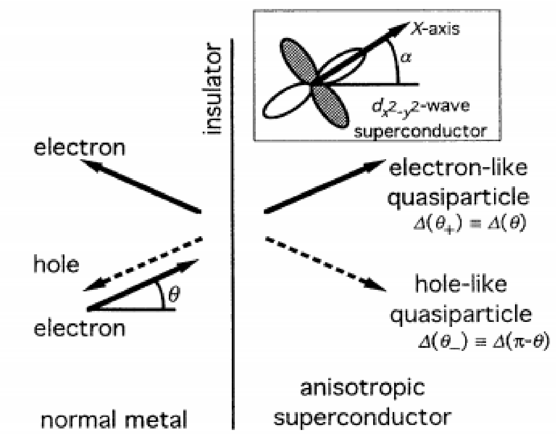

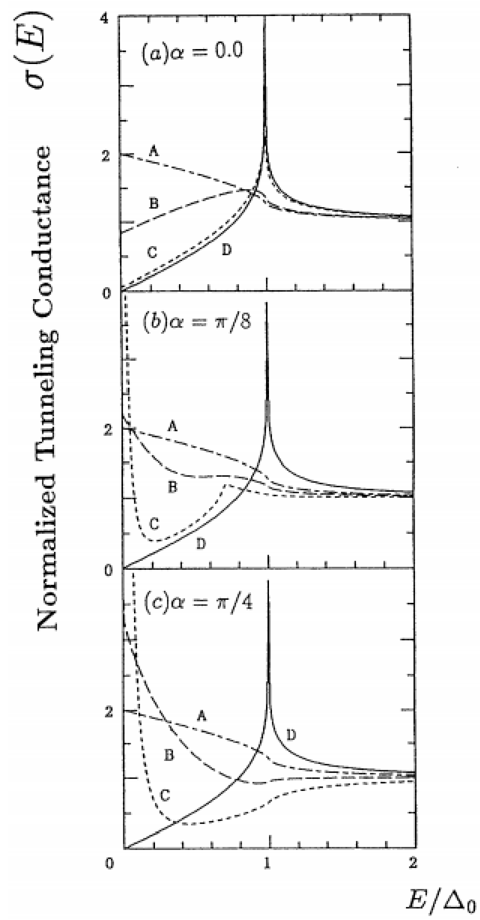

Figure 12. (left) Trajectories of quasiparticles and (right) theoretical tunneling conductance of d-wave NM-I-SC$_{\text{d-wave}}$ junction. $\alpha = 0, \frac{\pi}{8}, \frac{\pi}{4}$ in (a), (b) and (c) respectively is the angle of orientation between the lobe of the d-wave SC and the junction normal. θ is the angle of incidence of the incident electron. A, B, and C correspond to different values of Z = 0, 1, 5 respectively are normalized the bulk density of states in the normal state (D). Reproduced with permissions from [3].

Another important feature which is common to the conductance spectra from AR (s-wave or d-wave) discussed above is the difference in conductance above and below the superconducting gap (Δ_0). For near perfect AR ($Z \approx 0$), the sub-gap conductance increases due to formation of Cooper pairs. Increase in Z reduces the sub-gap conductance due to decrease in probability of AR, however Δ_0 is still inferable. When $Z \gg 1$ and conductance spectra begins to resemble the tunneling conductance of a SC-I-NM junction, a sharp drop in conductance occurs at Δ_0 corresponding to very small probability for AR. For the d-wave case, ZBP are seen with increasing Z, due to the reason explained above.

5.2 Andreev Reflection Graphene

AR in the SC-Gr junction, shown in Figure 13 (a), is unique in comparison to the SC-NM because the trajectory of particles is energy-dependent owing to the gapless helical dispersion of graphene. The SC region outlined in blue is graphene with superconducting pairing induced by the proximity effect from a conventional superconductor. Beenakker (2006) used the Dirac-BdG equations for graphene and predicted that specular Andreev reflection[6] (SAR) occurs at low doping (E_f) and excitation energy (ε). For AR to occur, we have to keep the $\varepsilon < \Delta$, which is experimentally possible by keeping the DC bias $eV < \Delta$. Consider the case when $E_f \leq \Delta$. An electron in the conduction band of graphene, which is incident on the SC, is reflected as a hole in the valence band. This inter-band reflection occurring at low energies is SAR, shown in Figure 13 (b). The transverse momentum (k_y) is conserved and longitudinal momentum (k_x) is reversed in electron-hole conversion process of SAR (Figure 13 (a)), like Klein tunneling (KT) in graphene p-n junctions. This is again due to the helical nature of carriers in graphene where the reflected hole preserves the pseudo-spin of the incoming electron.

When $E_f \geq \Delta$, the hole is reflected in the conduction band, which is called retro Andreev reflection (RAR) shown in Figure 13 (c). In RAR, the momentum vector of the reflected particle is reversed, just like AR in an SC-NM junction, shown in Figure 13 (a). Here we see how AR in graphene is sensitive to doping. Exact measurement of transition from SAR to RAR is ongoing, as we explain below.

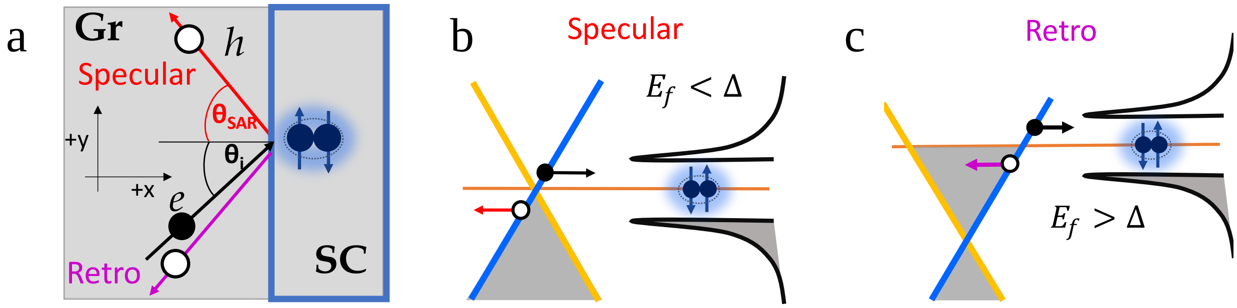

Figure 13. (a) Trajectories for SAR (red) and RAR (violet). Filled (empty) circles are electron (hole) like states. The SC region is superconducting graphene. The band diagram for the two scattering processes, SAR in (b) and RAR in (c), with graphene on the left and the SC to the right. The orange line is the Fermi-level at which the Cooper pairs in of the SC reside.

Another similarity between AR and KT is the angle dependence. The probability for Andreev reflection has a cosine dependence on the angle of incidence (θ_i) measured from the normal. Carriers that are at normal incidence ($\theta_i = 0°$) reflected with unit probability. The transmission probability decreases at oblique incidence, $0° < \theta_i < 90°$.

The experimental evidence for specular Andreev reflection junction was reported in junctions of $NbSe_2$ and bilayer graphene (BLG) on hexagonal boron nitride (h-BN) substrates by D. Efetov et al.[7]. The electron-hole puddles in the dielectric substrates, such as SiO_2, broaden the observable dispersion of graphene's electronic spectrum by $\delta\epsilon_f$~50 meV around the Dirac point. This broadening is much greater than the superconducting gap $\Delta < 2$ meV of most conventional SCs and has thwarted the observation of SAR in monolayer graphene. h-BN has proven to be a great substrate for graphene to minimize broadening and improve mobility[8]. The bottom graphene layer of BLG provides additional screening against charge puddles and keeps $\delta\epsilon_f < 1$ meV. Definite evidence for SAR in monolayer graphene is an active area of research[9,10].

The large superconducting gap ($\Delta > 20$ meV) of cuprate superconductors allows the observation of low-energy transport in SC-Gr junctions despite broadening in graphene's spectrum. Additionally, transport properties in cuprate SC-Gr junctions depend on the orientation of the *d*-wave order parameter and the presence of single-particle states within the gap that compete with AR. Below, we will review key results that have shown evidence for proximity effects in Dirac materials using high-Tc SCs.

The temperature and bias-dependent transport studies of BSCCO junctions with topological insulators (Bi_2Te_3 and Bi_2Se_3) and graphite, by P. Zareapour et al[11–13], identified different gap features in AR spectra from proximity-induced superconductivity. The transfer of superconductivity from BSCCO, with a bulk pseudogap of Δ_0, creates an induced gap of Δ_i in the material in contact and reduces gap of BSCCO at the interface to Δ_r. Zareapour et al observed the emergence of an induced gap in Bi_2Te_3 and graphite of $\Delta_i \approx 10$ meV for the zero-bias peak due to AR, i.e., low values of the Z parameter. See Figure 14 (a, b) for details. The Δ_i feature sharply appears at 40 K and continues to grow along with Δ_r and Δ_0 features below 30 K. These studies of Andreev reflection were seen in BSCCO/Bi_2Te_3 (Figure 14 (a)) and BSCCO/graphite (Figure 14 (b)) junctions using bulk materials. We expect graphene in contact with bulk BSCCO, such as in our BSCCO/Gr junctions, to acquire a comparable superconducting gap energy.

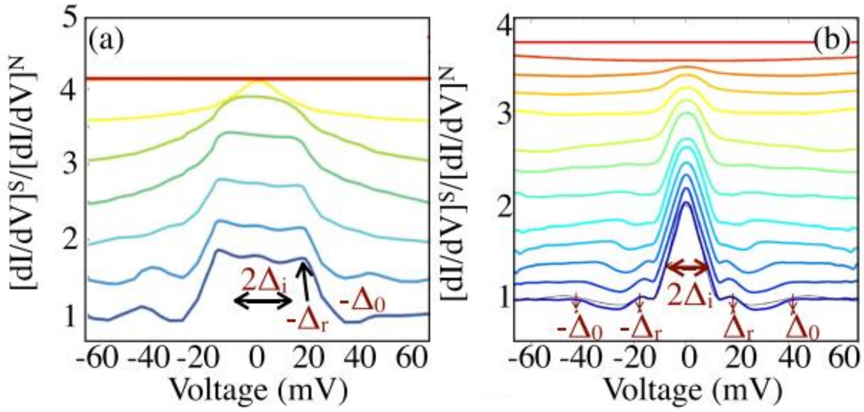

Figure 14. Normalized differential conductance for (a) BSCCO/Bi_2Te_3 (taken at 75 K, 60 K, 50 K, 40 K, 30 K and 20 K) and (b) BSCCO/Graphite junctions (70 K to 25 K every 5 K, and lastly at 11 K) with transparent interfaces. Figure adopted with from[13] (open access).

Based on the background discussion on theory and experiment above, the change in sub-gap conductance due to AR in SC-NM junctions can be useful to estimate the size of the superconducting gap. We confirm the origin of resonances from AR when $eV \leq \Delta_\mathrm{i}$ in BSCCO/Gr junctions (Figure 29 (a)) and $eV \leq 2\Delta_\mathrm{i}$ in BSCCO-Gr-BSCCO junctions (Figure 38 (a)), where Δ_i is the superconducting gap in graphene in contact with BSCCO. The resonances in our devices are reduced by an order of magnitude when DC bias is above $\Delta_\mathrm{i} > 15$ mV. This is comparable to the induced gap found in AR study of BSCCO/graphite junction shown in Figure 14 (b) and tunneling bias spectra on CVD graphene on single-unit cell BSCCO[14].

5.3 Gating a Barrier at the SC-Gr Junction

The work by S. Bhattacharjee and K. Sengupta (2006)[15] considered a graphene NM-I-SC junction with a conventional SC. The potential barrier height (V_0) in the I region* of length, d, is

* The barrier region “I” stands for doped graphene and not an insulator. It is the same as Gr’ in the discussion of our experimental results.

gate-tunable, as depicted in Figure 15 (a). Bulk metals which have large carrier concentrations can create barriers in the form of *p-n* junctions when in contact with graphene ($n{\sim}10^{12}$ cm^{-2}) by charge transfer. As we have discussed before in Chapter-2, Klein tunneling occurs at the *p-n* interface and is evidenced by reduced conductance. Similarly bulk superconductors can also transfer charge and create *p-n* junctions when brought in contact with graphene. A *p-n* junction formed at the SC/Gr interface is similar to the structure considered by Bhattacharjee et al and acts like the I region. The single BSCCO/graphene devices discussed in Chapter-7 are based on this concept.

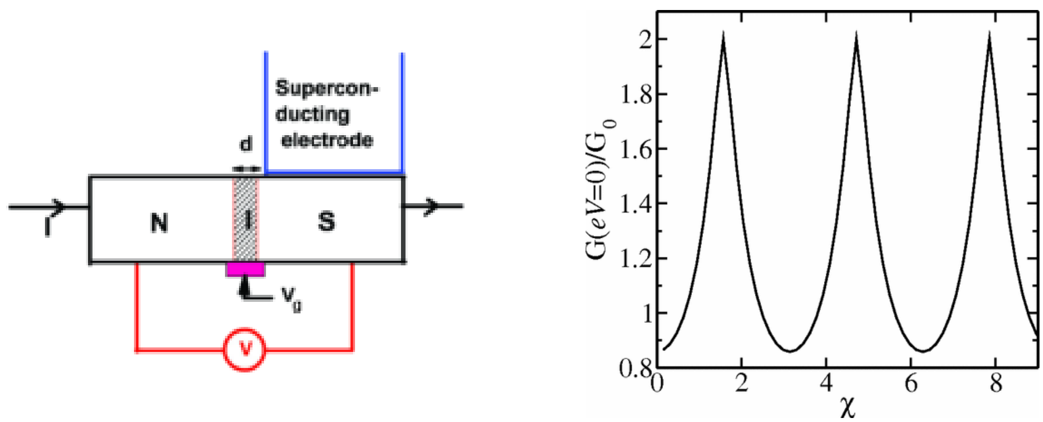

Figure 15. (left) Schematic of N-I-S device considered in [15], where the barrier is a gate tunable region of graphene. (right) The normalized tunneling conductance with respect to a theoretical gating parameter χ in units of π. Reproduced from [15].

Gating the I region of the NM-I-SC was predicted to result in an oscillatory behavior for the junction conductance when the barrier height was varied by a theoretical gating parameter $\chi = \frac{V_0 d}{\hbar v_f}$, shown in Figure 15 (right). The oscillations have a period of π with maxima at $\chi = \left(n + \frac{1}{2}\right)\pi$, where n is an integer. This device structure could be fabricated using e-beam lithography to make a small gate (10-20 nm) at the I region. Alternatively, one can estimate the length of the I region due to its relationship with the resonance period. Similarly, we estimate the length of the I region (called Gr' in Chapter-7) formed due to charge transfer in single BSCCO/graphene junctions is ~60 nm.

Note that the theory discussed above came before the theory on Fabry-Perot resonances from Klein-Tunneling in graphene *p*-*n* junctions in 2008[16]. In Chapter-7 we explain our results on resonances in BSCCO/Gr junctions can be treated as Fabry-Perot resonances occurring due to two mechanisms - Andreev reflection and Klein tunneling.

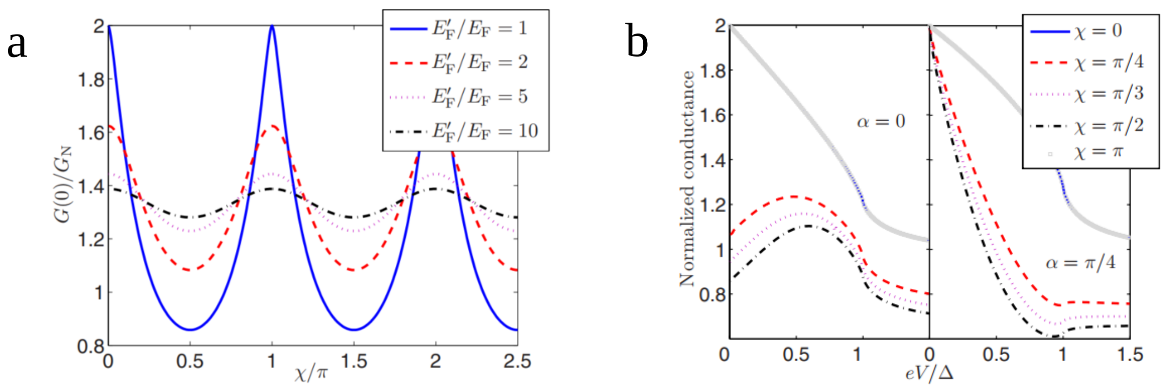

Figure 16. (a) Normalized conductance as a function of the gating parameter χ taken at different E_f'/E_f regions for s-wave SC-I-Gr. (b) Normalized conductance of a $SC_{d\text{-wave}}$-I-Gr junction with the angle α between the junction normal and lobe at 0° (left) and at 45° (right) taken at different values of the gating parameter in units of π. Reproduced with permissions from [17].

The advancement to this prediction was made by J. Linder and A. Sudbø (2008), who analytically examined the tunneling conductance of both *s*-wave and *d*-wave SC-I-Gr[17] junctions. The oscillations are expected to persist for different barrier heights ($E_f{}'$) in the I region, as shown in Figure 16 (a). Figure 16 (b) shows the conductance for the $SC_{d\text{-wave}}$-I-Gr junction for different values of the gating parameter, where α is the angle the *d*-wave lobe makes with the junction. The zero-bias peak when $\alpha = \frac{\pi}{4}$ corroborates with the results in $SC_{\text{d-wave}}$-NM junctions, which is a consequence of constructive interference of nodal single particle states[4,5]. The period of oscillations in the $SC_{d\text{-wave}}$-I-Gr case is also π. The resonant condition calculated in this work was $\chi = n\pi$, without the phase shift of $\frac{\pi}{2}$ derived in [15], for either superconducting pairing. The oscillation amplitude in the *d*-wave case is lower than the *s*-wave case, due to competing transport from single-particles within the gap that do not participate in Andreev reflection. In the experiment, this is evidenced by the reduction in oscillation amplitude with increasing bias which increases single-particle transport and is shown in Chapter-7.

Next, we discuss the experimental work by D. Perconte et al. (2018) on Gr/YBCO junctions[18]. The high-temperature *d*-wave SC, YBCO, was grown on a thick strontium titanate (STO, with relative permittivity $\epsilon_r = 1000$) substrate. A region of it was capped with 4 nm of Au to protect its superconducting properties. This superconducting YBCO region is marked "S" in Figure 17 (a). The uncapped YBCO was intentionally degraded to be insulating (the "Ins" region) with a surface roughness of 4 nm. CVD graphene was transferred to this structure to complete the device. By the proximity effect, the graphene on the Au/YBCO region becomes superconducting and is labeled "S" and the normal graphene region "N" is on Ins, also shown in Figure 17 (a). There is an intermediate N' region of doped graphene which forms naturally because of dielectric screening in the junction and acts as a tunable potential barrier. They performed three-terminal measurements of the S-N'-N junction as a function of the excitation bias (V), the gate voltage (V_G), and temperature. They observed a zero-bias peak of width ± 10 mV in the junction conductance, which can be seen in Figure 17 (b), and starts to appear below 30 K, in agreement with the superconducting gap of YBCO.

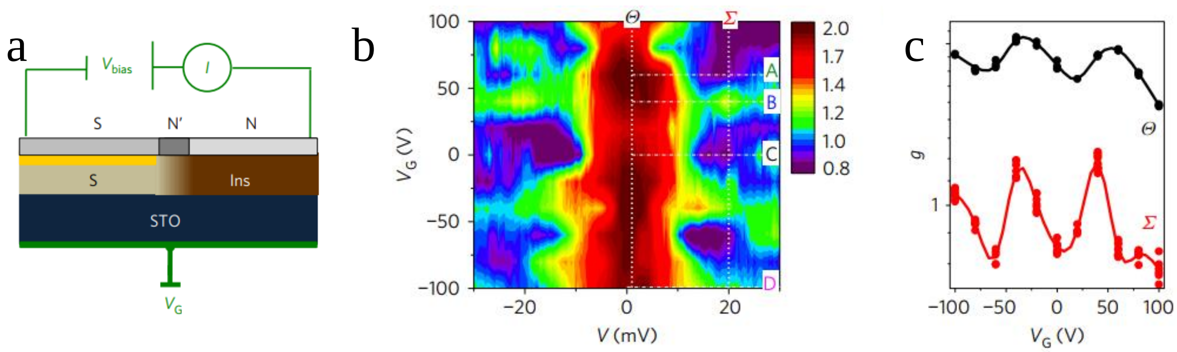

Figure 17. (a) A schematic of Gr/YBCO device on STO substrate. The graphene spans over superconducting (S) and insulating (Ins) regions of YBCO. The superconducting region of graphene is S, barrier normal region formed screening is N', and the rest of normal region is N. (b) Colormap of differential conductance as a function of excitation bias and gating. (c) Slices along gate voltage at zero bias and near the superconducting gap edge of YBCO showing a period of 75 V, which is 35 meV in Fermi-energy. Figure reproduced with permissions from [18].

The zero-bias peak is a sign of Andreev reflection through a highly-transparent interface between graphene and Au/YBCO. Conductance oscillations were observed along gate voltage (V_G) shown in the vertical axis of Figure 17 (b). Slices along V_G at 0 V (Θ) and 20 meV (Σ) are shown in Figure 17 (c). The reduced oscillation amplitude from single particle transport at high bias is visible in Figure 17 (c). The oscillations have a period of 75 V, which corresponds to ~33 meV using the proportionality factor $\frac{\delta\chi}{\delta E_F} \sim \frac{3\pi}{100}$ meV^{-1} based on the capacitance of the substrate. These conductance oscillations are a result of carrier interference in the N' region. However, due to experimental constraints, their devices operated in the highly doped p^+-p regime and did not reach the p-n regime required to observe Klein tunneling. In our work on BSCCO/Gr junctions we are able to gate the devices from p^+-p to p-n, supported by conductance asymmetry and observation of two minimum conductivity points at high bias. Perconte et al used the oscillation period to estimate the length of the N' region, $w = \frac{\delta\chi}{\delta E_F}\hbar v_f \approx 60$ nm. Their model and analysis are based on the work by J. Linder (2008)[17] discussed earlier.

This chapter concludes the discussion of the background information required to understand our experimental results. We have shown the similarities between Klein tunneling (Chapter-2) and Andreev reflection, owing to the helical nature of carriers in graphene. The recent results on Gr/YBCO junctions showed resonances from the presence of a potential barrier at the interface, supported by pre-existing analytical theories. The reported superconducting gap induced in Dirac materials from proximity to BSCCO supports our results on bias dependence of the resonances. As we explain in Chapter-7, our work is distinguished by the hallmark feature of Klein tunneling - conductance asymmetry as we change the doping from *p*-*p* to *p*-*n*, which occurs together with Andreev reflection as evidenced by the suppression of oscillations above the induced superconducting gap.

References

1. Lee, G.-H. & Lee, H.-J. Proximity coupling in superconductor-graphene heterostructures. *Reports on Progress in Physics* **81**, 056502 (2018).
2. Blonder, G. E., Tinkham, M. & Klapwijk, T. M. Transition from metallic to tunneling regimes in superconducting microconstrictions: Excess current, charge imbalance, and supercurrent conversion. *Phys Rev B* **25**, 4515–4532 (1982).
3. Tanaka, Y. & Kashiwaya, S. Theory of Tunneling Spectroscopy of *d*-Wave Superconductors. *Phys Rev Lett* **74**, 3451–3454 (1995).
4. Hu, C. R. Origin of the zero-bias conductance peaks observed ubiquitously in high superconductors. *Phys Rev B Condens Matter Mater Phys* **57**, 1266–1276 (1998).
5. Kashiwaya, S., Tanaka, Y., Koyanagi, M., Takashima, H. & Kajimura, K. Origin of zero-bias conductance peaks in high-T_c superconductors. *Phys Rev B* **51**, 1350–1353 (1995).
6. Beenakker, C. W. J. Specular Andreev Reflection in Graphene. *Phys Rev Lett* **97**, 067007 (2006).
7. Efetov, D. K. *et al.* Specular interband Andreev reflections at van der Waals interfaces between graphene and $NbSe_2$. *Nat Phys* **12**, 328–332 (2016).
8. Dean, C. R. *et al.* Boron nitride substrates for high-quality graphene electronics. *Nat Nanotechnol* **5**, 722–726 (2010).
9. Moriya, R., Yabuki, N. & Machida, T. Superconducting proximity effect in a $NbSe_2$-graphene van der Waals junction. *Phys Rev B* **101**, 054503 (2020).

10. Sahu, M. R., Raychaudhuri, P. & Das, A. Andreev reflection near the Dirac point at the graphene-$NbSe_2$ junction. *Phys Rev B* **94**, 235451 (2016).

11. Zareapour, P. *et al.* Modeling tunneling for the unconventional superconducting proximity effect. *Supercond Sci Technol* **29**, (2016).

12. Zareapour, P. Proximity Effect and Tunneling Spectroscopy of High-Temperature Superconductor-Semiconductor Hybrid Structures. vol. 13 (2015).

13. Zareapour, P. *et al.* Andreev reflection without Fermi surface alignment in high-T_c van der Waals heterostructures. *New J Phys* **19**, 043026 (2017).

14. Wu, Y. *et al.* The transport properties in graphene/single-unit-cell cuprates van der Waals heterostructure. *Supercond Sci Technol* **32**, (2019).

15. Bhattacharjee, S. & Sengupta, K. Tunneling conductance of graphene NIS junctions. *Phys Rev Lett* **97**, 1–4 (2006).

16. Shytov, A. V., Rudner, M. S. & Levitov, L. S. Klein Backscattering and Fabry-Pérot Interference in Graphene Heterojunctions. *Phys Rev Lett* **101**, 156804 (2008).

17. Linder, J. & Sudbø, A. Tunneling conductance in *s*- and *d*-wave superconductor-graphene junctions: Extended Blonder-Tinkham-Klapwijk formalism. *Phys Rev B Condens Matter Mater Phys* **77**, 1–14 (2008).

18. Perconte, D. *et al.* Tunable Klein-like tunnelling of high-temperature superconducting pairs into graphene. *Nat Phys* **14**, 25–29 (2018).

6. Sample Fabrication

The fabrication of devices using heterostructures of 2D materials for various experiments has deviated from conventional methods that often rely on deposition or growth to obtain heterogeneous layers of materials. The scotch-tape method, first used by K. Novoselov to isolate monolayer graphene, is still used today to exfoliate many 2D materials. The exfoliated layers are then characterized by optical microscopy, atomic force microscopy (AFM) and Raman spectroscopy to identify isolated “flakes” which are of desired thickness, uniformity, and free of contamination. This is followed by a dry stamping technique, called “pick-and-place”, to make heterostructures to combine different 2D materials. The finished heterostructure, often referred to as a “stack”, can then move to lithographic steps for device fabrication or is ready for desired experiments. This chapter presents the details of such methods which were utilized in the fabrication of various BSCCO/Gr and BSCCO-Gr-BSCCO devices.

6.1 Introduction to Pick-and-Place

The pick-and-place technique for 2D materials was initially demonstrated by using heterostructures of hexagonal boron nitride (h-BN) substrates to improve the carrier mobility in graphene [4–6]. The phonons of high-quality h-BN do not couple to not couple to carriers in graphene. This is the reason h-BN has proven to be a better substrate for graphene` compared to SiO_2. Since then, the technique has evolved rapidly, leading to discoveries and applications from combining dissimilar 2D materials[7]. Another domain of research using 2D materials explores physics that emerges when the angle between monolayer 2D materials is precisely controlled to break natural stacking symmetry[8–12]. This field has earned the names “twistronics” or “Moire magic” is also a byproduct of this technique.

The primary advantage of the pick-and-place technique to create our 2D material heterostructures is atomically clean interfaces. Previous work in Prof. Lee’s group on tunable Schottky barrier in graphene/WSe_2 junctions[13] due to the absence of fermi-level pinning is a great example of new device physics which is enabled by using pick-and-place to achieve clean interfaces. This motivated us to invest more time and resources to develop the technique to fabricate heterostructures using other 2D materials, such as BSCCO, in a relatively inert environment.

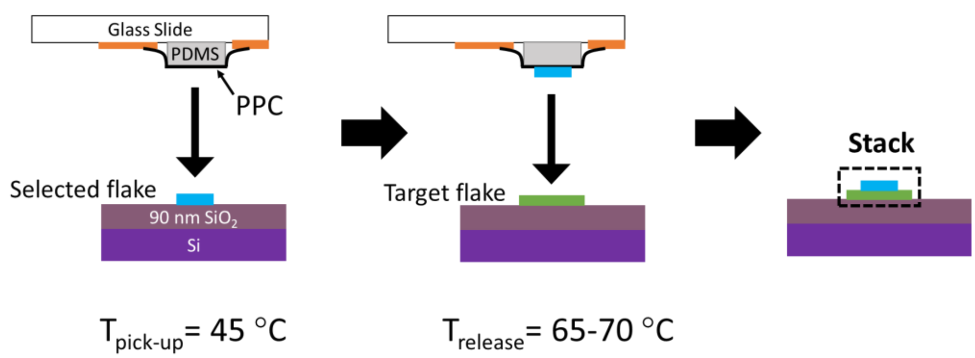

Figure 18. A simplified schematic of assembling a stack using the pick-and-place technique. (left) Start with a PPC/PDMS/Glass Slide stamp. Align it over a selected flake for pick up. (middle) After picking up the selected flake with the stamp align it over the target flake and release it. (right) The completed heterostructure is informally called a stack.

Most commonly, the “stamp” is a clean glass slide on which we place a slab of poly-dimethyl siloxane (PDMS) about 1-2 mm thick. The PDMS is rinsed in IPA and treated in O_2 plasma. Then a film of polypropylene carbonate (PPC) is draped over the PDMS and held in place using a double-sided tape, see Figure 18. The sample with the selected flake (blue) is set to 45 °C (below the glass transition temperature, T_g, of PPC) and the stamp is lowered until it contacts the substrate, Figure 18 (left), and PPC covers the flake. If the flake has bonded to the stamp by Van der Waals forces, it will be picked up from the substrate. The temperature of the target substrate (green) is set to 65 °C and the stamp/flake is carefully lowered onto the target flake. Fine adjustments to the alignment are made as needed, Figure 18 (middle). After contact is made, the stamp is raised to release the selected flake onto the target flake. PPC's adhesion to the flake is reduced above T_g, which allows the first flake to be released onto the second one resulting in the stack shown in Figure 18 (right).

The above description is a simple stack of two layers (could be the same or different materials) of 2D materials. Far more complex stacks have been fabricated by sequentially picking up additional layers either for encapsulation, gating, proximity effects, and heterojunctions. The pick-and-place process is usually not ideal because the success of each step depends on many factors that are not easy to quantify. For example, we have been able to pick up bulk crystals of h-BN, BSCCO, and graphite using the PPC-based stamps. However, it is more challenging (or even impossible) to pick up monolayer graphene directly using the PPC stamp. Also, plasma-treated substrates make it harder to pick up flakes and can sometimes even delaminate the PPC from the stamp. Such factors show that the pick-and-place technique needs to be developed for each material layer in a stack accounting for thickness, how they are exfoliated, and the stacking order. Mastery over these techniques is built on tentation, as it is for most crafts. Lastly, a feedback loop between experimental results and all aspects of fabrication (how the individual 2D materials are handled, how the stacks are assembled, lithography, etc.,) is necessary to truly gauge the scientific value of the stacks to go beyond visual appeal.

6.2 Substrates

The common substrates to exfoliate 2D materials are silicon wafers with 90 or 300 nm of silicon dioxide (SiO_2). The optical interference of 2D materials on SiO_2/Si produce a good correspondence between color (and/or contrast) and thickness when viewed under an optical microscope - usually the first estimate for the thickness of the flakes[14,15]. The charge puddles and surface roughness of SiO_2 are the two main problems that affect the mobility of graphene. We take advantage of CNSE's 300 mm fabrication facility to procure thermally grown SiO_2 on doped Si wafers, which have a low surface roughness (<1 nm). The high-doped Si wafer acts as a global gate for our devices. We initially used the standard Si wafers and found that the gate was freezing out below 50 K for $V_g < 0$ V due to insufficient doping. To address this, we requested p-type ion implantation on the Si-surface before growing the SiO_2 by thermal oxidation. These highly-surface-doped wafers have worked well down to liquid helium temperatures.

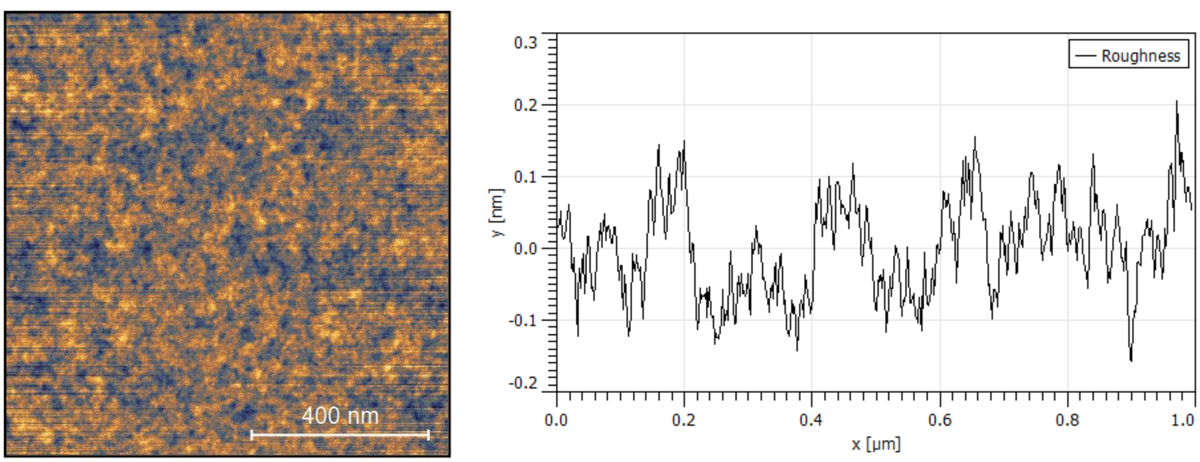

Figure 19. (left) AFM scan of 90 nm SiO_2 wafer. (right) An line scan averaged over 100 pixels which show a surface roughness of $\pm$ 0.1 nm of our thermal oxide wafers.

The SiO_2/Si wafers require minor cleaning steps before exfoliation because they come clean out of the fab. Figure 19 left panel shows the 2D AFM image of the SiO_2 surface and the averaged line scan in the right panel gives us confidence that the surface roughness is very low ~1 Å. We first dice the 300 mm wafer into smaller 2×2 cm^2 die. These are then rinsed in semiconductor-grade isopropyl alcohol (IPA) and dried with nitrogen. Next, we either plasma treat or dehydration bake the die, depending on the 2D material that will be exfoliated (not required for graphene), the desired thickness, and if the target flakes will be picked up for heterostructure assembly.

An array of alignment marks is patterned on the 90 nm SiO_2/S die by using e-beam lithography and depositing of Ti (3nm) + Au (20 nm) prior to exfoliation to help record the locations of graphene flakes in optical images (which we refer to as "mapping") and for inter-layer alignment during e-beam lithography. The metal deposited for alignment marks needs to be >20 nm thick for it to have good contrast under 300 nm of PMMA-A4, the primary resist used during e-beam lithography. The metal stack also needs to be robust against any aggressive steps such as high-temperature annealing. Graphene can be exfoliated on the marked SiO_2/Si die after they are treated in an oxygen plasma to ash away any resist residue.

6.3 Graphene Preparation

Different sources of high-purity graphite were examined by a previous student in Prof. Lee's research group. Dr. Sam LaGasse found that Naturagraphit Systems (NGS) Graphenium natural graphite yielded high-electron mobility samples (Sam's thesis: SUNY at Albany ProQuest Dissertations Publishing (2019). 22592148). NGS Graphenium has been the primary source crystal for all the graphene in devices for this work.

The exfoliation of graphene starts by preparing two sets of finger-long adhesive tapes from a standard roll of 3M Scotch Tape®. The first set is used as the “source” tape, used to carry a bulk graphite crystal which is gently tessellated for maximum coverage. Care should be taken to not bend the tapes or press them too hard while tessellating as this tends to break down the graphite crystals and lead to smaller graphene flakes on SiO_2 or even reduce yield to nil. The source tapes are copied onto a second set of “transfer” tapes which are used to exfoliate graphene on the SiO_2/Si die. See panels in Figure 20 (a) which shows the entire process of preparing these tapes. The die, discussed earlier for graphene exfoliation, is pretreated with a 50 W plasma of Ar (50 mTorr) + O_2 (100 mTorr) for 90 seconds to reduce hydrocarbons and increase Van der Waals forces. Together they increase the yield of exfoliated monolayer graphene. The transfer tape is brought into contact with the SiO_2/Si die immediately after they are plasma treated. The back of a tweezer is used to gently press the back of the tape which removes air bubbles and improves the contact area between the graphite on the tape with SiO_2. Next, we anneal the tape/wafer on a hotplate at 100 °C for 1 minute while continuing to press the back of the tape using a lint-free cloth. If the tape is peeled when the tape/wafer is still hot, there will be more adhesive residue and the yield of monolayer graphene will suffer. Once the tape/wafer is cooled to room temperature by blowing compressed nitrogen, we proceed to carefully peel the tape away from the wafer in one continuous motion. Figure 20 (b) gives an idea of how this is executed and how the resulting die looks visually. We avoid re-contacting the transfer tape to the wafer while peeling because this may contaminate the exfoliated flakes or pick them off the wafer. Finally, we use an optical microscope to collect images of the monolayer graphene. An example is shown in Figure 20 (c).

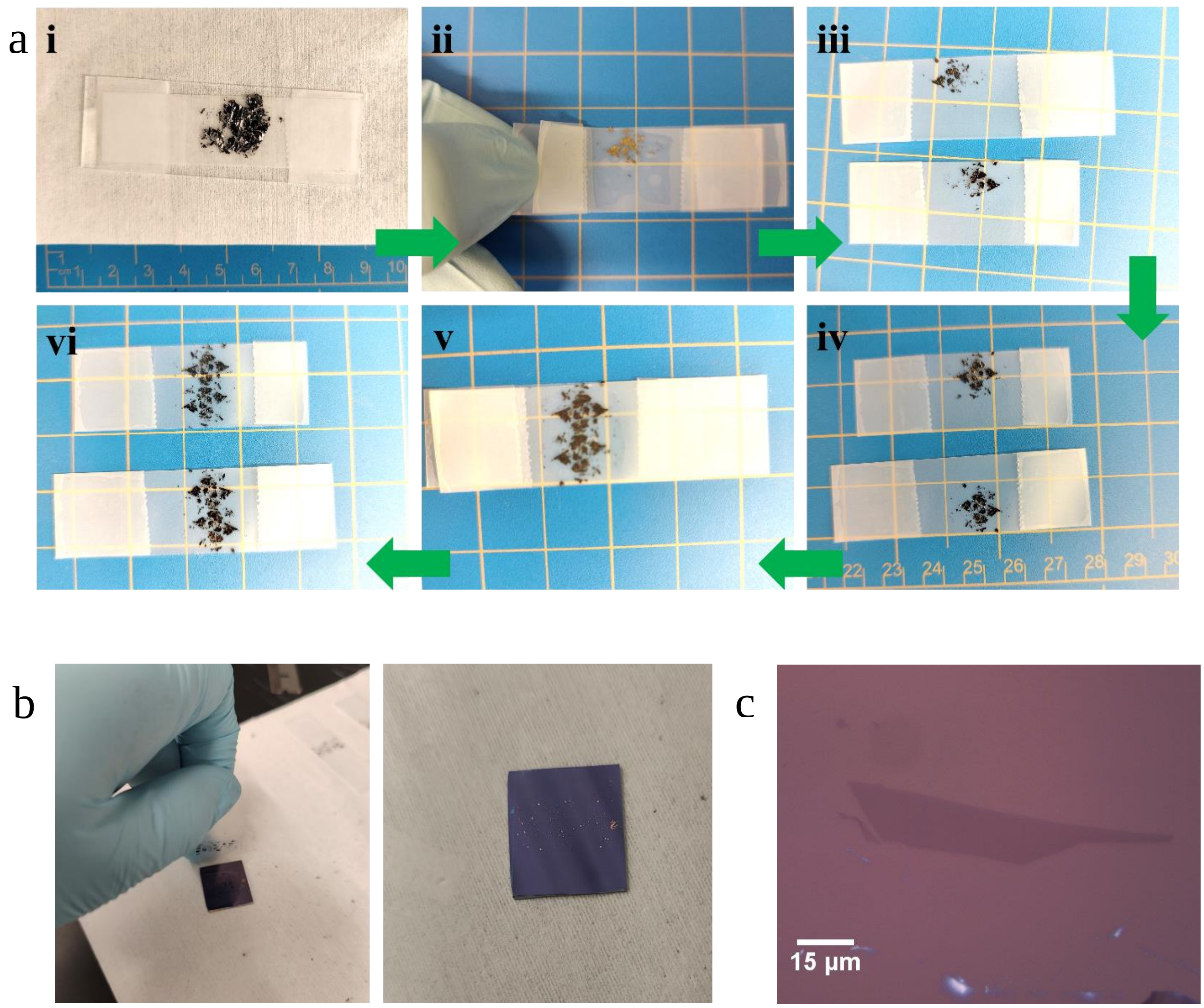

Figure 20. (a) Sequence of images for graphene exfoliation process. We start from a bulk crystal on a tape, which anchored to a glass slide. A transfer tape is used to peel off a small piece of bulk graphite. The scale of the background mat in (i) is in units of centimeters. Panels (ii-vi) show how we tessellate the graphite between two transfer tapes to maximize coverage to match the size of the wafer (about 2 x 2 cm^2). Each square in panels (ii-vi) is ½ X ½ inch. (b) First panel shows the transfer tape being peeled off the 90 nm SiO_2 wafer. Large bulk graphite flakes exfoliated on the wafer are noticeable to the naked eye. Seeing more of these is a good indicator of the chance of finding graphene under a microscope. (c) Optical micrograph of exfoliated graphene on 90 nm SiO_2/Si wafer.

Raman spectroscopy is a powerful technique to determine the number of layers and quality of graphene. The ratio of intensities of the 2D (also called G' at 2700 cm-1) peak with respect to the G (at ~ 1582 cm-1), $\frac{I_{2D}}{I_G}$ and FWHM are quick ways to verify the presence of monolayer graphene [16]. These quantities are sensitive to various extrinsic effects such as doping by the substrate, surface roughness, impurities, and defects. We have observed ratios of $\frac{I_{2D}}{I_G}$ for graphene on our plasma treated SiO2/Si substrates in the range between 1.2 to 1.4 (Figure 21 (a)). Lastly, the presence of a D-peak at 1350 cm-1 in is an indication of degradation. The D-peak is not observed in our graphene at any stage – from exfoliation to device completion.

After we collect the Raman spectra, the SiO_2/Si wafers with monolayer graphene are annealed in a quartz tube furnace (2" diameter) in a gas mixture of Ar (50 sccm) + H_2 (100 sccm) at 300 °C for 3 hours to remove hydrocarbons such as tape adhesive residue. The removal of tape residue is crucial to avoid lift-off issues. After annealing, we go back to each of the mapped locations to check if the graphene has deformed and only select those that remain unchanged to be used in devices. Figure 21 (b) show an example of a topographic image on an exfoliated graphene (yellow) after Ar/H_2 anneal, acquired using a Bruker Dimension Icon AFM. These scans have helped to assess the cleanliness of graphene before the pick-and-place steps.

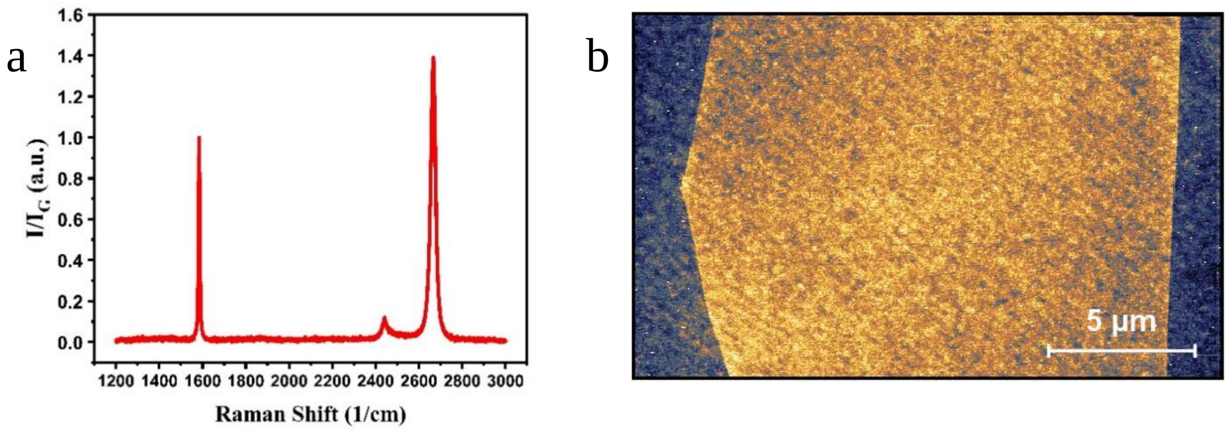

Figure 21. (a) Raman spectrum of monolayer graphene on the highly doped 90 nm SiO_2/Si substrate collected using 532 nm laser. (b) Height image from AFM scan so that the gold color shows graphene after Ar/H_2 annealing. Because the step height in graphene is 0.3 nm, distortions from interference of the laser reflected from the SiO2 substrate can appear in the AFM image, like the slanted fringe background in this image.

6.4 Glovebox with Pick-and-Place

After graphene is ready to be used in devices, the next stage of fabrication requires exfoliation of BSCCO to assemble the BSCCO-graphene heterostructure. Unlike graphene, BSCCO requires an inert glovebox to minimize the degradation from exposure to water vapor.

We commissioned an N_2 glovebox from Inert Corporation to work with sensitive layered materials. At this juncture, the lock-down from the COVID-19 pandemic in March 2020 slowed our progress. Fortunately, by August 2020 we began testing an existing hand-driven pick-and-place station to assemble encapsulated graphene and BSCCO-Gr heterostructures. Our productivity was thwarted by reduced dexterity from the butyl gloves and poor ergonomics which caused great physical strain to the user. Forced to innovate by necessity, we designed a motorized pick-and-place station which can carry multiple samples and allow for precise control during stacking. The schematic of the pick-and-place station is shown in Figure 22 (a) and the image of the actual station is shown in Figure 22 (b). They show four sample holders on the translational stages, a tube microscope, and the glass-slide stamp on a separate motor. The details of the design and operation are discussed below.

The temperatures of the sample holders (labelled 1 to 4 in green in Figure 22 (a)) can be individually set and monitored by the multi-channel temperature controller (labelled "4-Ch TC", red in Figure 22 (a)). The sample holders have a 1/8-inch vacuum connection to anchor down samples during stacking. The sample holders are all mounted on a thermally insulating "sample block" to prevent heat transfer between them. Two linear stages (X, Y in grey) that are orthogonal to each other provide long-range motion to navigate between samples and permit coarse alignment. The sample block is finally mounted on the rotational stage (R in orange in Figure 22 (a)), which are together on the of X, Y linear stages. The rotation stage is very helpful in making fine inter-layer alignments, $<15°$ with $<0.1°$ degree resolution, while stacking. The corresponding components can also be found in the image of the actual station, see Figure 22 (b). There is a 2 X 3 cm die on holder-1 to provide a sense of the scale of the different components. All stages (X, Y and R) and the temperatures for the four sample locations can be controlled from a computer located outside the glovebox.

The wires to the heater cartridges and thermocouples are encased in a flexible hose to reduce clutter and avoid entanglement. There are two valves in the vacuum line to the sample holders. The primary quarter-turn valve is positioned close to the user (not visible in Figure 22 (b)), towards the window side of the glovebox, which is closed whenever the station is not in use. The secondary quarter-turn ball valve is always open and connects to the glovebox's feedthrough port via a tee joint, partially visible in Figure 22 (b). The other end of the tee is provisional for other vacuum needs and remains closed.

The other aspect of the stacking process is manipulating the stamp which is used to pick-up a desired flake of 2D material and set it down at a new location to release or sequentially pick-up the next 2D layer. This process can be repeated several times while varying the materials being stacked to control the thickness and inter-layer orientation. We opted for a micromanipulator driven by piezo motors in three axes (x, y or in-plane and z or up/down) which provides a 30 nm resolution over +/- 2.5 cm range. The pitch and roll of the stamp can be separately adjusted manually by micrometers to control the contact angle of the stamp. Once the glass slide of the stamp is secured by shoulder-screw on the clamp and brought into the field of view under the microscope, the stacking process can continue via graphic user programs to control the stamp in three axes. Stamp micromanipulators operated by hand have several disadvantages such as poor resolution and inaccuracy in alignment. But the worst one is the transfer of vibrations and jerks from the human hand to the stamp when it is in the middle of pick-up or set down. These disruptions can cause sudden unpredictable damage to the precious heterostructures on which many intensive hours were invested. We circumvent these issues by using the motorized stamp micromanipulator which is shown in Figure 22 (a) and (b).

Lastly, we modified the tube microscope by attaching a rotating turret capable of selecting between three long-working-distance infinity-corrected objectives (10X, 20X and 50X, *blank*) to offer multiple ranges of magnification while leaving space for a stamp (glass slide + PDMS of ~ 3 mm) to be in the optical path. It is installed on a heavy-duty adjustable boom stand which allows for extension/retraction and swiveling, as indicated in Figure 22 (a). The image is captured by a CCD camera and fed to a computer via USB-2.0 feedthrough on the glovebox. The working distance can be adjusted by a knob. Fine settings to the image focus can be made by a dial on the microscope. The microscope also has a 0.02X to 7X focus module which gives dynamic control over the field of view. The magnification and focus modules with the objective turret are visible in Figure 22 (b).

The sample stages, stamp micromanipulator, and microscope are bolted into a single 1” thick aluminum plate to reduce acoustic vibrations. The floor of the glovebox is a stainless-steel plate which is not supported by a cross brace, even from the outside. Changes in pressure of the box makes the floor behave like a diaphragm. When the three components were separately placed on the glovebox’s floor, the vibrations were very noticeable and made it difficult to concentrate. The base plate was incorporated to mitigate the vibrations by coupling all components to one solid base. One other part that is most susceptible to vibrations is the tube microscope with the heavy nosepiece which sometimes oscillates. However, this was not detrimental to our operation.

The cumulative result of the mechanics and automation is a system that has enabled control and **repeatability to our stacking process and increased our productivity by a factor of four.** The system can easily locate target flakes, record image and positions, and return to them - all while ergonomically friendly.

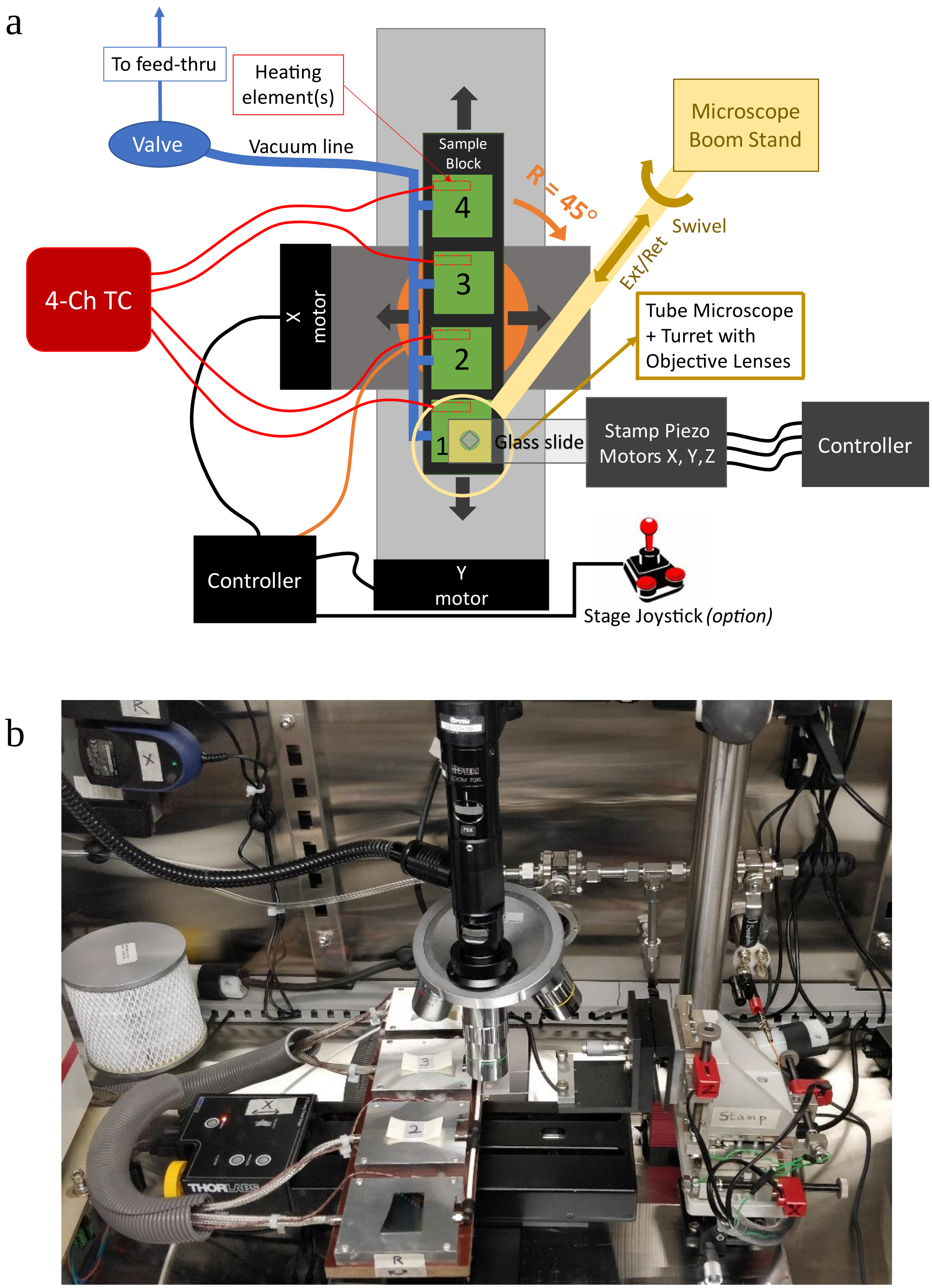

Figure 22. (a) Schematic for the motorized multi-sample pick-and-place station. (b) Image of the actual apparatus in the glovebox.

6.5 Assembling BSCCO/Graphene Heterostructures

The exfoliation of BSCCO is performed in the glovebox to minimize exposure to water vapor and oxygen. The double-sided Semiconductor Equipment Corp. Heat Release 3198M tape has a heat release side and pressure release side. We prefer to use the stickier heat-release side to make the BSCCO source tapes and the pressure-release side for the BSCCO transfer tapes. Note that the heat-release property is not used in preparing the source tapes. The same level of care in preparing the tapes for graphite also applies here. The 90 nm SiO_2 die of size 2×2 cm^2 are cleaned with IPA and brought into the glovebox. They are annealed on a hotplate at 100 °C for 1 minute to desorb surface water. They are then allowed to cool down to room temperature before exfoliating BSCCO using the transfer tapes. We record positions (x, y) and collect images of target BSCCO flakes which are 20-60 nm thick using stages 2 and 3 of the pick-and-place station at room temperature. The BSCCO flakes are selected based on:

1. Cleanliness – No indication of tape residue on the flake or trapped bubbles,
2. Thickness – Prefer to work with flakes >20 nm because they are easier to pick up.
3. Uniformity – No step edges, no ripples, no pointy edges that can be embed into the stamp and make it difficult to release.
4. Shape/Size – We need BSCCO flakes that are at least 30 μm along one side to be compatible with the 4-terminal structures on our photolithography mask.

We try to minimize the time taken from exfoliation to stack completion. The die with annealed graphene and the PPC stamps are loaded in the glovebox with the blank die intended for BSCCO. The wafers containing graphene are placed on location-1 of the stage and held at 40 °C. After the mapping of BSCCO flakes is complete, the stamp is inserted into the manipulator and stacking can begin immediately. We compare the optical images of different graphene flakes and the mapped BSCCO before making the stack. There may be big graphite flakes in the vicinity of the target graphene that may impede the placement of BSCCO or position of contacts during lithography. The BSCCO/Gr stacks for the results discussed in Chapter-7 are assembled according to the steps discussed in Section 6.1 by placing a clean BSCCO (30-40 nm) flake onto a pristine monolayer graphene.

The fabrication of BSCCO-Gr-BSCCO stacks for the results discussed in Chapter-8 has required additional ingenuity by using the piezo-driven stamp to mechanically crack a BSCCO flake (~40 nm thick) while setting it on graphene. A schematic and the corresponding microscope images of the process are shown in Figure 23 (a) and (b), respectively. We use the term “contact front” to refer to the edge of the contact area between the PPC stamp and sample. A downward motion of the stamp on or towards the sample causes the contact front to move inward. Once we have picked up the BSCCO using a PPC stamp and aligned over a graphene (all in the glovebox) using a high-resolution reference image, we set the temperature of the graphene sample to 45 °C. The contact front moves inward rapidly if the sample is >55 °C, making it difficult for a human user to respond and stop. Also, the cracking process is not effective when PPC >55 °C because it begins to lose rigidity. The next step is to lower the stamp/BSCCO into contact with the graphene sample and stop the contact front mid-way on the graphene as shown in the left panel of Figure 23 (a). We call the movable interface of the stamp with the substrate as the “contact front”. We then carefully make incremental steps on the stamp motor to first move 5-10 μm perpendicular to from the contact front and then move 5-10 μm along the contact front. This shearing force on the stamp causes the BSCCO flake to crack into two. These are labelled BSCCO-1 and BSCCO-2 in the second image from the left of the bottom panel in Figure 23 (b).

The cracks tend to propagate naturally along the contact front of the stamp. As an example, we show an optically visible crack with a spacing of ~5 μm, i.e., the junction length between BSCCO-1 and BSCCO-2. BSCCO-2 is then set down on graphene. Now we may increase the temperature to 65 °C to release both BSCCO #1 and #2. The completed stack is shown in the lower right-most panel of Figure 23 (b). In some situations, it may be better to simply melt the PPC at 90 °C and dissolved it away in acetone later without contaminating the BSCCO-Gr interface. Using this dry and mechanical technique, we have made several BSCCO-Gr-BSCCO devices with junction lengths ranging from <100 nm to 3 um.

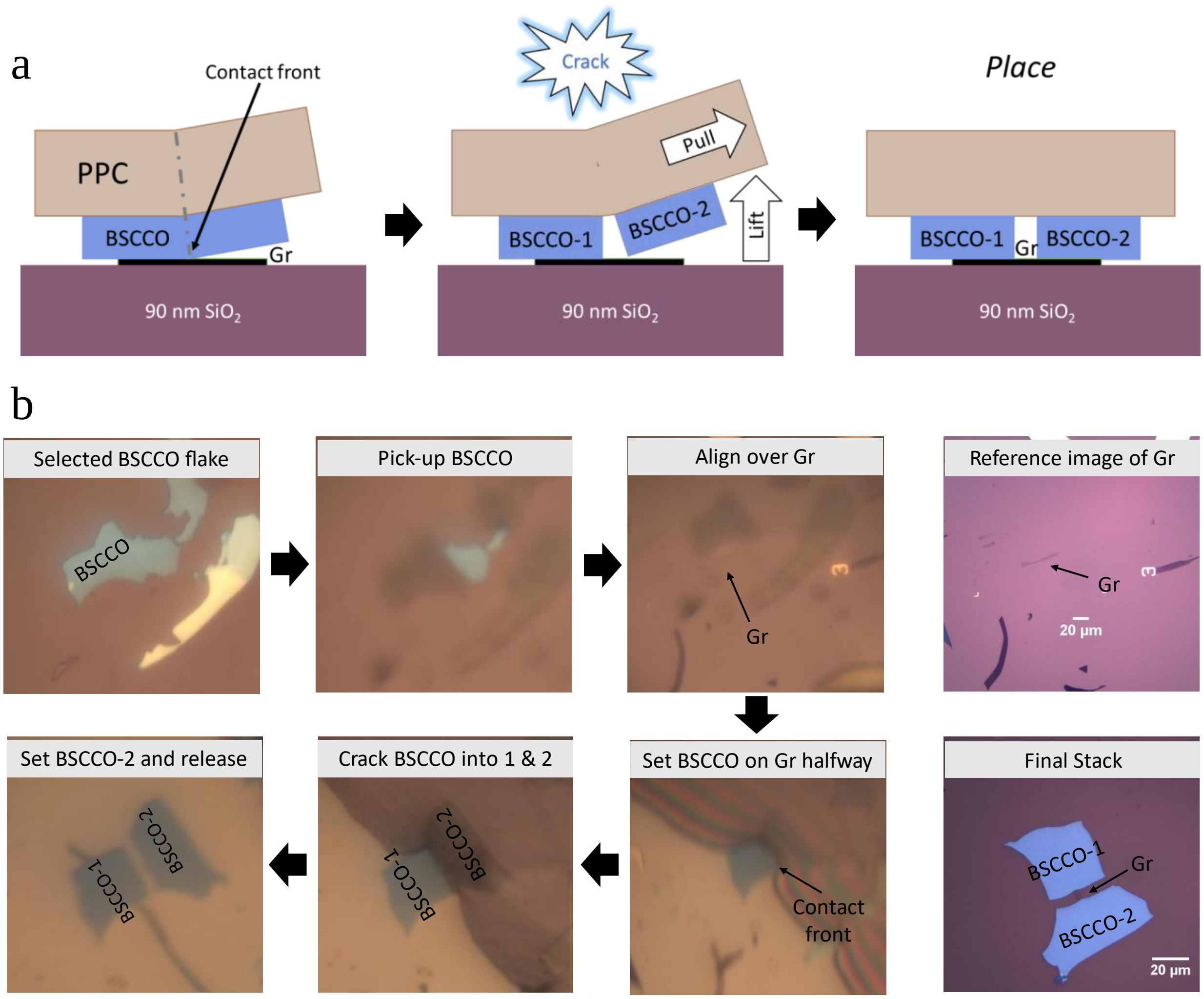

Figure 23. (a) Schematic of using mechanical movements of the stamp to induce a continuous crack in a BSCCO flake. (b) Optical images of cracking a BSCCO flake into two individual pieces to make the BSCCO-Gr-BSCCO stacks. To the top right is a reference image of graphene and bottom right is an image of the completed stack with junction length ~5 µm.

6.6 Lithography

Photolithography and e-beam lithography (EBL) were used to make different types of contacts to BSCCO and graphene in the devices which led to the results on conductance resonances. The details of these processes are described in this section. In addition, we will compare a patterning process to etch trenches in BSCCO, in lieu of using the cracking method discussed in Section-6.5, to achieve BSCCO-Gr-BSCCO junctions.

The steps involved in device fabrication are summarized in Figure 24 and listed below. The sub-sections 6.6.1 and 6.6.2 delve into the details of the lithography processes. Selectively etching and obtaining tunnel contacts to BSCCO are respectively described in 6.6.3.

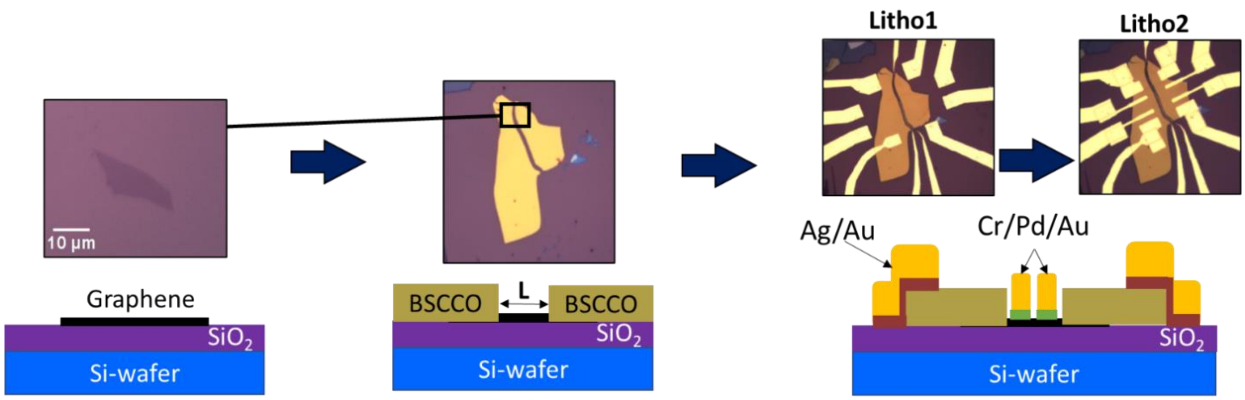

Figure 24. Optical images and schematics showing progression from a single graphene flake to a stack and finally to a device.

a) Start with clean pieces of 90nm SiO_2 wafer.

b) Pattern alignment marks and deposit Ti (3 nm) + Au (>20nm).

c) O_2/Ar Plasma treat wafers to improve yield of monolayer graphene.

d) Exfoliate graphene.

e) Optically map and collect Raman spectra of candidate graphene flakes.

f) Anneal graphene bearing samples in Ar/H_2 at 300 °C for 3 hours.

g) Assemble BSCCO/Gr and or BSCCO-Gr-BSCCO stacks.

h) Litho-1: E-beam lithography

i) Fabricate all probe pads and ohmic contacts to graphene in BSCCO/Gr devices or long channel BSCCO-Gr-BSCCO devices.

j) Deposit Ti (3 nm) + Au (40 nm) using e-beam evaporator.

k) Litho-2: Photolithography

l) Fabricate ohmic contacts to BSCCO.

m) Deposit Ag (10 nm) + Au 50 (nm) using e-beam evaporator.

n) Perform metal lift-off and/or solvent bath to dissolve resist residue.

6.6.1 E-beam lithography

We used the Raith Voyager 50 keV e-beam lithography system to pattern alignment marks on plain SiO_2 wafers, create electrical contacts to stacks, and define shapes in graphene and BSCCO for dry/wet etching. The Voyager system has a very precise piezo stage (<20 nm backlash) which makes it easy to achieve <100 nm accuracy in level-to-level alignment without the need for scanning marks. However, the marks are required to match 3 locations on the sample to the same 3 locations in the layout design file to achieve level-to-level alignment. The pitch, area covered, and unique identifiers of the mark array need to be defined to correctly identify candidate flakes. After we pattern the mark array, we deposit Ti (3) nm + Au (>20 nm) and perform the graphene exfoliation as described before. After the stacks are assembled, we collect optical images at two different magnifications which are then imported into the Voyager's own CAD software. Each optical image needs to contain unique marks to exactly match the location of the graphene flake or stack between the sample and design file. Because we will need to expose contacts to BSCCO from a photomask in *Litho-2*, we import and overlay their CAD designs into the *Litho-1* design file and draw the e-beam features for contact pads around them, see Figure 25.

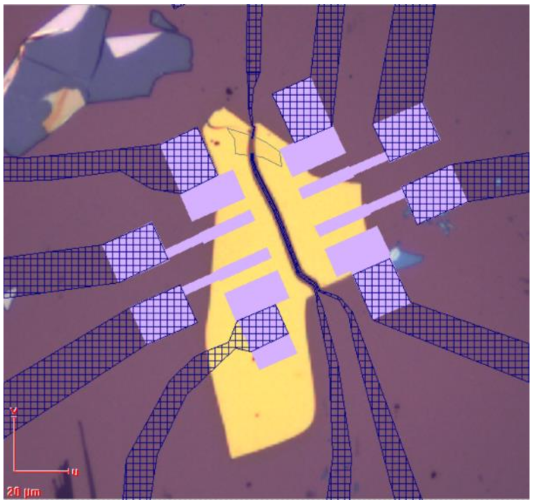

Figure 25. Optical image of the stack from Figure 24 imposed in the *Litho-1* design file to expose contacts to graphene and contact pads for BSCCO (filled in navy blue mesh). The features of photomask contacts to BSCCO (in lavender) are overlayed here to aid the alignment between *Litho-1* and *Litho-2*. The scale bar in red located at the bottom left-hand corner is 20 μm in both axes.

Once the designs are finalized, we follow the steps below:

1. Spin coat MicroChem (now Kayaku Inc.) PMMA-A4 950K on the sample at 3000 rpm.
2. Bake the PMMA covered sample at 165 °C for 15 minutes. Although the
3. Cool by blowing N_2. Remove any dust/debris. Clean bottom surface of the wafer.
4. Follow through standard operating procedure to complete patterning steps in the Voyager. PMMA is a positive tone resist, i.e., areas exposed to the electron beam are dissolved away during development ("what shows, goes"). Dose needs to be assigned correctly to make <5 kΩ ohmic contacts to any leads with a critical dimension <1 μm. Usually, a dose factor of 1.2X to 1.3X multiplied to the base does of 580 $\mu C/cm^2$ (10 nm step size) has worked well.
5. Soak the sample in MIBK-IPA (1:3) for 1 minute to develop the exposed regions in PMMA.
6. Deposit metal for contacts using e-beam evaporator. OR etch graphene using oxygen plasma.

7. After metal evaporation, soak the sample in hot acetone (80 °C) for 2 minutes and then lift-off the unexposed regions by agitating the liquid with a pipette. OR simply soak in acetone to dissolve resist after graphene etching. Then, the sample may be allowed to sit in PG Remover for 5 to 10 min at 60 °C to remove residual PMMA.
8. Rinse with IPA and dry with N_2.

We have also used this e-beam lithography processes to create Ti/Au tunneling contacts (>10 MΩ) to BSCCO. Tunneling measures the density of states of superconductors, i.e., the size and qualitative nature of the superconducting gap. This basic study is shown in Appendix.

6.6.2 Ohmic contacts to BSCCO

Ohmic contacts to BSCCO are necessary to perform four-terminal (Van der Pauw) resistance measurements of the BSCCO/Gr and the BSCCO-Gr-BSCCO junctions, and remove any series contact resistance. If the contacts to BSCCO are non-ohmic and have high resistance (>1 MΩ) at cryogenic temperatures, they can measure tunneling current. But they cannot accurately measure voltage, which is necessary for four terminal resistance measurements. Establishing ohmic contacts to BSCCO has required special steps like Ar ion milling to remove sacrificial layer before metal deposition or using a shadow mask for sputter deposition in an inert environment. However, these methods require specialized equipment and process development before they yield good results. We briefly attempted to develop an Ar plasma to etch BSCCO after lithography in the e-beam evaporator before depositing metal without breaking vacuum. But the finished contacts were not ohmic, possibly because the ion energy was insufficient to mill the top insulating layers of BSCCO. We found success using a photolithography process to consistently achieve contact resistance of few hundred ohms, as described below.

1. Clean the SiO_2/Si wafer carrying BSCCO-Gr stacks in acetone to remove any PPC residue and rinse with IPA. Dry with N_2.
2. Spin-coat the wafer LOR (lift-off resist) 3A at 4000 rpm for 1 minute. Bake it at 180 °C for 3 minute to cure the resist. Let it cool down to room temperature.
3. Then, spin-coat Shipley resist SR1813 on the wafer at 4000 rpm for 1 min. Bake it at 90 °C for 1 minute and then allow it to cool down.
4. Expose the sample for 2.8 to 3 seconds to a suitable multi-terminal pattern on the photomask using the OAI MDL 800 mask aligner (lamp intensity 22 – 25 mW/cm^2).
5. Develop the exposed wafer in AZ-300 MIF (metal ion free, 2.3% TMAH) solution for 45 seconds in a petri-dish while holding it with a tweezer. Rinse with deionized H_2O – this will not degrade BSCCO because it is protected with photoresist. It will only rinse away the developer from the exposed areas. We then dry with N_2 and briefly inspect under a microscope with a low mag objective (objectives >20X can further dose the resist if there is any UV in the light source) to check if the resist has cleared. Safely discard AZ-300 MIF.
6. Prepare a fresh petri-dish of AZ-300 MIF for the next step which is the key to creating ohmic contacts to BSCCO (>20 nm thick). We dip the sample again in AZ-300 MIF for 20-30 seconds and rely on TMAH to etch away the sacrificial layers of BSCCO. Rinse with deionized H_2O, followed by IPA, and dry with N_2.
7. We deposit Ag (10 nm) and Au (40) without breaking vacuum in an e-beam evaporator.
8. Perform metal lift-off in hot acetone (80 °C). LOR is not removed.
9. Dissolve the LOR layer in PG remover at 60 °C for 5-10 min.
10. Rinse with IPA and dry with N_2.

Making contacts to BSCCO has been the last step for most devices. After the final optical inspection, the devices are loaded in the LakeShore CPX-VF cryogenic probe station and kept under vacuum. We test all BSCCO and graphene contacts before cooling.

6.6.3 Selective etching of BSCCO

Prior to pursuing the cracking technique described in Section 6.5, we had explored selective etching of BSCCO to create sub-100 nm BSCCO-Gr-BSCCO junctions. Figure 26 (a) is an optical image of lines of different widths exposed in PMMA A4 over the edge of a 53 nm BSCCO flake. The sample was then dipped in 20% TMAH for ~1.5 minutes at room temperature to etch the exposed BSCCO and rinsed in DI water, giving an etch rate of ~20nm/min. We increased the etch rate to 120 nm/min using buffered 2.3% TMAH solution of AZ-300 MIF at 60 °C, the etched trench. This process was tested on a BSCCO/graphene stack shown in Figure 26 (c) and can easily create gaps in the 100 nm range (see Figure 26 (d)). Qualitatively, these side walls are tapered and the spacing at the bottom of the trench is 125 nm, whereas it was designed to be 50 nm. Blow-out of about 3 to 4 X was seen in lines designed to be 20, 50 and 100 nm. The selective etching method did show potential but required process development to control blow-out issues, trench profile, and possible residue at the bottom of the trench.

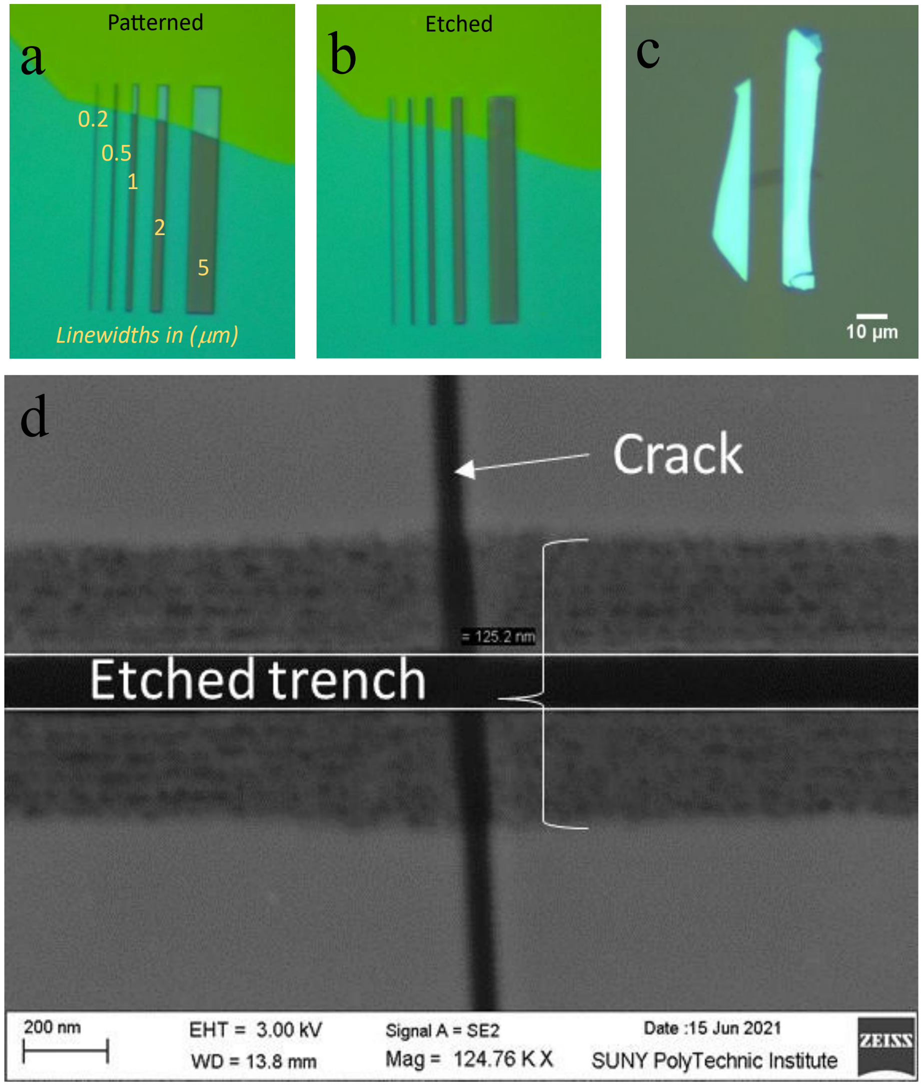

Figure 26. Top - Exposed boxes in PMMA A4 of increasing linewidths on 53 nm BSCCO (a) patterned and (b) etched using 20% TMAH. (c) A large trench cleared in BSCCO which exposed graphene underneath. (d) Electron micrograph of a 60 nm crack intersecting a selectively 125 nm etched trench in BSCCO.

References

1. Wang, L. High Quality Graphene Devices in Graphene-Boron Nitride Systems. (Columbia University, 2014).
2. Lee, M. Ballistic Conduction in Graphene Heterostructures. (Stanford University, 2016).

3. Frisenda, R. *et al.* Recent progress in the assembly of nanodevices and van der Waals heterostructures by deterministic placement of 2D materials. *Chem Soc Rev* **47**, 53–68 (2018).

4. Dean, C. R. *et al.* Boron nitride substrates for high-quality graphene electronics. *Nat Nanotechnol* **5**, 722–726 (2010).

5. Wang, L. *et al.* One-Dimensional Electrical Contact to a Two-Dimensional Material. *Science (1979)* **342**, 614–617 (2013).

6. Pizzocchero, F. *et al.* The hot pick-up technique for batch assembly of van der Waals heterostructures. *Nat Commun* **7**, (2016).

7. Geim, A. K. & Grigorieva, I. v. Van der Waals heterostructures. *Nature* **499**, 419–425 (2013).

8. Cao, Y. *et al.* Unconventional superconductivity in magic-angle graphene superlattices. *Nature* **556**, 43–50 (2018).

9. Zhao, S. Y. F. *et al.* Emergent Interfacial Superconductivity between Twisted Cuprate Superconductors. (2021).

10. Arora, H. S. *et al.* Superconductivity in metallic twisted bilayer graphene stabilized by WSe_2. *Nature* **583**, 379–384 (2020).

11. Kim, J. *et al.* Observation of plateau-like magnetoresistance in twisted Fe_3GeTe_2/Fe_3GeTe_2 junction. *J Appl Phys* **128**, (2020).

12. Sharpe, A. L. *et al.* Emergent ferromagnetism near three-quarters filling in twisted bilayer graphene. *Science (1979)* **365**, 605–608 (2019).

13. LaGasse, S. W., Dhakras, P., Watanabe, K., Taniguchi, T. & Lee, J. U. Gate-Tunable Graphene–WSe_2 Heterojunctions at the Schottky–Mott Limit. *Advanced Materials* **31**, 1901392 (2019).

14. Blake, P. *et al.* Making graphene visible. *Appl Phys Lett* **91**, 063124 (2007).

15. Anzai, Y. *et al.* Broad range thickness identification of hexagonal boron nitride by colors. *Applied Physics Express* **12**, 055007 (2019).

16. Ferrari, A. C. & Basko, D. M. Raman spectroscopy as a versatile tool for studying the properties of graphene. *Nature Nanotechnology* vol. 8 235–246

7. BSCCO/Graphene Junctions

This chapter is an expanded description of our work published in Physical Review Letters*.

Electronic scattering processes in condensed matter systems are typically driven by a single mechanism and rarely lead to resonances. Examples include tunneling phenomena in semiconductors, confinement in low-dimensional systems, Andreev bound states in superconductors (SC)[1], and Yu-Shiba-Rusinov states in superconductor-ferromagnet junction [2]. Here, we show the appearance of resonances due to the combination of two scattering mechanisms. Andreev reflection (AR), associated with superconductor/metal interfaces, and Klein tunneling (KT)[3–5], associated with Dirac fermions, occur together[6,7] in our BSCCO/graphene junctions. The long carrier coherence attests to the pristine quality of our devices, which allows the Fabry-Pérot process that manifests from these scattering processes. We estimate the length of the resonance region from the oscillation period. Our results are supported by calculations of the spectral functions for graphene with proximity-induced nodal superconductivity and the emergent resonant modes in the junction (credit is given to Prof. Jose Lado, Aalto University).

The understanding of transport in the BSCCO/graphene junction has been of interest in the graphene research community since the development of the dry transfer techniques[8–10]. The initial experimental advancement was hampered by the degradation of BSCCO, as explained in Chapter-4.2. To overcome these challenges, we minimize the degradation of exfoliated BSCCO flakes by assembling the heterostructures in the glovebox and using special photolithography and

---

* 1. Jois, S., Lado, J. L., Gu, G., Li, Q. & Lee, J. U. Andreev Reflection and Klein Tunneling in High-Temperature Superconductor-Graphene Junctions. *Phys. Rev. Lett.* **130**, 156201 (2023).

fabrication techniques to achieve ohmic contacts (<500 Ω) to bulk BSCCO. The details of these methods have been discussed in Chapter-6. The basic electrical measurements show the expected high T_c~85 K for pristine BSCCO in a majority of our devices, as shown in Figure A2. We also measured the intrinsic pseudo-gap in a BSCCO device with tunneling contacts and found $\Delta \sim 40$ meV, also comparable to previous reports. See Appendix-1 for these results.

The first section of this chapter presents the device structure. We will see how the scattering region (Gr') can be naturally formed in BSCCO/graphene junctions without requiring a local gate as first suggested by theory[11]. The Gr' region renders two different interfaces with different properties. Next, we see how modulating the global gate to tune the Fermi level in the Gr' and bare graphene (Gr) regions leads to the conductance oscillations predicted for tunable barriers in superconductor-graphene junctions[12,13], discussed in Chapter-5. Furthermore, we present our analysis on the origin of the resonance with evidence for KT by the conductance asymmetry, discussed in Chapter-2.4, and for AR by the bias dependence of the resonance amplitude. The microscopic mechanism for the single particle interference is explained, in light of a Fabry-Perot process. Then, the electronic spectral functions for the different regions of graphene in the device are presented along with the calculated junction conductance, to support the experimental findings. Lastly, we share preliminary results with an applied magnetic field.

7.1 Device details

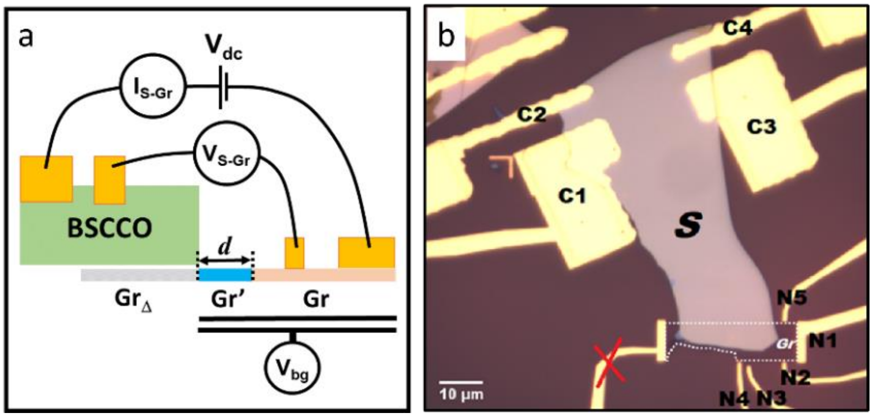

Figure 27. (a) Schematic cross-section of our device. Gr_{Δ} is superconducting graphene under BSCCO, Gr' is a p-doped graphene and Gr is native graphene. *d* is the length of Gr'. The dotted lines at either ends of Gr' denote the interfaces. (b) Optical micrograph of device-A from Table-1. S is shorthand for BSCCO. Dotted white outline tags graphene. The red X and N1 to N5 are contacts to graphene. C1 to C4 are contacts to BSCCO. Scale bar is 10 µm.

Three distinct regions of graphene form in our BSCCO/Gr junction. The regions are indicated as Gr_{Δ}, Gr', and Gr in Figure 27 (a). Gr_{Δ} is the portion of graphene under BSCCO that has a nodal proximity-induced superconducting gap (Δ_i). BSCCO is a hole-doped superconductor with a high carrier density[14] of 10^{15} cm^{-2}. BSCCO in contact with graphene, having lower carrier density (10^{12} cm^{-2}), transfers charge to create a *p*-doped Gr' region of length d, in addition to heavily doping Gr_{Δ}. A similar charge transfer process occurs in metal/graphene junctions[15]. The dotted line between the Gr_{Δ} and Gr' regions indicates the interface which is responsible for AR. At the other end of the Gr' region is another dotted line to indicate the second interface with native graphene Gr which is responsible for KT. Therefore, the superconducting Gr_{Δ} region is connected to Gr'-Gr regions that form a *p*-*n* junction by a gate. Modulation of the gate results in an asymmetric conductance as the doping in the Gr'-Gr regions changes from p^+-p to p-n, as we show in Figure 28 (b) and Figure 29 (a), beyond what was previously reported in YBCO/graphene junctions[16,17]. Previous studies created potential walls in bipolar graphene junctions (p-n-p). These partially reflective interfaces confine carriers that led to Fabry-Pérot resonances[18–20] from KT alone. The resonance condition occurs within one round-trip. On the other hand, the Gr_Δ-Gr'-Gr junction described here is an SC-p-n junction (Gr_Δ is a highly p-doped SC) with the two interfaces having different reflection properties that modify the interference condition that requires two round-trips. Here, we present results on gating BSCCO/graphene junctions in which we observe resonances from the interplay of KT and AR owing to the two different interfaces that occur naturally in our junctions.

7.2 Transport

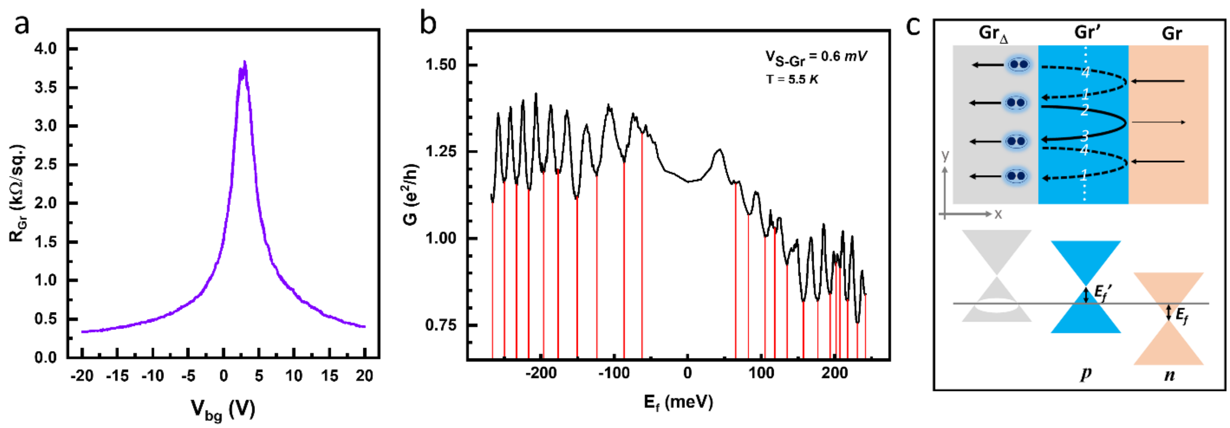

Figure 28. (a) Sheet resistance of typical bare graphene in our devices. (b) Conductance of BSCCO/Gr (device-A) junction in response to sweeping the Fermi-energy E_f The red lines indicate the position of the troughs. (c) Top - A p-n junction is formed in Gr'-Gr by electrostatic gating. The classical trajectory of the holes and electrons is depicted by dashed and solid lines respectively. The number labels count the trips for the interference condition.

The typical sheet resistance (R_{Gr}) of graphene in our devices in response to the sweep up and sweep down (dual sweep) of gate voltage (V_{bg}) is shown in Figure 28 (a). The resistance maxima for the Dirac point (V_{DP}) are often found to be between 0 V and +5 V, indicative of slight hole doping from the substrate. It is typical to neglect the substrate-induced doping by subtracting V_{DP} from the gate voltage, which we follow here. R_{Gr} is hysteresis-free at all temperatures, down to 4.2 K, suggesting little charge trapping at the graphene/SiO_2 interface. The four-terminal conductance of the BSCCO/graphene junction of device-A in Figure 28 (b) is measured as we sweep the gate, which acts on the non-superconducting regions Gr and Gr'. The gate voltage sets the Fermi level in graphene as $E_f = sign(V_{bg} - V_{DP})\, \hbar\, v_f \sqrt{\pi\, C_{bg} \frac{|V_{bg}-V_{DP}|}{e}}$, where $\hbar$ is the reduced Planck constant, $v_f \sim 1 \times 10^6$ m/s is the Fermi velocity in graphene, and $C_{bg} = 38.37$ nF/cm^2 is the gate capacitance for 90 nm SiO_2.

Note that the change in carrier density we can induce in BSCCO using our SiO_2/Si gate is not enough to affect its properties, unlike what is achievable by ionic gating[21,22]. In ionic gating, the voltage is fixed well above 200 K and is not tunable at cryogenic temperatures. The SiO_2 gate on a highly-doped Si wafer allows us to smoothly sweep the gate voltage at all temperatures, enough to modulate the Fermi level in graphene but not in BSCCO.

In Figure 28 (b), $E_f = 0$ for $V_{DP} = +2.2$ V of Gr from our measurement of R_{Gr}. The extent of *p*-doping in Gr' is $E_f' = -180$ meV, which can be inferred from the second conductance minima we observe at the gate voltage of +12 V. To observe the 2nd minima, we had to apply a bias (V_{S-Gr}) of more than 25 meV in Figure 28 (a). The importance of studies on bias dependence is further explained below in Figure 29. The presence of this *p*-doped Gr' region renders the two interfaces that are responsible for the resonant interaction between KT and AR in the junction, on which we will elaborate next.

The gate acts on Gr' and Gr regions simultaneously. When the gate bias is such that we $E_f < 0$, Gr'-Gr regions are in a p^+-p configuration. And when $0 < E_f < -E_f'$ meV, the Gr'-Gr regions are in a *p*-*n* configuration. The bottom panel of Figure 27 (c) shows the doping in the Gr_Δ-Gr'-Gr regions relative to the Fermi-level (gray line) when Gr'-Gr regions are in a p-n configuration. A nodal gap in the Gr_Δ region comes from the proximity to the d-wave order parameter of BSCCO and is further supported by the calculated spectral function in Figure 32 (b). In Figure 27 (b), the conductance asymmetry manifests as a 30% decrease in the average conductance for the p-n configuration compared to the p^+-p configuration. This is due to the reduction in the transmission of carriers that are incident at oblique angles on the *p*-*n* junction[4,23], owing to the chiral nature of carriers in graphene. The observation of the conductance asymmetry shown in Figure 28 (b) and verified in Figure 32 (e) through calculations, is one of the central results of this work.

The other remarkable feature of Figure 28 (b) is the conductance oscillations that exist in both p^+-p and *p*-*n* doping configurations. The top panel of Figure 28 (c) shows the classical trajectories of carriers to visualize the number of round trips in the Gr' region that lead to the resonant condition. Consider the *p*-*n* configuration in Gr'-Gr and a hole (dashed) entering Gr' by KT (top *1*). It impinges on the Gr_Δ-Gr' interface and reflects as an electron (solid) by AR (*2*). The electron (*2*) makes a round trip (*3*) by partial reflection from the Gr'-Gr interface. The returning electron (*3*) travels to the Gr_Δ region and reflects as a hole (*4*). At specific energies, a destructive resonant interference condition occurs every two round trips among carriers of the same charge, traversing in opposite directions in the Gr' region. The smaller width of the arrows in the Gr region indicates reduced transmission. The described resonant process is unchanged for p^+-p, except with higher transmission at the Gr'-Gr interface. The resonant mechanism is analogous to Fabry-Pérot resonances but requires two full round trips ($4 \times d$) as opposed to one round trip. The momentum-resolved spectral function in Figure 32 (c) of the Gr' region corroborates the formation of resonant modes. We note that tunneling into a nodal d-wave superconductor should lead to weaker AR compared to a system with an s-wave superconductor[11,13]. However, the significantly shorter coherence length of BSCCO compared to that of a conventional s-wave superconductor allows the formation of the three distinct regions needed to observe the resonances we report. On the other hand, quasi-periodic oscillations were observed in a Van der Waals $NbSe_2$/graphene junction[24], whose origin was reported to be unclear. The resistance of bare graphene in that work appeared to have oscillations with gating, which could be attributed to universal conductance fluctuations from disorder appearing below 1 K. The same could be the reason for seeing fluctuations in their $NbSe_2$/graphene junction conductance.

The positions of the troughs in Figure 28 (b) are highlighted in red. $E_{tr-tr} \sim 17.3$ meV is the average period of resonances in energy for device-A. The average period in gate voltage across all devices A through E is ~1.7 V, see Appendix (Figure A5). The small change in the period between p^+-p and p-n doping configurations can be attributed to the change in d with gating. We also note that resonances are less pronounced at low doping. It is likely that the energy broadening $\delta\epsilon_f = 50$ meV around the Dirac point from charge puddles[25] in the SiO_2 washes out the oscillations.

Next, we estimate the length d of the Gr' region from the oscillation period. The two round-trips of the scattering region give us a path length of $4d = n\,\lambda_f = n\,\frac{2\pi}{k_f}$, as the resonance condition. Here, λ_f and k_f are the Fermi wavelength and wavevector, respectively, and n is the integer index at resonance. Using the graphene dispersion relation $E = \hbar v_f k_f$, we arrive at the resonant condition,

$$E = \frac{nhv_f}{4d} \tag{1}$$

from which we can calculate the length *d*.

From Eq.-(1), the length of Gr' is *d*~59 nm. The values for E_{tr-tr} and *d* for all the devices in Table **1** are similar, regardless of other junction parameters such as T_c and junction resistance which can vary. The mean free path $\lambda_{mfp} \sim 80$ nm which we estimate, using $\sigma = \left(\frac{2e^2}{h}\right) k_f \lambda_{mfp}$, is longer than the estimated length of the Gr' region. Billiard ball trajectories of carriers are expected from phase-coherent transport[26] within the Gr' region. The phase coherence length is estimated to be $29 - 56$ nm using the expression $L_\phi = \sqrt{Dt_\phi}$, where the diffusion coefficient $D = v_f \times \frac{\lambda_{mfp}}{2} = 0.04$ m^2/s and the dephasing time t_ϕ can range between $22 - 80$ fs[27].

Table 1. Properties of the junctions examined in this work: T_C is the transition temperature of BSCCO, W is the junction width, $\boldsymbol{R \times W}$ the junction resistance, $\boldsymbol{E_{tr-tr}}$ the period of oscillations, and $\boldsymbol{d}$ the estimated length of the Gr' region, $\boldsymbol{\Delta_i}$ from bias dependence of oscillations.

Device #	**T_c** (K)	**$W_{S\text{-}Gr}$** (μm)	$\boldsymbol{R \times W}$ (kΩ μm)	$\boldsymbol{E_{tr-tr}}$ (meV)	$\boldsymbol{d}$ (nm)	$\boldsymbol{\Delta_i}$ (meV)
A	85	28.2	628.24	17.3	59	15
B	84	26.8	639.23	16.1	64	10
C	70	4.8	29.85	15.9	65	12
D	85	5.8	92.85	19.4	53	10
E	85	4.0	36.00	17.3	60	12

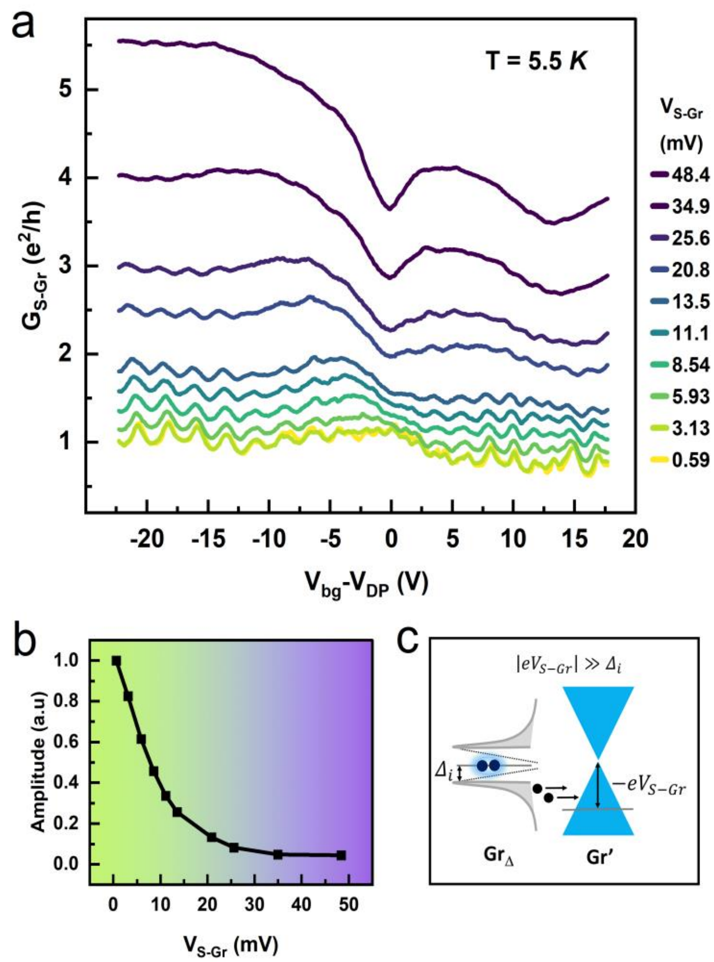

Figure 29. (a) Conductance of the S-Gr junction as a function of the back-gate voltage V_{bg} measured at different $V_{\mathrm{S-Gr}}$, corrected for the position of the Dirac point V_{DP} of Gr at +2.3 V (b) Amplitude of the oscillations as a function of the bias across the junction decays beyond ~15 mV. The solid curve is a guide to the eye. (c) A schematic representation of carriers outside of the pseudogap of Gr_Δ entering Gr' when $V_{\mathrm{S-Gr}} \gg \Delta_i$ across the junction.

The contribution of AR to the resonance is evident by the decay in the oscillation amplitude when the bias is larger than the induced gap, as seen in Figure 29 (a, b). Figure 29 (a) is a plot of the junction conductance as the bias $V_{S\text{-}Gr}$ across the junction is increased. In Figure 29 (a), the increasing Fermi window allows the injection of carriers from outside of the induced superconducting gap in graphene, Δ_i, (see Figure 29 (c)) which suppresses the resonances. Figure

29 (b) shows that the normalized oscillation amplitude decays when $V_{S\text{-}Gr}$>15 mV and implies Δ_i ~15 meV for device-A. We observe the same behavior in the other devices with the inferred Δ_i from bias dependence ranging between 10-15 meV. This variation is expected due to the sensitivity of the proximity effect from fabrication non-uniformities. A comparable magnitude of Δ_i has been seen in BSCCO heterojunctions with other 2D materials[10,28]. The differential resistance for devices A and B from Table **1** is shown below in Figure 30, which further corroborates our inference of Δ_i. Refer to the discussion in Chapter-5.2 on the induced superconducting gap in BSCCO/graphene junction in tunneling[10] and from Andreev reflection in junctions of BSCCO with Dirac materials like Bi_2Te_3 and graphite[28,29]. Also note that this is much smaller than the intrinsic gap of BSCCO ($\Delta_0 = 40$ meV) measured by others[22,30] and verified by us in a tunneling experiment shown in

Appendix.

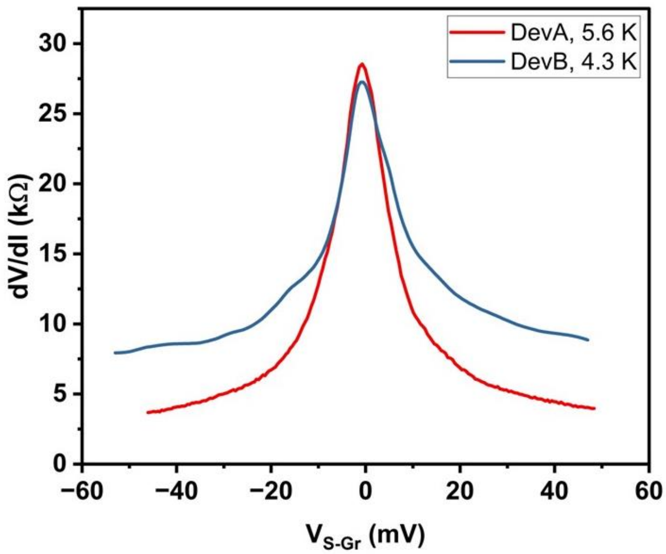

Figure 30. Differential resistance (dV/dI) of two BSCCO/Gr junctions at liquid helium temperature showing an induced pseudo-gap Δ_i below 15 mV.

The resonances are robust with temperature for device-A, as shown in Figure 31 (a). We show the relative oscillation amplitude for another device (similar to device-A) in Figure 31 (b) by subtracting the background resistance. We observe oscillations that persist up to 40 K. This observation is consistent with the temperature dependence of Δ_i reported by others[31].

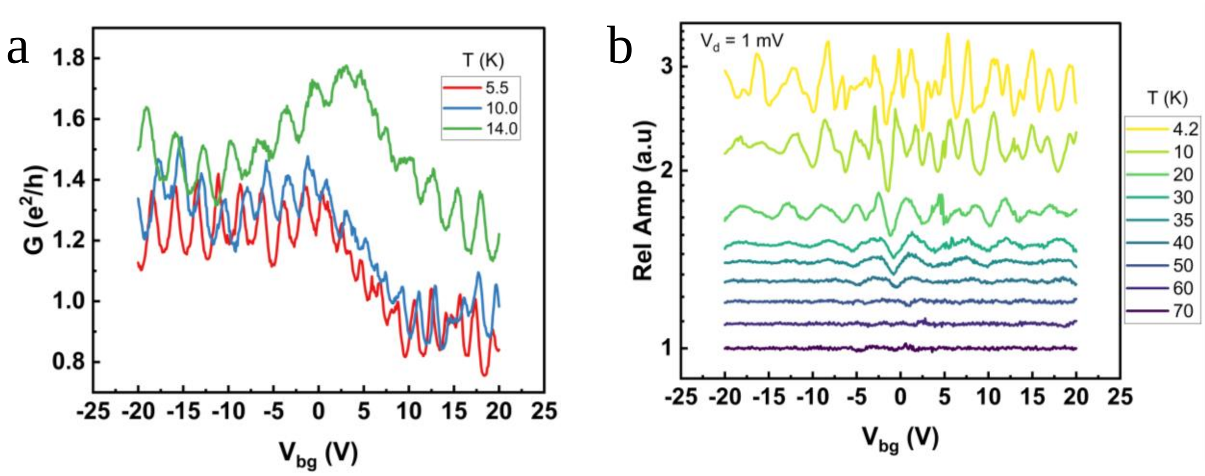

Figure 31. (a) Junction conductance for device-A is discussed in the main text at different temperatures. (b) The relative amplitude of the resonances of another BSCCO/Gr junction showing the amplitude decreasing as the critical temperature of BSCCO (T_c ~ 72 K) is approached.

The electronic properties of the junction are captured using an effective low-energy model Hamiltonian of the form:

$$\mathcal{H} = \mathcal{H}_{\text{kin}} + \mathcal{H}_{\text{SC}} + \mathcal{H}_{\mu}$$

with

$$\mathcal{H}_{kin} = t \sum_{\langle i,j \rangle, s} c_{i,s}^{\dagger} c_{j,s} + h.c.$$

capturing the kinetic energy of electrons, where $c_{i,s}^{\dagger}$ is the creation operator on site i and $c_{j,s}$ is the annihilation operator on site j, with pseudo-spin index s. The nearest-neighbor hopping energy is $t = 2.7$ eV, and $\langle\ \rangle$ denotes the sum over the first neighbors. The term

$$\mathcal{H}_{\text{SC}} = \mu_{\Delta} \sum_{\langle ij \rangle \in \text{Gr}_{\Delta}, s} \Delta_{ij} c_{i,\uparrow} c_{j,\downarrow} + h.c$$

accounts for the superconducting proximity effect, where Δ_{ij} is defined such that its Fourier transform leads to a $d_{x^2-y^2}$ order parameter in reciprocal space. Finally, the term

$$\mathcal{H}_\mu = \mu_\Delta \sum_{i\in \mathrm{Gr}_\Delta, s} c_{i,s}^\dagger c_{i,s} + \mu'_{\mathrm{bg}} \sum_{i\in \mathrm{Gr}', s} c_{i,s}^\dagger c_{i,s} + \mu_{\mathrm{bg}} \sum_{i\in \mathrm{Gr}, s} c_{i,s}^\dagger c_{i,s}$$

controls the local chemical potential in the different regions, to account for the experimental conditions. The difference in screening in the Gr and Gr' regions affect the position and tunability of their chemical potentials. The chemical potential is defined as $\mu_{\mathrm{bg}} = 0.06t + \mu'_{\mathrm{bg}}$. This way, the gating parameters relate closely to the experimentally applied bias V_{bg}, and the shift $\mu'_{\mathrm{bg}} = -0.06t \approx -162$ meV corresponds to the doping in the Gr' region when $V_{\mathrm{bg}} - V_{DP} = \mu_{\mathrm{bg}} = 0$. The chemical potential in Gr_Δ is set to $\mu_\Delta = 0.2t$, which arises due to charge transfer from BSCCO and remains constant due to screening. The gating parameters defined here are comparable to experimental observations from Figure 29.

We define a junction that is infinite in the y-direction, and a finite Gr' region is defined between the two semi-infinite Gr_Δ and Gr regions, as depicted in Figure 28 (c). Due to the translation symmetry in y, the spectral function of the junction can be labeled according to the parallel momenta $\mathbf{k}_\parallel$ to the interface. The previous Hamiltonian is solved with the Bogoliubov-de Gennes formalism, and we compute the electron spectral function at the Gr' region defined as

$$A(\mathbf{k}_\parallel, \omega) = -\frac{1}{\pi} \mathrm{Tr}'_{\mathrm{Gr}} \mathrm{Im}[P_e \mathcal{G}(\mathbf{k}_\parallel, \omega)]$$

where P_e is the projection operator in the electron Nambu sector and $\mathcal{G}(\mathbf{k}_\parallel, \omega)$ is the full Nambu Green's function of the system. $A(\mathbf{k}_\parallel, \omega)$ is used to directly extract the electronic excitation emerging in the junction and is computed with the Green's function re-normalization algorithm[32].

The respective spectral functions in doped graphene in the absence and presence of a d-wave superconducting proximity effect are shown in Figure 32 (a) and (b). It is observed in Figure 32

(b) that the proximity to a *d*-wave superconductor opens a momentum-dependent electronic pseudo-gap structure in graphene. Panels (c, d) of Figure 32 shows the momentum-resolved spectral function at the center of the Gr' region, featuring the emergence of resonant modes. The increase in oscillatory single-particle states of Figure 32 (d) shows the sensitivity of the resonances to gating. A zero-energy state is present the electronic spectrum for the Gr’ region, shown in Figure 32 (c) and (d). This due to constructive interference of electrons and holes (mid-gap states) present along the [110] direction of present in the *d*-wave order parameter[33,34].

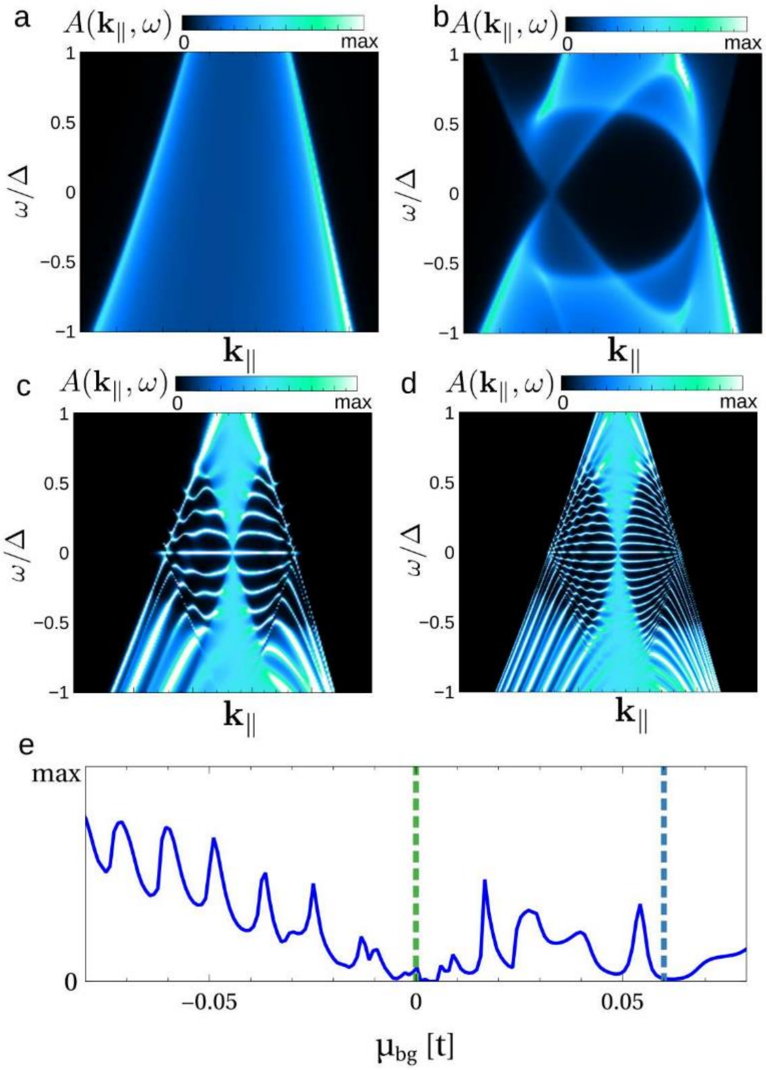

Figure 32. (a) Bulk spectral function for doped graphene, and doped graphene in the presence proximity induced d-wave superconductivity (b). Panel (c, d) shows the spectral function for the (c) unbiased and (d) biased gating conditions in the Gr' region. Panel (e) shows the computed $\mathrm{dI/dV}$ at $V_{\mathrm{S-Gr}} = 0.07 \times \Delta$, with the locations of the conductance minima of Dirac points marked by green ($\mu_{\mathrm{bg}} = 0$) and blue ($\mu_{\mathrm{bg}} = 0.06t$) dashed lines for the Gr and Gr' regions respectively. (Theory and figure were contributed by our collaborator J. Lado. Published)

Experimental reports have extensively studied KT and AR, but independently. In a previous study from our group, we reported angle-dependent transport properties of KT in graphene *p-n* junctions[23]. The *p-n* junction resistance is relatively small, about several hundred ohms for a 1 μm wide junction, because graphene is gapless[35] (refer to Chapter-2.4 for more detail). The same could be said about AR for a highly transmissive contact. In current devices, one would not be able to observe these resistances if we simply treated these scattering mechanisms as series resistances. The reduction of single particle states in the Gr' region, seen in Figure 32 (c and d), can cause the measured resistance of the BSCCO/graphene junction to be higher than the individual resistances associated with AR and KT.

To show the impact of those resonances in transport, the conductance of the entire junction $G(\omega)$ was calculated using the non-perturbative $\mathcal{S}$-matrix formalism[36–39]. The resultant conductance as we vary the Fermi energy in the Gr'-Gr regions is shown in Figure 32(e) for low excitation energy. The minimum conductance at $E = 0$, marked by the green dashed line corresponds to the Dirac point of the Gr region. The conductance asymmetry between the p^+-p configuration ($E < 0$) versus *p*-*n* configuration ($E > 0$) of the Gr'-Gr regions is evident, as also seen in the experiment.

Figure 32 (c, d) shows that gating the Gr' region causes the resonant states to change their separation in energy and redistribute the spectral weight of the single particle states. These changes to the electronic spectrum in the Gr' region can reduce the period of resonances and increase overall conductance, as seen in computation (Figure 32 e) and experiment (Figure 28 b). We also see the oscillation amplitude increases as the gate voltage approaches -20V and Gr' becomes more *p*-doped, in Figure 28 (b). The calculated conductance in Figure 32 (e) also supports these observations. Further, we point out the increase in oscillation amplitude with higher doping of the scattering region is related to the increase in the ratio of $d/\lambda_f{}'$, where $\lambda_f' \left(\propto \frac{1}{E_f'}\right)$ is the fermi wavelength of the scattering region. This is consistent with the behavior predicted in theory [13]. The oscillation amplitude in our devices is typically 10-20% of the background conductance, which agrees with the *d*-wave case described in theory[13].

7.3 Magnetic field data

Another experiment we did was to understand the transport properties is to apply a perpendicular magnetic field. In Figure 33 (a), we show the 3D color plot of the junction resistance as a function of gate voltage and magnetic field for device B from Table **1**. The resistance at the Dirac point ($V_{bg} \approx +2.5$ V) increases by more than six times, from 33 kΩ to 250 kΩ at the maximum field we can apply at ± 2.4 T. The resistance along V_{bg} at no field and high field are shown in Figure 33 (b). Surprisingly, there is no noticeable change in the resistance at high doping beyond 10 V. In comparison, the R_{xx} resistance of bare graphene in the device increases three times from 6 kΩ to 18 kΩ, suggesting unique transport properties of the junctions.

We qualitatively explain the magnetic field dependence by considering only the normal mode to the junction since this mode transmits with unity probability at the *p*-*n* junction due to KT. Any perturbation that disrupts the normal mode can severely affect the junction conductance due to the strong angle-dependent transmission of the *p*-*n* junction as discussed in Chapter-2. Magnetic field is one such parameter that can affect the normal mode trajectory due to the Lorentz force.

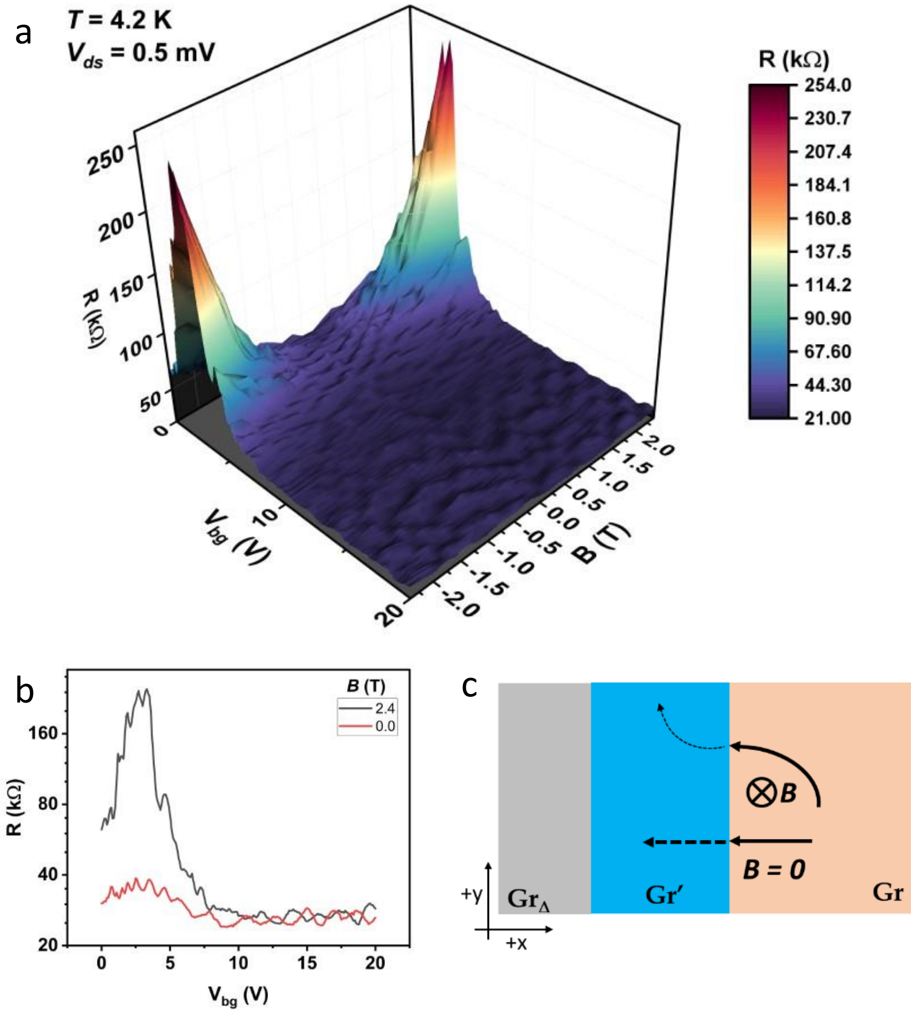

Figure 33. (a) Colormap of the BSCCO/Gr resistance as a function of gate voltage and perpendicular magnetic field for device-B from Table **1**. (b) Line cuts at 0.0 T and 2.4 T from the 3D map. (c) Electron (solid) and hole (dashed) trajectories at the Gr'-Gr interface in the absence and presence of a perpendicular magnetic field. The normal mode when $B = 0$, the transmission $T = 1$ according to KT. However, when $B \neq 0$ the electrons are incident at oblique angles and T decays $\propto e^{-(\sin\theta_i)^2}$.

7.4 Conclusions

In conclusion, we have discussed the origin of resonances found in our BSCCO/graphene junctions by the presence of a *p-n* junction that is formed naturally at the BSCCO/graphene boundary. The *p-n* junction provides one interface for KT. The superconducting graphene provides the other interface for AR. The scattering between these two interfaces results in the resonances with a period of ~17 meV we observe in the junction conductance as a function of gate voltage, as initially suggested by theory[11,13]. The conductance asymmetry observed between the p^{+}-p to p-n configurations in our junctions is consistent with the conductance asymmetry from KT seen in graphene p-n junctions. The oscillations gradually decrease with an increase in bias because of an increase in transmission of single particles from the pseudo-gap of the superconducting graphene region. The amplitude drops by one order of magnitude when the bias energy reaches the expected induced gap between 10-15 meV. We corroborated this from an independent measurement of the induced gap from the differential resistance. For consistency, we also verify the appearance of these oscillations below 40 K with previous temperature studies of induced superconductivity in graphene from BSCCO. Our calculated electronic structure of induced superconductivity in graphene from the d-wave superconductivity in BSCCO shows an expected momentum-dependent pseudo-gap. The spectral function of the scattering region has an oscillating distribution of single particles in energy that are sensitive to gating, consistent with experimental results. Lastly, we have seen an increase in the Dirac point resistance with a perpendicular magnetic up that indicates suppression in specular reflection and sets a precedent for future work.

References

1. Sauls, J. A. Andreev bound states and their signatures. Philosophical Transactions of the Royal Society A: Mathematical, Physical and Engineering Sciences **376**, 20180140 (2018).
2. Kezilebieke, S., Žitko, R., Dvorak, M., Ojanen, T. & Liljeroth, P. Observation of Coexistence of Yu-Shiba-Rusinov States and Spin-Flip Excitations. Nano Lett **19**, 4614–4619 (2019).
3. Katsnelson, M. I., Novoselov, K. S. & Geim, A. K. Chiral tunnelling and the Klein paradox in graphene. Nat Phys **2**, 620–625 (2006).

4. Cheianov, V. v. & Fal'ko, V. I. Selective transmission of Dirac electrons and ballistic magnetoresistance of n-p junctions in graphene. Phys Rev B **74**, 041403 (2006).

5. Reijnders, K. J. A., Tudorovskiy, T. & Katsnelson, M. I. Semiclassical theory of potential scattering for massless Dirac fermions. Ann Phys (N Y) **333**, 155–197 (2013).

6. Burset, P., Herrera, W. & Levy Yeyati, A. Proximity-induced interface bound states in superconductor-graphene junctions. Phys Rev B **80**, 041402 (2009).

7. Beenakker, C. W. J. Colloquium: Andreev reflection and Klein tunneling in graphene. Rev Mod Phys **80**, 1337–1354 (2008).

8. Lee, M. Ballistic Conduction in Graphene Heterostructures. (Stanford University, 2016).

9. Perconte, D. Proximity effect between a high temperature superconductor and graphene. (2020).

10. Wu, Y. et al. The transport properties in graphene/single-unit-cell cuprates van der Waals heterostructure. Supercond Sci Technol **32**, (2019).

11. Bhattacharjee, S. & Sengupta, K. Tunneling conductance of graphene NIS junctions. Phys Rev Lett **97**, 1–4 (2006).

12. Linder, J. & Sudbø, A. Dirac fermions and conductance oscillations in *s*- and *d*-wave superconductor-graphene junctions. Phys Rev Lett **99**, 1–4 (2007).

13. Linder, J. & Sudbø, A. Tunneling conductance in s- and d-wave superconductor-graphene junctions: Extended Blonder-Tinkham-Klapwijk formalism. Phys Rev B Condens Matter Mater Phys **77**, 1–14 (2008).

14. Sterpetti, E., Biscaras, J., Erb, A. & Shukla, A. Comprehensive phase diagram of two-dimensional space charge doped $Bi_2Sr_2CaCu_2O_{8+x}$. Nat Commun **8**, 2060 (2017).

15. Mueller, T., Xia, F., Freitag, M., Tsang, J. & Avouris, P. Role of contacts in graphene transistors: A scanning photocurrent study. Phys Rev B Condens Matter Mater Phys **79**, 245430 (2009).

16. Perconte, D. et al. Tunable Klein-like tunnelling of high-temperature superconducting pairs into graphene. Nat Phys **14**, 25–29 (2018).

17. Perconte, D. et al. Long-Range Propagation and Interference of *d*-Wave Superconducting Pairs in Graphene. Phys Rev Lett **125**, 87002 (2020).

18. Shytov, A. V., Rudner, M. S. & Levitov, L. S. Klein Backscattering and Fabry-Pérot Interference in Graphene Heterojunctions. Phys Rev Lett **101**, 156804 (2008).

19. Young, A. F. & Kim, P. Quantum interference and Klein tunnelling in graphene heterojunctions. Nat Phys **5**, 222–226 (2009).

20. Rickhaus, P. et al. Ballistic interferences in suspended graphene. Nat Commun **4**, 1–6 (2013).

21. Sterpetti, E., Biscaras, J., Erb, A. & Shukla, A. Comprehensive phase diagram of two-dimensional space charge doped $Bi_2Sr_2CaCu_2O_{8+x}$. Nat Commun **8**, 2060 (2017).

22. Liao, M. et al. Superconductor-Insulator Transitions in Exfoliated $Bi_2Sr_2CaCu_2O_{8+\delta}$ Flakes. Nano Lett **18**, 5660–5665 (2018).

23. Sutar, S. et al. Angle-dependent carrier transmission in graphene p-n junctions. Nano Lett **12**, 4460–4464 (2012).

24. Sahu, M. R., Raychaudhuri, P. & Das, A. Andreev reflection near the Dirac point at the graphene-$NbSe_2$ junction. Phys Rev B **94**, 235451 (2016).

25. Dean, C. R. et al. Boron nitride substrates for high-quality graphene electronics. Nat Nanotechnol **5**, 722–726 (2010).

26. Miao, F. et al. Phase-Coherent Transport in Graphene Quantum Billiards. Science (1979) **317**, 1530–1533 (2007).

27. Heide, C. et al. Electronic Coherence and Coherent Dephasing in the Optical Control of Electrons in Graphene. Nano Lett **21**, 9403–9409 (2021).

28. Zareapour, P. et al. Andreev reflection without Fermi surface alignment in high-T_c van der Waals heterostructures. New J Phys **19**, 043026 (2017).

29. Zareapour, P. et al. Proximity-induced high-temperature superconductivity in the topological insulators Bi_2Se_3 and Bi_2Te_3. Nat Commun **3**, 1056 (2012).

30. Yu, Y. et al. High-temperature superconductivity in monolayer $Bi_2Sr_2CaCu_2O_{8+\delta}$. Nature **575**, 156–163 (2019).

31. Wu, Y. et al. The transport properties in graphene/single-unit-cell cuprates van der Waals heterostructure. Supercond Sci Technol **32**, (2019).

32. Lopez Sancho, M. P., Lopez Sancho, J. M. & Rubio, J. Highly convergent schemes for the calculation of bulk and surface Green's functions. Journal of Physics F: Metal Physics **15**, 851–858 (1985).

33. Hu, C. R. Origin of the zero-bias conductance peaks observed ubiquitously in high superconductors. Phys Rev B Condens Matter Mater Phys **57**, 1266–1276 (1998).

34. Kashiwaya, S., Tanaka, Y., Koyanagi, M., Takashima, H. & Kajimura, K. Origin of zero-bias conductance peaks in high-Tc superconductors. Phys Rev B **51**, 1350–1353 (1995).

35. Stander, N., Huard, B. & Goldhaber-Gordon, D. Evidence for Klein tunneling in graphene p-n junctions. Phys Rev Lett **102**, 1–4 (2009).

36. Datta, S. Electronic Transport in Mesoscopic Systems. (Cambridge University Press, 1995). doi:10.1017/CBO9780511805776.

37. Blonder, G. E., Tinkham, M. & Klapwijk, T. M. Transition from metallic to tunneling regimes in superconducting microconstrictions: Excess current, charge imbalance, and supercurrent conversion. Phys Rev B **25**, 4515–4532 (1982).

38. Fisher, D. S. & Lee, P. A. Relation between conductivity and transmission matrix. Phys Rev B **23**, 6851–6854 (1981).

39. Lado, J. L. PyQula. Preprint at https://github.com/joselado/pyqula.

8. BSCCO-Gr-BSCCO Junctions

Fabrication and measurement of graphene Josephson junctions using high-temperature d-wave superconductors (HTS), such as $Bi_2Sr_2CaCu_2O_{8+x}$ (BSCCO) and $YBa_2Cu_3O_7$ (YBCO)[1], has been difficult due to several challenges. They include fabrication challenges of creating highly transmissive interfaces and single nanometer separation lengths between the superconducting electrodes. The other is the lack of fundamental understanding of their transport properties. Therefore, resonances recently found in HTS/graphene junctions [2,3] needs to be studied in the S-Gr-S scheme to further understand the interactions due to proximity effects and confinement. Our recent study, discussed in Chapter-7, of transport in single BSCCO/Gr junctions showed the simultaneous occurrence of two scattering mechanisms, Klein tunneling (KT) and Andreev reflection (AR), leading to resonances[3]. Here, we examine the resonant scattering processes by joining two BSCCO/Gr junctions together to make BSCCO-Gr-BSCCO junctions.

We previously attributed the resonant scattering to a naturally formed p-doped barrier Gr' at the BSCCO/Gr boundary due to charge transfer from BSCCO. The Gr' region of finite length (d) provides two interfaces. The first interface with the bare graphene region (Gr) contributes to Klein-tunneling, supported by the reduced conductance in the p-n configuration by gating[4]. The second interface between the superconducting graphene region (Gr_Δ) and Gr' contributes to Andreev reflection and is evidenced by the suppression of resonances when the bias is above the induced superconducting gap in graphene by BSCCO. The two partially reflective interfaces result in a Fabry-Perot interference after two round-trips ($4 \times d$). By connecting two such BSCCO/Gr junctions to make a BSCCO-Gr-BSCCO junction, we link two hybrid scattering regions via a normal region of graphene.

8.1 Device details

Schematic representations of the device, a band diagram, and scanning electron micrographs of short and long devices are shown in Figure 34. The graphene regions $Gr_{\Delta 1}$ and $Gr_{\Delta 2}$ in Figure 34 (a) are under BSCCO and are superconducting from the proximity effect. Two p-doped regions of graphene Gr_1' and Gr_2' of length d_1 and d_2 are naturally formed at the boundary of each $BSCCO_{1,2}$/graphene junction by charge transfer are the resonant barriers. The $Gr_{\Delta 1} - Gr_1'$ and $Gr_{\Delta 2} - Gr_2'$ interfaces each contribute to AR. The $Gr_1' - Gr$ and $Gr_2' - Gr$ interfaces are responsible for KT. In this manner, the resonant scattering from AR and KT, previously reported in single BSCCO/Gr junctions, is recovered. Here, however, we modulate the length of the normal Gr region. A band diagram is shown in the bottom panel of Figure 34 (a) with a nodal gap in $Gr_{\Delta 1,2}$. Using the process detailed in Chapter-6.5, we fabricated several BSCCO-Gr-BSCCO devices of junction lengths (L) ranging from 20 nm to 3 μm, as shown in Figure 34 (b) and (c). Scanning electron microscopy (SEM) images were collected after transport measurements to measure the junction length.

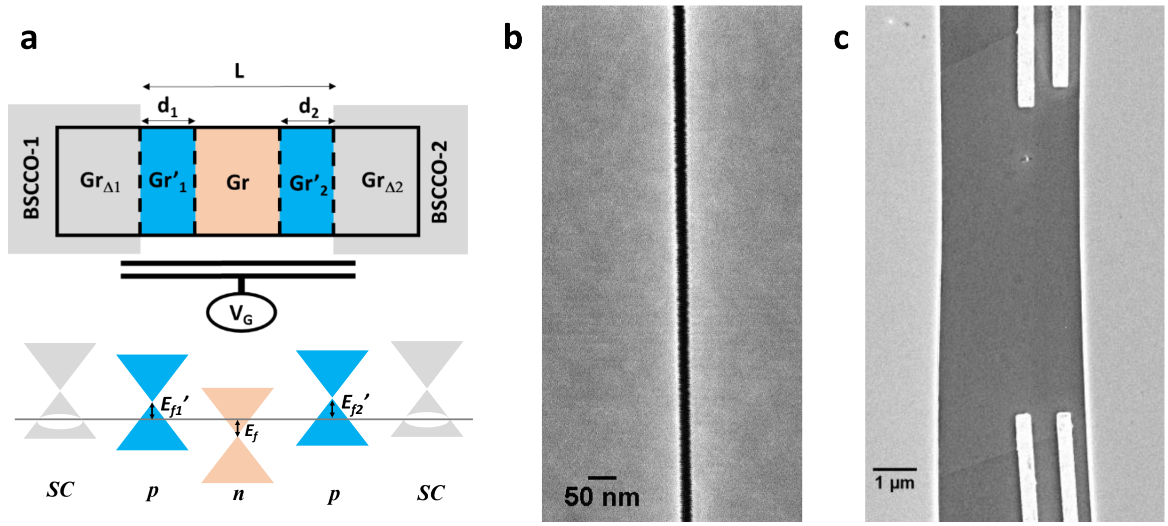

Figure 34. (a) Schematic of $BSCCO_1$-Gr-$BSCCO_2$ junction in the top panel and the corresponding band diagram in the bottom panel. $Gr_{\Delta 1,\Delta 2}$ (gray) are the regions of graphene with induced superconductivity and heavy hole-doping due to charge transfer. Similarly, the $Gr'_{1,2}$ regions are hole-doped barriers due to charge transfer and have a finite length $d_{1,2}$. SEM images of the shortest (Reg-1) and longest (Reg-3) $BSCCO_1$-Gr-$BSCCO_2$ junctions in (b) and (c) respectively.

8.2 Transport

We categorize the devices into three regimes according to the junction length. The first (Reg-1) below 100 nm, the second (Reg-2) between 100 nm to 1 μm, and third (Reg-3) for $L > 1$ μm. We measure the four-terminal conductance of all the $BSCCO_1$-Gr-$BSCCO_2$ junctions at 4.2 K as a function of gate voltage (V_g) in steps of 0.1 V. For comparison, portions of the normalized conductance from different length devices are offset and shown in Figure 35 (a). The shortest junction device from Reg-1 (L~21 nm), the top red curve, shows a clean oscillatory conductance with the largest period of 3.64 V. For devices in Reg-2, the middle blue curve (L~377 nm), the period is ~2 V. The bottom conductance curve in yellow for the long device from Reg-3 (L~3.04 μm) has a visibly reduced period of 1.5 V.

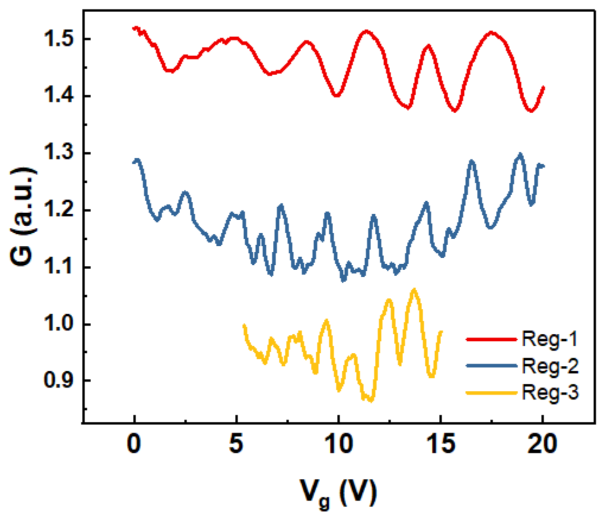

Figure 35. Representative normalized conductance of devices from different length regimes ($L = 21$ nm, 377 nm, and 3.043 μm measured at 4.2 K are offset and shown here for comparison.

The fast Fourier transform (FFT) of the conductance for different junctions is shown in Figure 36 (a), with the period (1/frequency) on the horizontal axis. We observe a reduction of the primary frequency from 3.65 V to ~1.5 V as the separation of the $BSCCO_1$-Gr-$BSCCO_2$ junction increases beyond 1 μm. The inverse scaling of the period with junction length is shown in Figure 36 (b).

Unlike the single junction case where studying the length dependence was limited, here by forming two junctions we are able vary the confining region Gr. The $\sim 1/L$ dependence seen in Figure 36 (b) (to be submitted for publication) is consistent with Fabry-Perot like resonance between two junctions. Therefore, with decreasing length, in addition to the resonances in the $Gr'_{1,2}$ regions, an additional resonance in the Gr region constraints to the overall resonance conditions. The resonance in the Gr region disappears eventually, resulting in the resonance condition shown in Figure 37 (b). In the long junction limit, the two junctions become decoupled, recovering the period of the single junction.

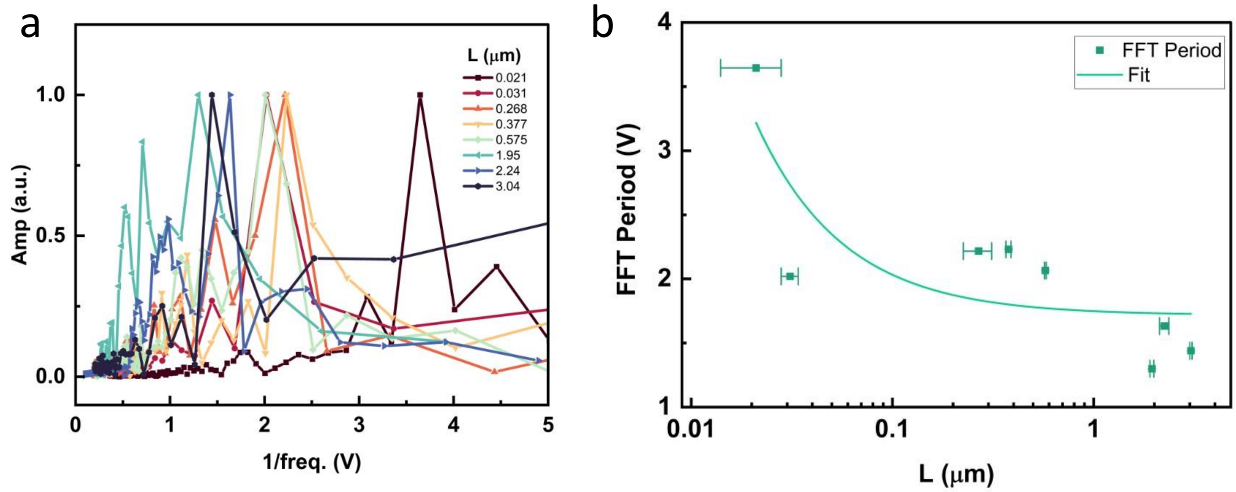

Figure 36. (a) The normalized FFT amplitude of the oscillatory junction conductance for different devices as function of the period. We see a decreasing shift in period going form Reg-1 to Reg-3. The primary period of the devices in Reg-3 tend to the average period of 1.5 V. (b) The period as a function of junction length shows the inverse scaling in period of resonances. Scatter points are primary period form FFT. The line is a fit curve according to the relationship in the main text.

We fit the primary FFT period as a function of length in Figure 36 (b) using the equation:

$$Period\ (V) = \frac{A}{L} + V_{sat}$$

The fitting constants are $A \approx 31$ mV μm) and $V_{sat} = 1.72$ V is the saturation period in the long $BSCCO_1$-Gr-$BSCCO_2$ junctions. V_{sat} is close to the average period of 1.7 V (Figure A5) found in the single BSCCO/Gr junctions. This indicates the resonant scattering due to KT and AR at the individual $BSCCO_{1,2}$/Gr junction approaches the single junction limit as the junction length between the two BSCCO increases above about 1 μm, i.e., devices in Reg-3. The sharp increase in the period below a critical length suggests a different resonance condition, as we explain below.

In $BSCCO_1$-Gr-$BSCCO_2$ junctions of Reg-1, when the Gr region of Figure 34 (a) tends to zero and $L \sim d_{1,2}$, we expect the entire graphene to be hole-doped. A schematic band diagram for the short junction is shown in Figure 37 (a). The *p-n* interface which is known to contribute to KT in single BSCCO/Gr and Reg-2 and Reg-3 junctions is absent in Reg-1 junctions. Therefore, carriers only undergo AR at each $BSCCO_{1,2}$/Gr junction and interfere in one round trip, as shown in the schematic Figure 37 (b).

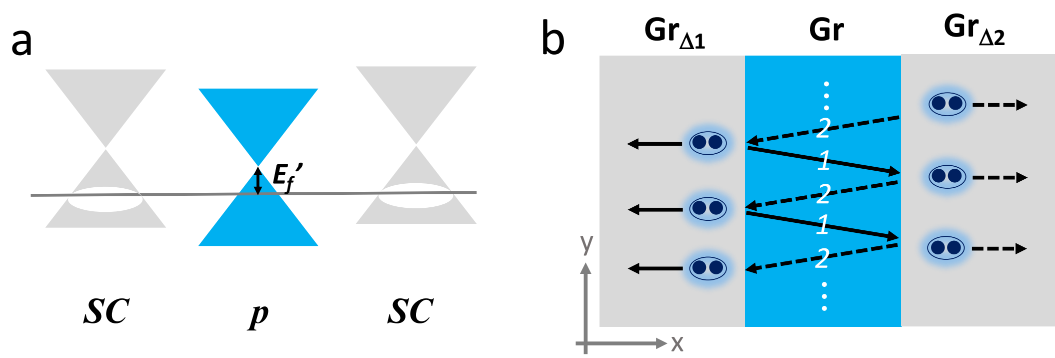

Figure 37. Carrier trajectories in the short junction limit leading to interference from multiple Andreev reflections. The electrons (solid) undergo AR at each Gr_{Δ} interface and convert to holes (dashed).

Again, the superconducting origin of these resonances is supported by the studies on excitation bias shown in Figure 38. The normalized amplitude of oscillations as a function of source-drain voltage (V_{ds}) for the shortest device from Reg-1 is shown in Figure 38 (a). We notice the oscillation amplitude drops by an order of magnitude when $V_{ds} > 30$ mV. In our previous work on single BSCCO/Gr junctions[3], we found the superconducting pseudo-gap induced in graphene is $\Delta_i \approx 15$ meV, consistent with other reports[5–7]. The presence of two superconducting leads in $BSCCO_1$-Gr-$BSCCO_2$ junctions requires twice the gap energy to suppress the superconducting transport, i.e., $2\Delta_i \approx 30$ meV, which is consistent with the observation in Figure 38 (a).

The differential conductance across $BSCCO_1$-Gr-$BSCCO_2$ on the same device is shown in Figure 38 (b), which was measured at different temperatures and shows the appearance of a gap-like feature below 28 K. Below 10 K, the gap is clearly visible when $V_{ds} \sim 30$ mV and is again consistent with the expected value of $2\Delta_i$. Specifically, $V_{ds} \geq 2\Delta_i/e$ required to diminish the oscillations in in Figure 38 (a) is consistent with the induced gap $\Delta_i \approx 15$ meV and confirms the superconducting origin and the role of AR in these resonances. The differential conductance of a long BSCCO-Gr-BSCCO ($L \sim 2.24$) μm junction is compared with a single BSCCO/Gr junction in Figure A4 of the Appendix.

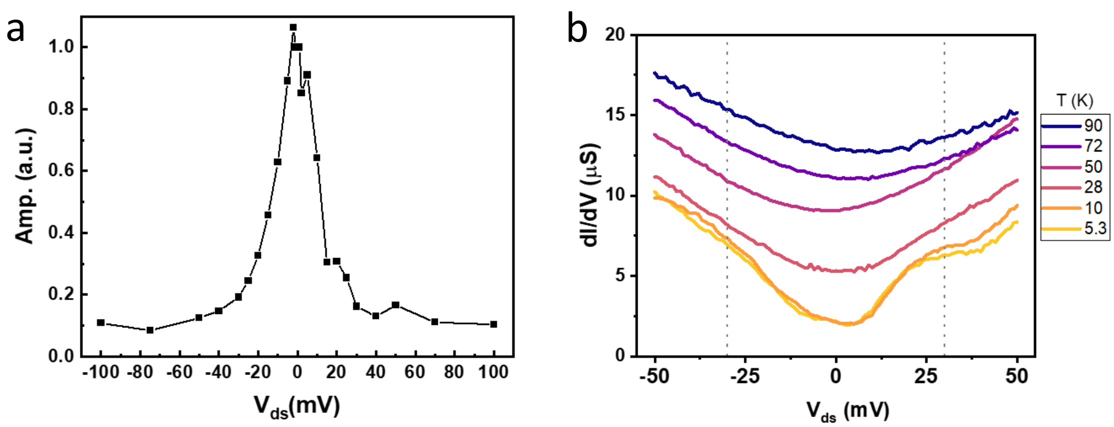

Figure 38. (a) The normalized amplitude of oscillations for the shortest device in Reg-1 at different DC bias while sweeping the gate voltage. The oscillation amplitude is diminished at twice the induced gap, $2\Delta_i \sim 30$ meV. (b) The differential conductance (dI/dV) of the S-Gr-S junction as a function of sweeping the DC bias. A sub-gap feature of $2\Delta_i \sim 30$ meV is also seen below 10 K.

8.3 Magnetic field data

Results on the gating studies of different BSCCO-Gr-BSCCO devices in a perpendicular magnetic field are shown in Figure 39 below. Figure 39 (a) and (b) correspond to devices in Reg-1 ($L = 21$ nm) and Reg-2 ($L = 377$ nm), respectively. The normalized conductance plots here show that the oscillatory conductance is largely unaffected at magnetic fields up to 2 T, unlike the results shown for the single junction devices and the double junction devices in the long junction limit (Figure 39 c). The weak magnetic field dependence is consistent the new resonance condition shown in Figure 37 (b) and consistent with the absence of p-n junctions whose conductance is dominated by the normal mode as discussed in Chapter-7.3.

For the long junction device from Reg-3 ($L = 1.95\ \mu$m), we show the junction resistance in a 3D colormap. Here, the oscillatory conductance at high gate voltage is preserved and the resistance near the Dirac point increases dramatically with magnetic field, recovering the behavior seen in the single junction. This further supports the decoupling of two BSCCO/Gr junctions in the long junction limit.

We estimate a shift of 1 Volt/Tesla for the resonances with magnetic field in Figure 39 due to an additional phase acquired by carriers, possibly for reasons similar to observations in bipolar graphene junctions[8,9] shown in Figure 5. Thus, the magnetic field data confirms the decoupling to the junction in the long device limit and a new resonance condition in the short junction limit.

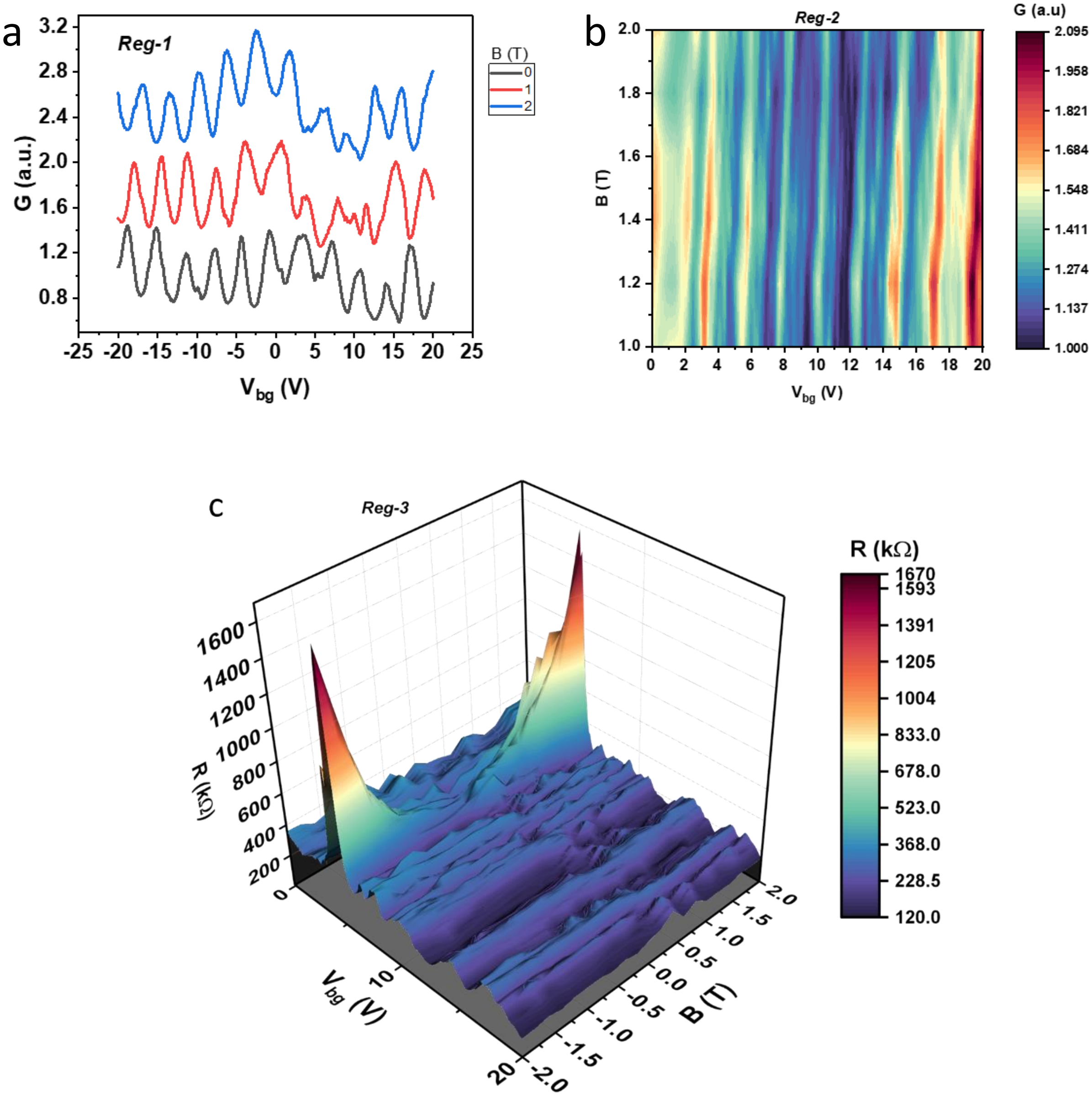

Figure 39. Transport in BSCCO-Gr-BSCCO devices in a perpendicular magnetic field. Normalized conductance for devices from Reg-1 (L=21 nm) and Reg-2 in (a) and (b) how resonances are robust with increasing magnetic field. (c) The resistance for a long BSCCO-Gr-BSCCO junction from Reg-3 increases at the Dirac point, however the resonances are unchanged at higher gate voltage.

8.4 Conclusion

We fabricated BSCCO-Gr-BSCCO junctions of different lengths and characterized the transport properties with gating. We found an inverse relationship between the resonance period and junction length. For the shortest junction, $L = 21$ nm, we observed the highest period of ~3.64 V. The period approaches 1.5 V in long junctions, $L > 1$ μm, this is close to the average period of 1.7 V observed in single BSCCO/Gr junctions. We confirm the contribution from Andreev reflection by observing an order of magnitude reduction in the oscillation amplitude as the applied bias approaches twice the induced superconducting gap, $2\Delta_i = 30$ meV, expected for a weak link between two superconductors. The differential conductance of the junction also supports this observation. The double junction data is consistent with Fabry-Perot resonances arising from the strength of the coupling between the two BSCCO/Gr junctions.

References

1. Perconte, D. *et al.* Long-Range Propagation and Interference of *d*-Wave Superconducting Pairs in Graphene. *Phys Rev Lett* **125**, 1–18 (2020).
2. Perconte, D. *et al.* Tunable Klein-like tunnelling of high-temperature superconducting pairs into graphene. *Nat Phys* **14**, 25–29 (2018).
3. Jois, S., Lado, J. L., Gu, G., Li., Q. & Lee, J. U. Andreev Reflection and Klein Tunneling in High-Temperature Superconductor/Graphene Junctions. *arXiv:2210.17503* (2022).
4. Stander, N., Huard, B. & Goldhaber-Gordon, D. Evidence for Klein tunneling in graphene *p-n* junctions. *Phys Rev Lett* **102**, 1–4 (2009).
5. Wu, Y. *et al.* The transport properties in graphene/single-unit-cell cuprates van der Waals heterostructure. *Supercond Sci Technol* **32**, (2019).
6. Zareapour, P. *et al.* Andreev reflection without Fermi surface alignment in high-T_c van der Waals heterostructures. *New J Phys* **19**, (2017).
7. Zareapour, P. *et al.* Proximity-induced high-temperature superconductivity in the topological insulators Bi_2Se_3 and Bi_2Te_3. *Nat Commun* **3**, (2012).
8. Shytov, A. V., Rudner, M. S. & Levitov, L. S. Klein Backscattering and Fabry-Pérot Interference in Graphene Heterojunctions. *Phys Rev Lett* **101**, 156804 (2008).
9. Young, A. F. & Kim, P. Quantum interference and Klein tunnelling in graphene heterojunctions. *Nat Phys* **5**, 222–226 (2009).

9. Conclusions and Outlook

In summary, we have shown that low-energy resonances dominate the transport properties of BSCCO/graphene junctions due to Andreev reflection and Klein tunneling occurring at two different interfaces of the *p*-doped Gr' region at the junction boundary. The resonances are observed in the asymmetric junction conductance between p^+-p and p-n configurations achieved by gating and supported by theory. The resonant condition occurs for every two round trips of carriers within the Gr' region. Phase coherent quasi-ballistic transport within the Gr' region supports the Fabry-Perot nature of the resonances. Our computed momentum-resolved spectral functions show the band structure of graphene with *d*-wave pairing and the sensitivity of the resonant modes gate bias, as also observed in the experiments. In BSCCO-Gr-BSCCO junctions, we observe an inverse scaling of resonance period with junction length.

Below are a few strategies for fabrication and characterization of heterostructures using BSCCO and graphene that can be pursued in the near future:

- Incorporating hexagonal boron nitride (h-BN) as a substrate or to encapsulate graphene has been shown to drastically improve the mean free path of carriers and reduce broadening in Fermi energy. Similarly, using h-BN as a substrate for the devices studied here can improve the properties near the Dirac point in transport measurements. Higher quality graphene can support quantum Hall states which can be studied in proximity to a graphene with nodal superconductivity from BSCCO.
- Strategies such as stacking at cryogenic temperatures can be explored to improve interface transparency of the BSCCO/graphene junction.

- Further understanding of the resonances may be gained by methods such as scanning tunneling spectroscopy (STS) to profile the density of states of the Gr' region at the BSCCO/graphene boundary. The bias spectroscopy of Gr' should reveal an oscillatory density of states that are sensitive to gating, as shown by our calculations of the spectral function.
- The contributions from specific orientations of the d-wave order parameter to transport in BSCCO/graphene junctions can also be explored in a systematic study. Exfoliated BSCCO flakes can have three or more crystallographic edges. These multi-faceted edges can be placed on graphene. Graphene can be shaped into strips of finite width, so the transport at the BSCCO/graphene junction is only into a single edge.
- The contributions from specular and retro Andreev reflection can be studied more closely in devices where the distance between the BSCCO/graphene boundary and the metal lead (L) is less than the length of the charge (d) transfer Gr' region, i.e., $L < d$. The Gr'-Gr interface, which is responsible for Klein tunneling, will not exist by doing so. This strategy could help to study only contributions from Andreev reflection in BSCCO/graphene junctions.
- Supercurrents in BSCCO-Gr-BSCCO junctions may be achievable by combining the cracking technique to achieve nanoscale separation between the superconducting contacts with annealing or cold stacking to improve the transparency of the BSCCO/graphene interfaces and using h-BN as the substrate.

Appendix

Basic Electrical Characterization

Once our devices are complete, they are immediately loaded into the Lakeshore CPX-VF probe station shown in Figure A (a). The triax connections to the probes and sample stage (for back-gate bias to the substrate) allow for low noise current and voltage measurement. The cross-section schematic of the cryostat in Figure A (b) shows the low-temperature limits of the different stages when cooled with liquid helium. Note that the probes are also cooled (15 K) via braided heat sinks to reduce large heat transfer to the sample upon contact. There is an indium foil to improve thermal contact between the samples and the stage. We mount multiple samples on the 2-inch diameter sample stage and ensure all probes reach all devices. Then the radiation shield is screwed on, the chamber lid is closed, and the cryostat is evacuated to 1×10^{-5} torr by dry pumps.

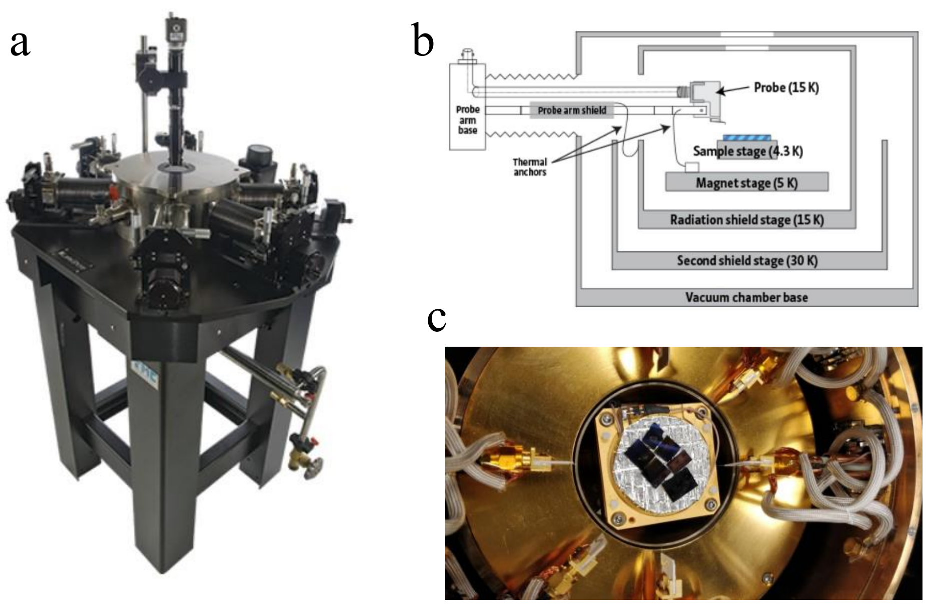

Figure A1. (a) Lakeshore CPX-VF probe station and (b) Cross-section schematic of the cryostat's internal stages, reproduced from the product manual. (c) Photograph of many samples on the stage.

We go through a series of important preliminary tests to check contact resistances, transition temperatures of BSCCO, and the junction resistance at temperatures from 300 to 77 K to help us find the devices that are fit for liquid helium measurements.

We carry out DC measurements using a Hewlett Packard 4156 B parameter analyzer. Its source-measure units (SMUs) can source and measure both current and voltage. The connections are triaxial from the SMUs to the probes, i.e., the guard is isolated from the signal but carries the same voltage as the signal to the probe arm. For AC measurements, we use SR-830 and SR-865 lock-in amplifiers from Stanford Research Systems. The AC excitation is sourced from SR-865. AC + DC measurements are possible by adding the two components using an SR-595 summing amplifier. The two-lug BNC outputs from the lock-in amplifiers (or the summing amplifier) are connected to the triax ports via a converter that floats the guard on the probes. The probe station is designed such that the exterior casing is at the same electrical ground (GND) as the triaxial probe connections. If the probe's guard is connected to GND, discharge events that occur in GND can be carried into the probe station and destroy devices. We are also diligent in calibrating the instruments. The AC and DC measurement instruments are synchronized with a temperature controller and a power supply for the superconducting magnet using GPIB connections. The different measurements are driven by LabView programs written by the candidate.

A.1 Transition Temperature

The resistance of BSCCO in all devices is measured by cooling from 90 K to 77 K (ramp rate of 1 K/min) either with DC or AC instruments. Figure A (a) below shows the DC resistance of BSCCO from a single device measured. We can see the transition from the normal state to superconductivity occurring at T_c~82 K which is simultaneously measured in both the four-terminal ($R_{4\text{-term}}$) and two-terminal ($R_{2\text{-term}}$) resistances. $R_{2\text{-term}}$ saturates to the contact resistance at T_c and then increases as temperature decreases. $R_{4\text{-term}}$ remains unchanged at 0 Ω below T_c. We prefer to keep the temperature sweep within 90 to 77 K because the probes tend to slide or lose contact over larger temperature set points. Measuring below 77 K using liquid N_2 is possible by pumping on the cryogen exhaust port, which cools the sample to ~65 K. The noise in the AC 4-terminal resistance versus temperature is better than the DC counterpart, which can be seen in Figure A (b) for BSCCO in different BSCCO-Gr devices on the same substrate. This difference can be attributed to the higher voltage resolution and phase-sensitive detection of the lock-in amplifiers. We generally observe T_c between 80-85 K in all devices.

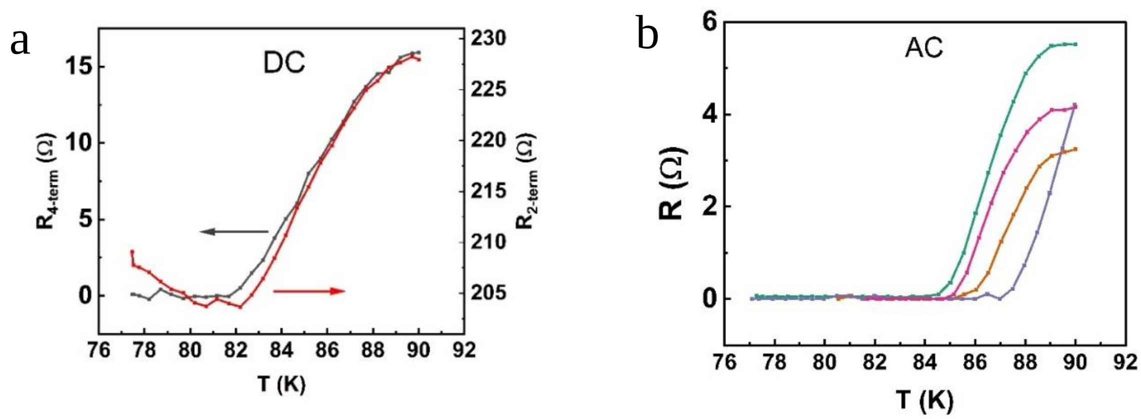

Figure A2. (a) DC 4-terminal (left vertical axis) and 2-terminal (right vertical axis) resistances of BSCCO in a single device as a function of temperature. (b) AC resistance as a function of temperature of BSCCO in four different devices on the same substrate.

We have noticed lower T_c when time consumed in device preparation is longer, likely due to the degradation mechanism discussed in Chapter-4. In the best-case scenario, we need 2-3 days to go from the exfoliation of BSCCO to the completion of BSCCO-Gr junction devices. When the devices are kept cold (<100 K) in the cryostat, we have not observed a significant change to the T_c even after two months.

A.2 Tunneling measurements of BSCCO

The tunneling conductance in metal-insulator-superconductor (NM-I-SC) junctions can tell us the size of the superconducting gap. The top few outer layers of BSCCO degrade to an insulating state over time by the loss of oxygen. Ohmic contacts are made by etching away these layers to contact the pristine bulk as described earlier in Chapter-6. We created tunnel contacts to BSCCO by preserving the sacrificial insulating layers and using our standard e-beam lithography process described in Chapter-6 for metal deposition and lift-off. The resistance of tunnel contacts ranges from 10-20 MΩ, which is five orders of magnitude higher than the ohmic contacts.

An AC+DC bias was applied on a tunnel contact (yellow) and the other ohmic contact (red) was connected to the current input of the lock-in amplifier which filters the DC component of the current to the chassis ground. A simplified circuit is depicted in Figure A3 (a) and an optical image of the device (T_C~80 K) is shown in Figure A3 (b). Panels (c and d) in Figure A3 are the differential conductance (dI/dV) measurements in which we verified the superconducting pseudo-gap of BSCCO to be $\Delta_0 \approx 40$ meV, comparable with previous results. In addition, we see conductance oscillations occurring in intervals of Δ_{BSCCO} in both positive and negative excitation bias.

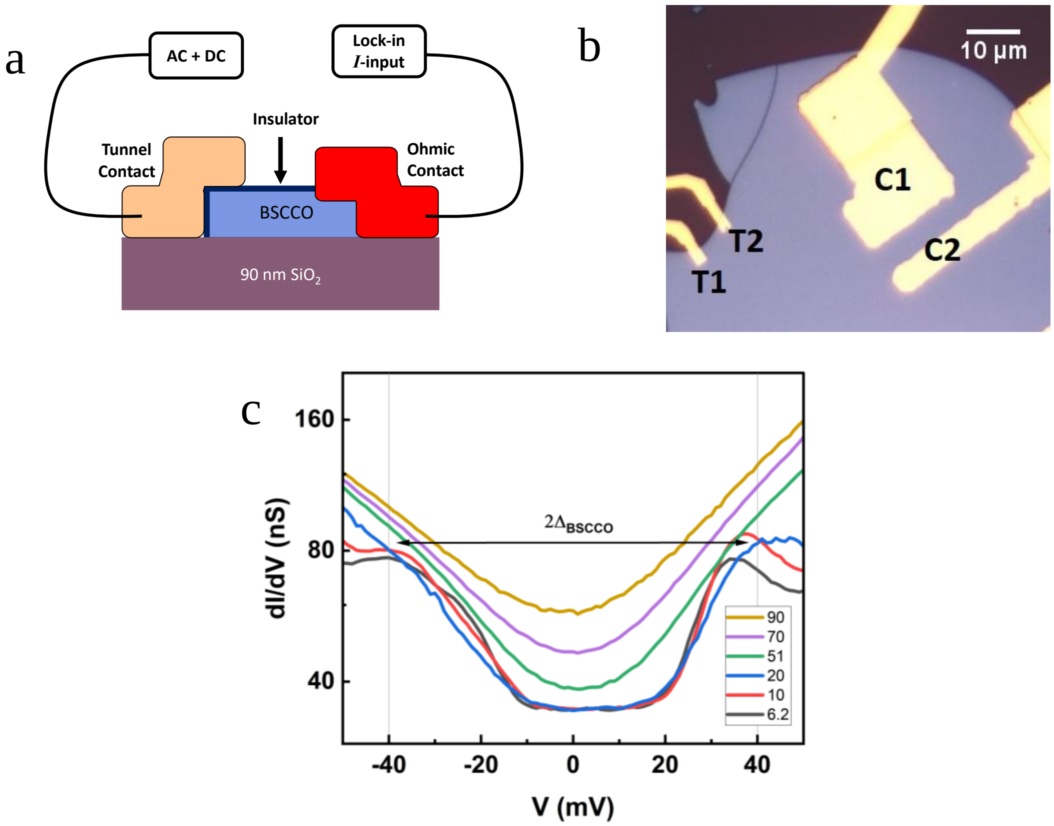

Figure A3. (a) Schematic cross section of a BSCCO device for the tunneling experiment using AC+DC measurement. (b) Optical image of the device with tunnel contacts labelled T1 and T2 and ohmic contacts labelled C1 and C2. Data in (c) shows the size of the superconducting gap of BSCCO evolve with temperature.

A.3 Differential Conductance Between S/Gr vs S-Gr-S

The normalized differential conductance (dI/dV) for the single S/Gr junction and a long S-Gr-S ("S" is short for BSCCO) are shown in Figure A4 below for comparison. From the differential resistance of the S/Gr junction, device B shown earlier in Figure 30, we inferred the induced pseudogap in graphene is $\Delta_i \approx 15$ meV. This feature appears softer in the dI/dV for the same S/Gr device (black) shown here in Figure A4. The dI/dV for a short S-Gr-S from Reg-1 ($L\sim 21$ nm) was shown previously in Figure 38 (b), where $2\Delta_i \sim 30$ meV was inferred. Similarly, we see a pseudogap feature at $V_{ds}\sim 30$ mV in Figure A4 for a long S-Gr-S junction from Reg-3 ($L = 2.24$ μm). As explained previously, an S-Gr-S junction will require a bias $eV > 2\Delta_i$ for transport to be dominated by single particles outside the gap energy. Additionally, in both the dI/dV below we can see a second sharper feature around 40-50 mV that corresponds to Δ_{BSCCO}.

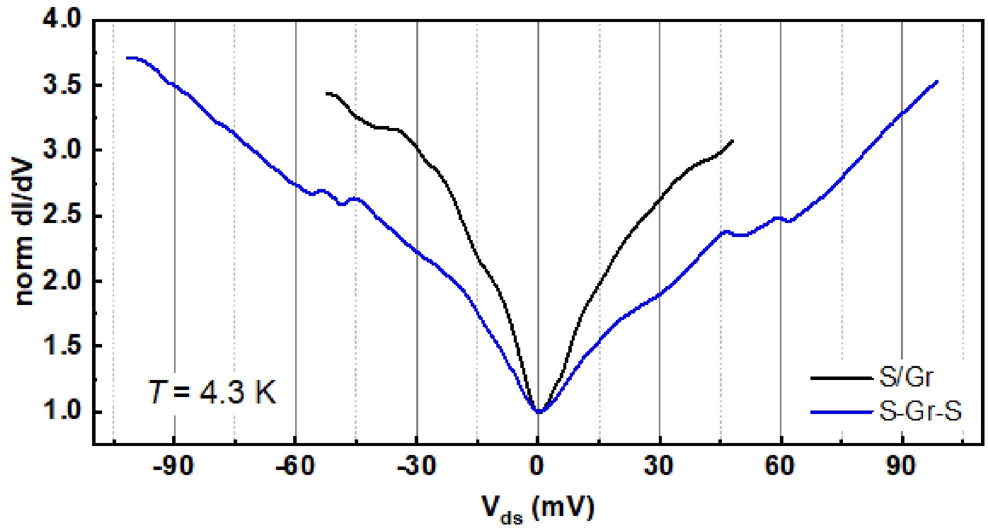

Figure A4. Normalized dI/dV for S/Gr (black) compared with S-Gr-S (blue) at liquid helium temperature. Both spectra suggest the induced gap in graphene is $\Delta_i \sim 15$ meV and also show the gap edge features at expected energies for Δ_{BSCCO}.

A.4 Period in Voltage for all BSCCO/Gr devices

The mean and standard deviation of oscillation period in gate voltage observed in each of the single BSCCO/Gr junctions A-E from Table **1** is shown below in Figure A5. The average period across these devices is 1.7 V, indicated by the blue line.

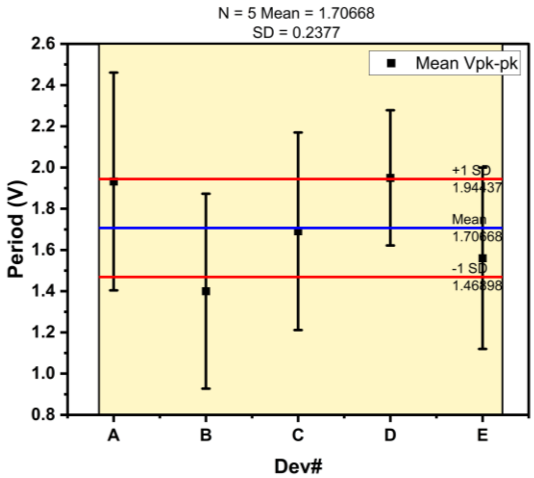

Figure A5. Average period of resonances in gate voltage for the different BSCCO/Gr devices. The mean period across them is ~1.7 V. The standard deviation (SD) is ~0.24 V.